TIME INTEGRATED DETECTION AND APPLICATIONS OF FEMTOSECOND LASER PULSES SCATTERED BY SMALL PARTICLES

Vom Fachbereich Maschinenbau
an der Technischen Universität Darmstadt
zur
Erlangung des Grades eines Doktor-Ingenieurs (Dr.-Ing.)
genehmigte

D i s s e r t a t i o n

vorgelegt von

Dipl.-Phys. Saša Bakić

aus Darmstadt

Berichterstatter:	Prof. Dr.-Ing. C. Tropea
1. Mitberichterstatter:	Prof. Dr.-Ing. N. Damaschke
2. Mitberichterstatter:	Prof. Dr. rer. nat. W. Elsäßer
Tag der Einreichung:	30.06.2009
Tag der mündlichen Prüfung:	04.09.2009

Darmstadt 2010
D17

Abstract

In this thesis the time integrated detection of scattered femtosecond laser pulses, and illumination from a continuous wave semiconductor laser source with optical feedback and adaptable coherence length, is investigated for small particles. In this context the scattering function for small particles is numerically advanced. The angular distribution of local maxima of the scattering function is presented for small particles under ultrashort pulse illumination. The position of local maxima relating to scattering angle, particle size and refractive index is calculated with Fourier-Lorenz-Mie theory. Moreover, an estimate of the sensitivity of the scattering function to non-sphericity is presented, utilizing general Lorenz-Mie theory. For ultrashort pulse illumination the maxima of the supernumerary bows of the primary rainbow, which hold information on particle size and refractive index, are freed from disturbing interferences with reflection order and higher refractive order contributions. The presented results indicate the feasibility of precise in-situ measurements with Rainbow refractometry for highly spherical small particles with compact and cost-efficient sources of illumination and quantify the pulse duration or coherence length for the desired lower size range, which is essential information for future experimental studies. Moreover, a substantial reduction of morphology dependent resonances for microscopic water droplets is successfully demonstrated. For the first time, an electrodynamic Paul trap with novel geometry is applied to successfully observe the scattering of femtosecond laser pulses on small water droplets not only during a short period of milliseconds as in a droplet stream, but also over the temporal evolution of an evaporating droplet. Beyond Rainbow refractometry, the acquired results indicate the feasibility of new measurement techniques and the significant enhancement of existing methods. Under the aspect of the separation of scattering orders, interferometric particle imaging (IPI) is enhanceable by fitting the coherence length to the angle of detection. Illumination of small particles with femtosecond laser pulses is shown to facilitate direct size measurement from focused images of a thin spray by measurement of the intensity ratio of specific glare points on individual particles. Moreover, the smoothing of the diameter-intensity function for small particles allows for more precise determination of the Sauter mean diameter in the named size range. Due to the introduction of coherence length as a variable parameter for small particle charac-

terization, the advantages of time integrated detection of femtosecond laser pulses scattered by small particles are underscored by the outlook of utilizing spatially compact and cost-efficient semiconductor laser devices with the important benefit of adjustable coherence length.

Kurzzusammenfassung

In dieser Doktorarbeit wird die Zeitintegrierte Detektion von gestreuten Femtosekunden-Laserpulsen an kleinen Partikeln untersucht. Als alternative Beleuchtungsquelle dient die Emission einer Halbleiter-Laserquelle im Dauerstrichbetrieb mit optischer Rückkopplung und anpassbarer Kohärenzlänge. In diesem Zusammenhang konnte die Streufunktion für kleine Partikel numerisch erweitert und die angulare Verteilung der lokalen Maxima der Streufunktion für Beleuchtung durch fs-Laserpulse dargestellt werden. Dabei wird die Position dieser lokalen Maxima in Abhängigkeit von Streuwinkel, Partikeldurchmesser und Brechungsindex durch die Fourier-Lorenz-Mie Theorie ermittelt. Darüber hinaus wird die General-Lorenz-Mie Theorie genutzt um eine Abschätzung der Empfindlichkeit der Streufunktion für Nicht-Sphärizität von Partikeln vorzustellen. Bei Beleuchtung durch fs-Laserpulse werden die Maxima der Streulichtkeulen des primären Regenbogens, die Informationen über Partikelgröße und Brechungsindex enthalten, von störenden Interferenzen befreit, die durch die Überlappung der Reflexion an der Oberfläche des Teilchens und höheren Streuordnungen entstehen. Die vorgestellten Ergebnisse weisen auf die Machbarkeit von präzisen in-situ Messungen mit der Regenbogenmesstechnik mit kompakten und kosteneffizienten Beleuchtungsquellen hin, und quantifizieren die Pulslänge bzw. Kohärenzlänge für die Untersuchung kleiner Partikel. Diese Ergebnisse sind essenziell für zukünftige experimentelle Studien. Ferner wird eine beträchtliche Reduzierung von Strukturresonanzen für mikroskopische Wassertropfen erreicht. Zum ersten Mal wird eine elektrodynamische Paulfalle (mit neuentwickeltem optischen Zugang) genutzt, um das Streulicht von fs-Laserpulsen während des Verlaufes der Verdunstung eines kleinen Wassertropfens zu messen. Jenseits der Regenbogenmesstechnik weisen die erzielten Ergebnisse auf die Realisierbarkeit neuer, und die Weiterentwicklung bestehender Partikelmesstechniken hin. Unter dem Aspekt der Separierung der Streuordnungen kann Interferometric Particle Imaging (IPI) durch Anpassung der Kohärenzlänge an den Detektionswinkel erweitert werden. Die Beleuchtung kleiner Partikel durch fs-Laserpulse ermöglicht deren direkte Größenmessung durch Auswertung fokussierter Abbildungen eines dünnen Sprays und der Verhältnisbildung der Intensitäten bestimmter Glanzpunkte auf einzelnen Partikeln. Außerdem führt die Reduzierung von störenden Interferenzerscheinungen in der Darstel-

lung der Beziehung von Durchmesser und Streuintensität zu der Möglichkeit einer präziseren Messung des Sauterdurchmessers kleiner Partikel. Die Kohärenzlänge wird also als zusätzlicher Freiheitsgrad in der Partikelmesstechnik eingeführt. Der Nutzen der Zeitintegrierten Detektion von gestreuten fs-Laserpulsen wird demnach durch den Einsatz einer kompakten und kosteneffizienten Halbleiter-Laserquelle mit dem Vorteil der Einstellbarkeit der Kohärenzlänge erweitert.

Acknowledgments

The research work at hand has been carried out at the Chair of Fluid Mechanics and Aerodynamics, Technische Universität Darmstadt between March 2005 and June 2009.

I am deeply grateful and would like to thank my advisor Prof. Dr.-Ing. C. Tropea very much for the opportunity to learn the skills needed for conducting successful research and for patiently advising, guiding and encouraging me during the course of this work. Prof. Dr. rer. nat. W. Elsäßer as well has been extremely kind, patient and generous by providing unlimited personal and most crucial technical support. Prof. Dr.-Ing. Damaschke has been a constant, profoundly helpful and patient role model who gave me the confidence and taught me the endurance to successfully complete the work at hand.

Of course this work could not have been achieved without the substantial financial support of the Deutsche Forschungsgemeinschaft (DFG) advancing the project through grant DA 600/2 and also the financial and scientific support by the Graduiertenkolleg "Optische Messtechniken für die Charakterisierung von Transportprozessen an Grenzflächen" (GRK1114).

By name I would like to mention and thank very much Dr. Heinrich Bech, Dr. Tobias Michel, Dr. Michael Peil, Dr. Guillaume Castanet, Dr. Christian Heinisch, Dr. Feng Xu, Dr. Joachim Kaiser, Dipl.-Ing. Stefan Bareiss, Dipl.-Phys. Robert Irsig, Dipl.-Ing. Hagen Koroll and last but not least Mr. Tarek Anous for the successful and inspiring professional cooperation. The indefinitely cordial professional and personal support by many more colleagues and friends will be pleasantly remembered and missed in the years to come.

Contents

Chapter 1

Introduction

Over the course of the last years new applications and measurement techniques have been established in a variety of fields in consequence of the development and commercialization of femtosecond pulse lasers. This is due to three extraordinary characteristics of ultrashort laser pulses:

The extremely short pulse duration allows for an according time resolution of physical processes. Therefore pulses with this property can be applied, e.g., in ultrafast spectroscopy for real-time observation of molecular vibrations (Baumert et al. 1991). Moreover, femtosecond pulses stand out due to their comparatively broad spectral width. As a chain of pulses is generated, the temporal width of individual pulses reflects the spectral width of the gain medium. The pulse repetition rate is given by the length of the laser resonator. Linked to the broad spectrum is a narrow effective coherence length, which corresponds to the pulse length. According to the speed of light ($c = 299792458$ m/s) the spatial pulse length is $x = 0.3$ μm per fs, defining the spatial resolution. Additionally, femtosecond laser pulses can reach very high energy densities, establishing new approaches for ablation of substances or tissue in material science and medicine (Laser Technik Journal 4/2005). This third characteristic of high pulse energies also permits the study of nonlinear optical effects (Oberlé et al. 1995). Therefore femtosecond laser pulses are nowadays an integral part of medicine, chemistry and physics.

However, applications in engineering, except in material processing (Zoubir et al. 2003), are rare. This study aims to establish femtosecond laser pulses in the field of optical measurement techniques, more precisely in the domain of single particle characterization. In this context, particles are optical inhomogeneities in the size range of a few millimeters down to less then a micrometer. The necessity for particle characterization becomes obvious with the applications involved:

Characterization of sprays e.g. is a well investigated field of application (Nasr et

al. 2002). As outlined in Frohn and Roth (2000), for internal combustion engines the particle size is important, because the fuel is supplied to the combustion chamber as liquid droplets (Kowalewicz 1984). For building small and efficient cooling systems, the evaporation of liquid droplets is a crucial field of study (Tinker et al. 1995). Pharmaceuticals can be delivered as an aerosol to a patient through the respiratory system. The droplet size determines which area of application is reached by the particles (Nikander 1997).

While droplets and bubbles have an even surface and are therefore numerically manageable, non-spherical and highly irregular particles are more difficult to approach. In the later case, inversion strategies exist only for certain types of particles (Xu et al. 2007). Hence, most naturally occurring particles are described by statistical quantities like average concentration or surface roughness. The focus of the study at hand are measuring methods for the characterization of individual, spherical particles within a process relevant ensemble of particles, based on the scattering of femtosecond laser pulses. These are so-called counting methods which assign in-situ properties to every single detected particle within an ensemble, e.g. velocity, size, temperature or form and structure. Counting methods differ from statistical methods (LIDAR, e.g. Gillespie et al. 2002, diffraction measurement, e.g. Malvern Instruments GmbH, global Rainbow thermometry, van Beeck et al. 1999, planar droplet sizing, Domann and Hardalupas 2001). Counting methods have the advantage of allowing for concentration and flux density measurement, e.g. number-, volume-, mass-concentration or concentration of momentum of a particle ensemble. However, the requirements compared to statistical methods are thereby significantly higher. Counting methods are used predominantly for development and research in non-contact, quantitative determination of particle parameters, while statistical methods for particle characterization, due to their simple implementation, are commonly employed for monitoring purposes and process quality control. Due to the difficulties of numerical inversion of light scattering for single particles larger then the wavelength of light, and because the optical access to a particle within the geometry of the experimental setup is nontrivial, only few counting methods for single particle characterization are available commercially (phase Doppler, imaging techniques, shadow Doppler, interferometric particle sizer). Further methods, as well as the already available techniques, are subject to research and development: Laser induced fluorescence (Lavieille et al. 2004), time-shift technique (Damaschke et al. 2002a), phase Doppler (Schelinsky 2002, Damaschke 2003), global phase Doppler (Damaschke et al. 2005), interferometric particle imaging (Maeda et al. 2002), Rainbow measurement technique (van Beeck 1997, Wilms 2005), imaging techniques (e.g. Nishino et al. 2000), digital holography (Palero et al. 2005, Raupach et al. 2006) and shadow Doppler (Jones et al. 2002). The most commonly used and commercially available counting

method for particle size characterization is the phase Doppler technique (Albrecht et al. 2003). The phase Doppler technique assumes homogeneous and spherical particles. This is true for droplets and bubbles which are not characterized directly after being generated.

A series of inversion strategies have been proposed to determine the refractive index of particles (Card and Jones 1991, Onofri et al. 1996, van Beeck 1997, Onofri 1999, Schaller 2000, Vetrano et al. 2004). Measuring the refractive index of particles is of importance because of the connection to particle temperature and the identification of the components in two-phase particles. The determination of temperature of small particles ($d_p < 30$ μm), and the identification of substance by refractive index measurement, is fundamental to many processes of optimization, but also in combustion problems. The determination of temperature of droplets with the rainbow measurement technique has been investigated by a number of study groups (van Beeck 1997, Roth 1998, Damaschke 2003, Wilms 2005). Especially the study group around Gouesbet and Gréhan has contributed not only to inversion strategies and temperature measurement, but also to the understanding of refractive index gradients in droplets (Saengkaew et al. 2007).

In principle, two inversion strategies have to be distinguished. First, the angular position of the supernumerary bows of the rainbow given by Airy theory are a direct measure for the refractive index of a homogeneous, spherical particle. This technique was investigated by van Beeck (1997). However, this works only under strict laboratory conditions due to the requirements of sphericity, especially for larger droplets. Beyond that, the technique is inaccurate for small particles, due to interference of higher scattering orders with the supernumerary bows (Damaschke et al. 1998). The company TSI Inc. put this technique to use in 1993 by implementing a rainbow refractometer (Sankar et al. 1993), but its preformance was limited by the above mentioned problems (Heukelbach et al. 1998, Hom 2000). In van Beeck et al. (1999) the global Rainbow thermometry was presented as a statistical measurement technique for an ensemble of particles. With this method uncertainty for single particles is reduced by averaging across the ensemble. The average angular position of the rainbow is a measure for the average particle diameter. However, in doing so, data for single particles is not available anymore.

The second inversion strategy utilizes, instead of the Airy-approximation, the exact angular intensity distribution of a single particle. This distribution includes the ripple structure resulting from interference with higher scattering orders in the rainbow region and morphology dependent resonances (MDR)(Roll 1999). It can be used to precisely determine the particle diameter, diameter change in time and refractive index. Mostly the measured intensity distribution is compared with numerical results for various diameters and refractive indices. In particular, by detec-

tion of MDR´s, the diameter alteration rate can be determined (Wilms 2005). This method gives precise results, however it requires an excellent signal-to-noise ratio and very stable experimental conditions only obtainable with levitated droplets or monodisperse droplet chains. This method is excellent for characterization of single, non-moving droplets, e.g. for validating evaporation models, but fails due to low SNR´s for moving particles within in-situ applications.

Currently the temperature, not refractive index, determination by spectral analysis of fluorescent dyes within a particle is being commercialized (e.g. Lavieille et al. 2004). The method determines temperature change accurately to 1 K, but demands dye placement inside the particle. Other methods have been proposed for refractive index determination, using geometrical optics. Schaller et al. (1994) studied the intensity ratio of two glare points, e.g. caused by the scattering orders of reflexion and first-order refraction, depending on refractive index and particle size. In this example geometrical optics predict a monotonous intensity ratio between the glare points. However, the monotonous relation is disrupted due to interference between the involved electromagnetic waves. Various scattering orders interfere in the far field and angular intensity maximas are generated. With changing particle size or refractive index the intensity maximas migrate over the detector surface and modulate the received intensity. For this reason, especially for small, simple and therefore preferable apertures without lenses, particle sizing becomes unfeasible. Additionally, the scattering cross section of particles swells dramatically for certain diameters in spacings of a few 100nm due to MDR´s. MDR´s modulate the intensity of every single scattering order and completely disrupt the monotonous relationship between scattered intensity and particle size, and refractive index respectively. In principle, MDRs can be eliminated by using a spectrally broad source, e.g. a light bulb. A white light source though is hard to focus, or rather not easy to couple into a fiber, and the intensity (photon flux per solid angle) is far less in magnitude compared to a laser source. For this reason, e.g. for particle image velocimetry (PIV), laser light is almost solely used for measurements. Accordingly this study examines the potential of laser sources with a broader spectral gain, and therefore shorter coherence length, for in-situ particle characterization. Moreover, currently proposed, common counting methods for particle parameter determination, except Damaschke et al. (2002a), depend on two or more optical access points for detection. This increases the complexity of adjustment of the mechanical and optical setup. In summary, especially the phase Doppler technique is a reliable optical counting method, which determines particle size. Currently no in-situ optical counting method measures refractive index and particle volume dependably enough for deployment in industrial processes.

The idea of using femtosecond laser pulses for single particle characterization has been initiated through detailed simulation of femtosecond pulse scattering by

Gouesbet and Gréhan (2000a,b). However, the computation of short pulse scattering was feasible before (Shifrin and Zolotov 1994, 1995) and has been applied otherwise (Sbanski et al. 2000). The statistical, time resolved description of multiple particle scattering by Monte-Carlo simulation of femtosecond laser pulses, which have a pulse length comparable to the diameter of utilized particles, has been investigated by Roze et al. (2003) and Berrocal et al. (2005). Experimentally, Linne et al. (2005) implemented a time-gated ballistic imaging instrument which utilizes femtosecond laser pulses to provide single-shot images with high spatial resolution of the liquid core in e.g. a water spray.

To investigate the potential for in-situ counting methods with femtosecond laser pulses, in the study at hand numerical computations and experimental verifications have been carried out to quantify the measurement methods, by means of acoustic and electrodynamic levitation of single particles, monodisperse droplet chains and thin sprays of small particles, e.g. Bakic et al. (2008, 2009). Suggestions for the use of femtosecond laser pulses for single particle characterization have been proposed by Mees et al. (2001a,b,c and 2002), Damaschke et al. (2002), Bech and Leder (2004, 2006) and Roze et al. (2003). Due to the temporal and spatial shortness of a femtosecond laser pulse the scattering orders, e.g. first, second, third refractive order, leave the particle temporally displaced. Therefore work on ultrashort pulse scattering so far focuses on the time delay between scattering orders. However, due to the extremely high experimental demand for time resolved detection this study favors the approach of time integrated detection. The applicability of properties of femtosecond laser pulses, such as the broad spectral range, are investigated in this context and the coherence length is introduced as a novel degree of freedom for small particle characterization. Comparable studies on utilization of femtosecond pulses and corresponding short coherence length in combination with time integrated detection are currently not available in literature.

Following this introduction, chapter 2 introduces the properties of femtosecond laser pulses by exemplarily deconstructing the process of generating them with a Ti:Sapphire laser to concepts like coherence, mode-locking and dispersion. While a Ti:Sa laser is a powerful tool with high output intensity facilitating experimental verification, less spacious and more cost-efficient sources of short coherence length are discussed. Chapter 3 focuses on the intensity distribution for various angles and diameters emitted by a particle illuminated with a laser beam under the restrictions of Mie-scattering. After a discussion of the physically more conceivable Airy-theory rigorous Fourier-Lorenz-Mie theory (FLMT) and general-Lorenz-Mie theory (GLMT) are utilized to compare and predict effects for coherent and pulsed illumination (Bakic et al. 2009). Because the numerical results consider spherical, homogeneous particles, and because of many industrial applications, it is favorable

for experimental verification to create and position small liquid droplets. Chapter 4 therefore introduces various methods and devices to meet this requirement. A Paul trap with novel geometry of optical access crucial to this work is presented (Heinisch 2006, Bakic et al. 2008). To experimentally verify numerical characteristics of the scattering function chapter 5 focuses on the implementation of various combinations considering the properties of the detection device, the type of laser source, and the generation and preparation of droplets. The angular intensity distribution and the diameter-intensity relationship of small droplets under short coherence length illumination are detected (Bakic et al. 2008). In addition to this experimental verification chapter 6 discusses the prospect of enhancing several existing particle characterization techniques like Rainbow refractometry and is followed by a conclusion in chapter 7.

Chapter 2

Properties of Laser Pulses and Short Coherence Length

In this section the properties of femtosecond laser pulses and possible alternatives for small particle characterization are discussed as outlined by Hirlimann in Rullière (2005). This is achieved by assembling the process of generating ultrashort pulses with a Ti:Sapphire laser successively from the concepts of coherence, optical resonators, nonlinear optics, Kerr-effect, mode-locking and despersion. While a Ti:Sa laser with its high output intensity facilitates experimental verification, less spacious and more cost-efficient sources of short coherence length are introduced as an alternative way of generating laser illumination with appropriately short coherence length.

2.1 Coherence

Coherence and therefore interference are essential for the process of constructing ultrashort laser pulses from an optical resonator. Also, for particle characterization with femtosecond laser pulses the detected intensity distribution is a result of various scattered fragments of pulses overlapping or shifted to each other in time and space. To clarify this interactions and the importance of ultrashort laser pulse illumination in comparison to pulse lengths exceeding the diameter of a particle, it is necessary to introduce the concepts of spatial and temporal coherence.

Coherence and incoherence are two extreme cases describing the phase relationship of two light waves (e.g. Born and Wolf 1999, Demtröder 2003). A degree of coherence in between becomes noticeable by lower contrast in interference experiments. Instead of the expressions partial coherence and full coherence, one also speaks equally of coherence and full coherence. Mutual coherence characterizes the case of two independent light sources, whose emitted light waves overlap at an accord-

ing point in space. However, in interference experiments interfering light waves normally originate from a single source and are divided by beam splitters. Mutual coherence can be analytically described by a function of cross-correlation. Π provides the extent of similarity between two amplitudes integrated in a wavefield at positions $\vec{r}_{1,2}$:

$$\Pi_{1,2}(\overline{t}) = \lim_{T\to\infty} \frac{1}{T} \int_{-T/2}^{T/2} E(\vec{r}_1, t) E^*(\vec{r}_2, t + \overline{t}) \tag{2.1}$$

the function of contrast is therefore:

$$C_{1,2}(\overline{t}) = \left| \frac{2\Pi_{1,2}(\overline{t})}{\Pi_{1,1}(0) + \Pi_{2,2}(0)} \right| \tag{2.2}$$

For no coherence to partial to full coherence, the function ranges over $0 \leq C_{1,2}(\overline{t}) \leq 1$. From the spatially extended wave field of a source two partial waves can be derived from two different points within the wave field. Interference between those partial waves occurs if they are coherent. In terms of the function C, due to t = 0, this can be expressed as:

$$C_{1,2}(0) = \left| \frac{2\Pi_{1,2}}{\Pi_{1,1} + \Pi_{2,2}} \right| \tag{2.3}$$

The entire wave field is called spatially coherent, if oscillations of the electric field have a constant phase relationship between arbitrary points in space. Accordingly, a wave field of a light source is called temporally coherent, if two arbitrary oscillations of the electric field have a constant phase relationship at a single point in space for different times. Moreover, light waves from an identical emission center are not necessarily coherent. This is due to a statistically distributed phase to each other of successively emitted photons from such an emission center. Only photons originating from a single act of emission are coherent to each other. The spatial difference between them must not be larger than the length of one wave train. This

highest acceptable distance is called coherence length. The time a light ray needs to pass this distance is called coherence time. A temporally stable interference structure can only be observed if the phase difference between the partial waves in a specific point in space changes less then $\nu = 2\pi$ during observation time. The partial waves are then called temporally coherent. With the positions 1 = 2 and two separate fields $E_{1,2}$ in equation (2.1) the function of contrast is then:

$$C_{1,2}(\overline{t}) = \left| \frac{\Pi(\overline{t})}{\Pi(0)} \right| \tag{2.4}$$

The concept of coherence length can also be clarified as follows: Every natural source of light, as well as a laser, emits light with a central frequency ν_0 and a spectral width $\Delta\nu$. This emission can be seen as a superposition of many monochromatic waves with frequencies within the interval $\nu_0 \pm \Delta\nu/2$. The phase difference δ between such partial waves with the frequencies $\nu_1 = \nu_0$ - $\Delta\nu/2$ and $\nu_2 = \nu_0 + \Delta\nu/2$ is for $\delta(\mathrm{t}_0) = 0$:

$$\Delta(t) = 2\pi * (\nu_2 - \nu_1) * (t - t_0) \tag{2.5}$$

The phase difference accumulates linearly with time t. After the coherence time $\Delta\mathrm{t}_c = \Delta\nu^{-1}$ has passed, the phase difference is $\delta(\Delta\mathrm{t}_c) = 2\pi$. The coherence length of a light wave is therefore the reciprocal of the spectral width $\Delta\nu$:

$$\Delta t_c = \frac{1}{\Delta\nu} \tag{2.6}$$

A monochromatic wave has an infinite coherence time according to the relation above. Conversely, a wave whose phase drifts quickly will have a short coherence time. Similarly, pulses (wave packets), which naturally have a broad range of frequencies, also have a short coherence time since the amplitude of the wave changes quickly. The most monochromatic sources are usually lasers (so-called continuous wave illumination). Such high monochromaticity implies long coherence lengths (up to hundreds of meters). For example, a common stabilized helium-neon laser

can produce light with coherence lengths in excess of $x = 5$ m. Not all lasers are monochromatic, however (e.g. a Ti:Sa laser). For a white-light source such as a light-bulb, t_c is also small, it is considered a spatially incoherent source. In contrast, a radio antenna array has large spatial coherence because antennas at opposite ends of the array emit with a fixed phase-relationship. Spatial coherence of laser beams manifests itself e.g. as speckle patterns. Holography requires light with a long coherence time. In contrast, optical coherence tomography uses light with a short coherence time.

In the case of femtosecond laserpulses it might seem counterintuitive that, on the one hand, the broad spectral width of ultrashort pulses suggests a low temporal coherence, but on the other hand different single pulses from the periodic pulse train emitted by the laser can interfere with each other. The answer to this problem is the fact that the Fourier spectrum of the pulse train is not continuous, instead it has the form of a so-called frequency comb (Ye and Cundiff 2005). The coherence time responsible for interference between distant pulses is represented by the spectrally narrow single peaks of the frequency comb. However, the short term decay of the coherence function for single pulses is given by the inverse width of the envelope of the Fourier spectrum. Demonstratively this can be understood by considering the geometry of the experimental setup. With every round trip a single pulse circulating in the Ti:Sa laser cavity creates a new intensity peak in the emitted pulse train. Due to the exact nature of the repetition there is a strong phase relation between emitted subsequent pulses. Hence long temporal coherence exists, but is only detectable for time delays allowing pulse overlap.

Beyond that, the pulse in question has not only a temporal Gaussian profile in the direction of propagation, but also a two-dimensional Gaussian distribution perpendicular to it. However, for particle characterization purposes, this variation in spatial coherence does not effect the detected Mie scattering, because the beam waist of the utilized laser exceeds by far the size of the investigated small particles.

2.2 Optical Resonators and Nonlinear Optics

As outlined, coherence influences the scattering and detection of femtosecond laser pulses. The corresponding effect of interference stands at the very beginning of constructing laser illumination and therefore laser pulses within optical resonators.

While transversal modes are a physical necessity of electromagnetic wave propagation, longitudinal modes are a property of light amplification in optical resonators. To cause a standing electromagnetic wave between two mirrors of a laser cavity, constructive interference has to be established. That is why the cavity length L

has to be an integer multiple of half the corresponding wavelength. with T as wave period, c the velocity of light, the wavelength $\lambda = cT$ and n a positive integer the standing wave condition for a cavity is

$$\frac{ncT}{2} = L, \ \frac{2L}{c} = T \ (n = 1) \tag{2.7}$$

T(L) is therefore the spacing between frequencies supported by the resonator, given by the length of the resonator. Of course only the frequencies matching the properties of the gain medium are amplified due to stimulated emission.

The condition 2.7 is essential to the process of mode-locking described in chapter 2.3 and also provides the frame for the period of a pulse train and the repetition rate in which a mode-locked Ti:Sapphire laser can operate.

So far the superposition principle for electromagnetic waves was assumed inside the optical resonator. Linear optics describes the interaction of light and matter for low-intensity light sources like light bulbs and broad daylight. The electromagnetic field $\vec{E}$ and the intensity of the source do not change the well-known properties of reflection, refraction, or absorption. Simple refraction e.g., as described by the law of Snellius, is a so-called first-order effect, because only the first term of the expanded macroscopic polarization $\vec{P}$ of a medium is relevant (ϵ_0 stands for electric permittivity and χ is called susceptibility):

$$\frac{\vec{P}}{\epsilon_0} \ = \ \chi^{(1)}\vec{E} \ + \ \chi^{(2)}\vec{E}\vec{E} \ + \ \chi^{(3)}\vec{E}\vec{E}\vec{E} \ + \ ... \tag{2.8}$$

The invention of the laser was crucial for reaching high energy densities ($>$ 1 kW/cm^2) in light beams. In such a case more terms of equation (2.8) have to be considered, and therefore many higher degree effects like frequency doubling or the Kerr-effect (chapter 2.3). This is known as nonlinear optics. In nonlinear optics the response of the medium varies with the beam intensity. In the case of ultrashort laser pulses and the Kerr-effect the additional medium is positioned within the optical resonator.

2.3 Kerr-Effect and Mode-Locking

In classical linear optics light is emitted by harmonic electronic dipoles. For high excitation intensities, the oscillations become strongly inharmonic. The dipoles then radiate at multiple integers of the original frequency. Second harmonic generation combines two photons of the same angular frequency ω. When passing through an appropriate material, they can add up to a single photon with double the original frequency. Commonly this is implemented by using solid state lasers. Nd:YAG lasers emit at $\lambda = 1.06$ μm, the wavelength after frequency-doubling is therefore $\lambda = 532$ nm. Second-order susceptibility (constants of proportionality in equation 2.8) makes possible similar effects in which a photon is either split apart or two photons are mixed. Third-order susceptibility involves four photons. For example, three photons can be mixed into one high-frequency photon. Conversely, a single photon can be split into three lower frequency photons. Also, two photons can be mixed to generate two frequency shifted photons. In contrast to second-order susceptibility, this effect also occurs in centrosymmetric materials. Also, they are observable in liquids and amorphous matter. While the efficiency of effects due to third-order susceptibility is low, they are relevant for the generation of ultrashort laser pulses due to variations of the index of refraction induced by high excitation intensities in e.g. solid state gain media. The dielectric response of an electromagnetic wave with high energy density traveling through an isotropic medium is:

$$\varepsilon_t = \varepsilon + \varepsilon_2 \langle \vec{E}\,\vec{E} \rangle \tag{2.9}$$

ε_1 is missing due to the assumed centrosymmetric medium. The index of refraction is given by the square root of the dielectric function:

$$n = \sqrt{\varepsilon_t} = \sqrt{\varepsilon + \varepsilon_2 \langle \vec{E}\,\vec{E} \rangle} \approx n_0 + n_2 \langle \vec{E}\,\vec{E} \rangle \tag{2.10}$$

Therefore, because the squared absolute value of the electric field gives the intensity of the light beam:

$$n = n_0 + \frac{1}{2} n_2 I \tag{2.11}$$

We assume a Gaussian laser beam in a third-order susceptibility material with a shape parameter g. Therefore, the refractive index distribution is:

$$n(r) = n_0 + \frac{1}{2} n_2 I(r),\ I(r) = \exp[-gr^2] \tag{2.12}$$

for $n_2 < 0$ the refractive index of the material is then largest at the center of the Gaussian beam. Thus, the material becomes a lens which focuses the Gaussian beam. Because a focused beam has a larger intensity the beam is focused even more. This process of self-focussing is called Kerr-Lens Effect and eventually stops due to linear diffraction. It is exploited in connection with mode-locking in titanium doped sapphire lasers to generate ultrashort laser pulses.

A laser cavity generates oscillations over all resonance frequencies for which the gain is greater then the losses. The output intensity is therefore not necessary constant with time. The time distribution depends primarily on the phase relations between the different longitudinal modes. For random phase differences between the longitudinal modes, the time distribution of the output intensity has a random distribution of local maximas. When the modes oscillate with the same initial phase, the time distribution is a periodic repetition of a wave packet due to constructive interference of the modes. Therefore the output intensity of the laser will be a periodic succession of individual pulses, with a temporal width of the order of the inverse of the gain curve width: $\Delta t = 1/\Delta\nu$. The repetition rate of the pulses is given by the geometry of the cavity: $T = 2L/c$. This is the so called mode-locking regime, and the pulses are Fourier-transform-limited.

The different temporal intensity distributions for the cases with random phase and fixed phase become more clear if the beat terms of the involved modes are considered. As a first step we consider two modes E_{M1} and E_{M2} linearly polarized in the same direction:

$$E_{M1} = E_1 cos[\omega_1 t + \phi_1(t)] \tag{2.13}$$

$$E_{M2} = E_2 cos[\omega_2 t + \phi_2(t)] \tag{2.14}$$

The time distribution of the output intensity will therefore follow the time relation of the phase factors $\phi_1(t)$ and $\phi_2(t)$. Because a common detector receiving the temporal intensity distribution has a response time t_r substantially larger than the optical oscillation periods, the measured intensity is a mean value over t_r:

$$\langle I \rangle = \frac{E_1^2}{2} + \frac{E_2^2}{2} + \frac{E_1 E_2}{t_r} \int_0^{t_r} cos[(\omega_1 - \omega_2)t + \phi_1(t) - \phi_2(t)]dt \tag{2.15}$$

The third term of equation (2.15) describes the beating between the two modes. If the phase factors $\phi_1(t)$ and $\phi_2(t)$ vary randomly with time, the changes in the output intensity are much shorter in time than the response time t_r of the detector and cannot be measured. If the two modes with independent phase factors would generate an intensity fluctuation in the range of the response time, a detector would measure intensity fluctuations with a random phase. For a large number of N modes this would again result in non-periodic intensity fluctuations. For perfectly correlated phase factors $\phi_1(t)$ - $\phi_2(t) = 0$ of the two modes however, equation (2.15) shows that the temporal output intensity will vary sinusoidal with a period $\Delta T = (2\pi)/(\omega_1 - \omega_2)$. This can be generalized to an infinite number of phase-locked modes $\phi_i(t)$ - $\phi_j(t) = 0$ (for all *i,j*). In this case the total electric field is:

$$E(t) = \sum_{-\infty}^{+\infty} E_n exp(i\omega_n t), \quad \omega_n = \omega_0 + n\Delta\omega \tag{2.16}$$

$\omega = 2\pi c/2L$ is the interval between neighbouring modes. Therefore the total electric field can be rewritten to:

$$E(t) = exp(i\omega_0 t) \sum_{-\infty}^{+\infty} E_n exp(in\Delta\omega t) \tag{2.17}$$

Thus the total electric field oscillates with the frequency ω_0 but is modulated with a slow period $T = 2\pi/\Delta\omega = 2L/c$. The modulation is due to the sum

in equation (2.17), which can be interpreted as Fourier series. For a Gaussian distribution of amplitudes E_n around a central frequency ω_0 the mean output intensity is approximately proportional to a Gaussian in time, hence a pulse:

$$\langle I \rangle = E(t)E^*(t) \propto exp\left[-\left(\frac{2t}{t_p}\right)^2 ln2\right], \quad t_p = \frac{2\sqrt{2}}{\pi\Delta\omega_0} ln2 \tag{2.18}$$

t_p is the total pulse duration at half maximum and $\Delta\omega_0$ the width at half maximum of the full field distribution. Ultimately the pulse forms at a specific location in the cavity because the involved modes interfere destructively anywhere but at this location. The position of the pulse within the cavity shifts periodically with time, obeying the equation $T = 2L/c$.

A Gaussian amplitude distribution of the modes is not mandatory for mode-locking. The shape of the amplitude only influences the shape of the pulse. The pulse duration and repetition rate remain unaltered. Due to the competition of different modes for amplification by the gain medium strong fluctuations in phase relations and amplitudes of the modes are observed. In passive mode-locking a saturable absorber is added to the cavity in order to enhance the intensity of stronger maxima at the expense of weaker maxima. Finally, the involved energy is collected in one single pulse. Equivalently, in the frequency domain, the according phase relations are established. Active mode-locking describes the process of modulating the modes from the outside with a frequency around the desired interval $T = 2L/c$, for example with an acousto-optical modulator.

For this study a titanium doped sapphire laser was used. A Ti:Sa Laser has a width at half maximum full field distribution of up to $\Delta\omega_0 = 400$ nm, while the central wavelength is typically at the lower end of the visible spectrum around $\nu_{center} = 750$ nm. This corresponds to a pulse length of as short as $t_p = 3$ fs, which is reached without external pulse shaping. Pulse lengths of $t_p = 100$ fs are commercially well available. Moreover, synthetic sapphire has, at low temperature, a thermal conductivity similar to metal. Hence continuous wave (CW) optical pumping is feasible on the scale of watts. A Ti:Sa Laser exploits the Kerr-lens effect to establish self-locking of the modes. The effect is also called Kerr-lens mode locking. No additional saturable absorber is needed. A Gaussian beam is exposed to an inhomogeneous refractive index due to the Kerr-effect. For stronger intensities the refraction is stronger, so the amplifying medium behaves like a lens. This means that stronger intensity maximas in the cavity will be focused far more strongly than the weak ones. This leads to mode-locking. The pulses become

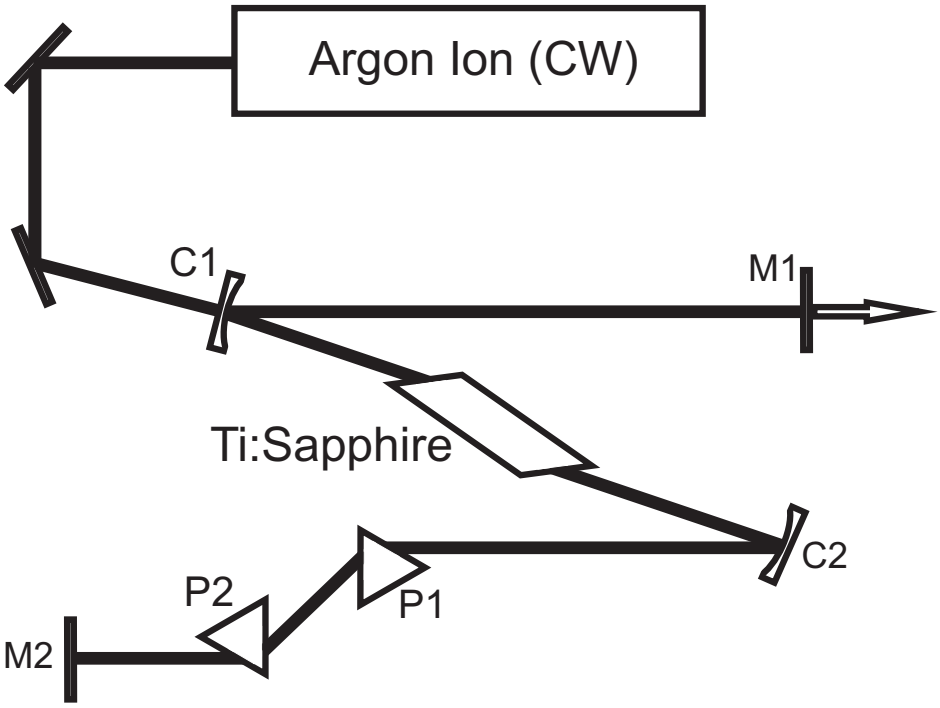

Figure 2.1: Cavity setup of a self mode locked Ti:Sa laser using the Kerr-lens effect.

shorter because the amplifying medium also acts as saturable absorber. At some point of course the diffraction and the imperfect geometry of the cavity limit the shortening, and a minimum pulse length is reached.

Figure 2.1 depicts the most important components of a common Ti:Sa Laser setup. The pump source is an argon ion laser operating in CW mode. The beam is directed into the cavity limited by the mirrors C_1, C_2, M_1, M_2 and passes the Ti:Al_2O_3 crystal. The process of pulse shortening is weakend by the dispersion of the wave group velocity, which tends to lengthen the pulse. The Prisms P_1 and P_2 counter the dispersion of the group velocity within the cavity. In this configuration the laser does not construct pulses voluntary. Pulses can be initiated by creating a minimal local inhomogeneity in the beam intensity, for example by knocking lightly on the fixture of the cavity. This triggers the Kerr-lens mode locking. The process can be aided by adding a slit to the optical path. It increases the difference between the losses experienced by the weaker intensities and intensity maxima. Ultimately a pulse travels back and forth in the cavity while keeping its shape.

2.4 Dispersion

Laser pulses emitted by, e.g., the discussed Ti:Sapphire laser system can reach energy densities at the scale of petawatts. Ultrashort laser pulses not only differ from linear optics because of high peak powers but also due to dispersion. The material response to various wavelengths matters because of the extreme spectral width of pulses in the femtosecond regime. This is important to consider for the illuminated components of experimental setups.

Ultrashort pulse lengths in the order of $t_p = 10$ fs correspond to a very wide spectral bandwidth. The spectral bandwidths (full width at half maximum) of the numerically utilized pulse lengths in this work are $\lambda = 90$ nm, 45 nm, 18 nm and 7 nm for $t_p = 10$ fs, 20 fs, 50 fs and 200 fs respectively. The propagation of such a pulse through a transparent but dispersive medium results in a duration broadening of the pulse and a frequency chirp. This behaviour can be quantified, on the basis of the expression for a Gaussian pulse in the frequency domain:

$$E_0(\omega) = exp\left(\frac{-(\omega-\omega_0)^2}{4\Gamma}\right) \tag{2.19}$$

Γ is the shape factor of the Gaussian envelope. For a pulse that travels a distance x, equation (2.19) can be expanded to:

$$E(\omega, x) = E_0(\omega)exp[-ik(\omega)x], \quad k(\omega) = \frac{n\omega}{c} \tag{2.20}$$

If the propagation factor is expanded in Taylor series under the assumption that the spectral bandwidth of the pulse is far smaller in absolute value than the central wavelength, equation (2.20) becomes:

$$E(\omega, x) = exp\left[-ik(\omega_0)x - ik'x(\omega-\omega_0) - \left(\frac{1}{4\Gamma} + \frac{i}{2}k''x\right)(\omega-\omega_0)^2\right] \tag{2.21}$$

The inverse Fourier transform gives the evolution in time of the electric field:

$$\epsilon(t,x) = \sqrt{\frac{\Gamma(x)}{\pi}} exp\left[i\omega_0\left((t - \frac{x}{\nu_\Phi(\omega_0)}\right)\right] exp\left[-\Gamma(x)\left(t - \frac{x}{\nu_\Phi(\omega_0)}\right)^2\right] \quad (2.22)$$

$$\nu_\Phi(\omega_0) = \left(\frac{\omega}{k}\right)_{\omega_0}, \quad \nu_g(\omega_0) = \left(\frac{d\omega}{dk}\right)_{\omega_0}, \quad \frac{1}{\Gamma(x)} = \frac{1}{\Gamma} + 2ik''x \quad (2.23)$$

In common matter, the group velocity is smaller than the phase velocity, $\nu_g < \nu_\Phi$. The second exponential term in (2.22) expresses the distortion of the pulse envelope. To determine the nature of the distortion we rewrite the form factor Γ(x) to:

$$\Gamma(x) = \frac{\Gamma}{1 + \xi^2 x^2} - i\frac{\Gamma\xi x}{1 + \xi^2 x^2}, \quad \xi = 2\Gamma k'' \quad (2.24)$$

A substitution of (2.24) in the second exponential term of (2.22) gives the expression:

$$exp\left[-\frac{\Gamma}{1 + \xi^2 x^2}\left(t - \frac{x}{\nu_g}\right)^2 + i\frac{\Gamma\xi x}{1 + \xi^2 x^2}\left(t - \frac{x}{\nu_g}\right)^2\right] \quad (2.25)$$

The real term in (2.25) is a Gaussian function delayed in time with a shape factor

$$\frac{\Gamma}{1 + \xi^2 x^2} \quad (2.26)$$

This new shape factor remains smaller than Γ. The pulse is therefore subject to a duration broadening when it propagates through a transparent but dispersive medium. Also, the imaginary term of expression (2.25), the phase, includes a quadratic temporal term. Because the frequency is given by the time derivative of the phase Φ, it then must change linearly:

$$\omega(t) = \frac{\partial \Phi}{\partial t} = \alpha\omega_0 + \beta t, \quad \alpha, \beta > 0 \tag{2.27}$$

This results in a linear frequency chirp in the pulse. That is the leading edge of the pulse shifts to lower and the tail to higher frequencies.

The effects of duration broadening and frequency chirp scale with the traveled distance in the medium and are to be considered and corrected for experimental setups including lenses. This can be done with an optical compressor consisting of two appropriate gratings. In the compressor the components of a pulse with different wavelengths have different optical paths. This corrects group velocity distortions.

In this work however pulses of $t_p = 200$ fs have been used experimentally, mainly on droplets of water. The according spectral width of $\Delta\omega = 7$ nm causes only negligible distortions in lenses and filters used in experimental setups. To investigate shorter pulse lengths numerically, the results by Quan and Fry (1995) have been utilized to calculate the wavelength dependence of the refractive index of water. For wavelengths from $\lambda = 200$ nm to $\lambda = 1100$ nm the refractive index of water is given by:

$$n(\lambda) = 1.31279 + 15.762\lambda^{-1} - 4382\lambda^{-2} + 1.1455E + 6\lambda^{-3} \tag{2.28}$$

For small particle characterization the necessary pulse length declines together with the distance traveled within the medium. To investigate a $d_p = 5$ μm particle a $t_p = 10$ fs pulse with a broad spectral width is appropriate. But then again the traveled distance within the particle is only a few times the wavelength and can therefore be neglected which is relevant for the results in chapter 3.5.

2.5 Alternative Methods for Generation of Femtosecond Laserpulses

For a laser to operate so-called population inversion of electronic states in the gain medium is necessary. In a gas laser this evidently takes place between electronic

levels in gas atoms and molecules. Other gain media are plasmas of ions and metal vapours. Electrical discharges inside a sealed cavity induce energy and therefore excited electronic states. Unbound atoms themselves have states with energetically narrow bandwidths, but while moving around freely with a distribution of velocities the electronic states are shifted according to the Doppler effect. For this reason the emitted radiation by a gas is spectrally broadened. In a gas laser an accousto-optical cell can be used to create active mode-locking, for example with ionized argon. Unfortunately, the spectral region available for gain extends only over a few dozen modes. That is why the shortest pulses achievable in this manner are in the range of a few hundreds of picoseconds. To nevertheless reach the femtosecond regime, a significant effort in external pulse shaping with gratings and single mode fibers is necessary (Nikolaus and Grischkowsky 1983).

In liquids the density of atoms is higher and with it the optical yield, compared to gases. This is true even though the critical organic dye molecules used for population inversion are dissolved in solvents like alcohols or water. On the one hand the velocity of the molecules in their solvent is significantly smaller than the speed of atoms in a gas, so Doppler broadening can be neglected. On the other hand, compared to gases, the electronic states depend profoundly on the molecular environment. The interactions of electron clouds of neighboring molecules results in a spectral broadening. This allows for a spectral width of up to a few dozen nanometers, and is therefore sufficient for the generation of femtosecond laserpulses (Yariv 1975).

To establish ultrashort pulses the dye in the solvent can be used as gain medium in a so-called colliding-pulse mode-locked (CPM) dye laser (Fork et al. 1983). A ring laser cavity is pumped by a CW argon laser and passively mode locked by a saturable absorber inside the resonator. The laser pulses travel in both directions inside the ring resonator. The saturable absorber, which can be a dye, too, is selected to have a concentration such that it only saturates when two pulses pass through simultaneously. As a consequence, the two pulses synchronize their motion inside the cavity. To maximize the net gain per round trip the absorber is placed at a location where the path length to the gain medium is one quarter of the total ring length. This stable operation is called colliding-pulse mode-locking and results in pulse lengths as low as $t_p = 50$ fs.

Preferable to both a gas or dye are solid state gain media, due to their even higher mass density. Titanium-doped aluminium oxide (Ti:Sa) is a very effective gain medium, because the titanium ion is notably larger than the aluminium ion. This leads to significant distortions of the local electronic states within the sapphire structure. The ground and excited states of the Titanium ion couple strongly with the vibrational modes of the surrounding molecules, which leads to strong spectral

broadening.

Optical solitons can be utilized to compress femtosecond laserpulses to even shorter pulse lengths by coupling the emission of broadband infrared lasers, such as the Ti:Sapphire laser or color-center lasers, into fused quartz fibers. Such a system is called a soliton laser (Mollenauer et al. 1980). An optical fiber can have an intensity-dependent refractive index $n = n_0 + n_1 I(\mathrm{t})$. While the high spectral width of a pulse leads to spatial broadening in a medium with normal negative dispersion ($dn_0 \,/\, d\lambda < 0$), the opposite happens in a medium with positive dispersion ($dn_0 \,/\, d\lambda > 0$): The pulse is compressed. This characteristic can be found in fused quartz fibers for $\lambda > 1.3\ \mu m$ (Midwinter 1979). For a fitting pulse intensity the positive and negative dispersion caused by n_0 and $n_1 I(\mathrm{t})$ cancel each other out. The pulse therefore propagates through the fiber without changing its temporal profile. In this state the pulse is called a soliton. If the intensity dependent refractive index is computed for a Gaussian pulse envelope, higher order solitons are obtained. For this solitons the pulswidth oscillates around its inital form while propagating through the medium. Therefore the inital pulselength is shortened at certain positions within the fiber where it can be decoupled.

While the alternatives discussed so far are mostly suitable in pulse length and emitted intensity to provide the experimental results discussed in the work at hand, they are as spacious, and mostly as care intensive and expensive as the Ti:Sa systems already utilized. To lessen the experimental demands for future applications in particle characterization with time integrated and eventually time resolved detection, the femtosecond diode laser, as another variation of solid state gain media, should be considered. Such a device can generate ultrashort laser pulses by e.g. applying passive mode-locking. For instance, the saturable absorber inside the cavity of the laser may be a special quantum well structure. Broadband gain diodes emit strongly chirped light pulses which can be compressed to $t_p =$ 150 fs (Azouz et al. 1995). Principally the pulse will in addition experience self-narrowing by propagating through the semiconductor material (Lami et al. 1999).

Mode-locking is, while most widely used, not the only way to create femtosecond laserpulses. Distributed Feedback Dye Lasers (DFDL) do not utilize a mirror cavity (Shank et al. 1971). The feedback needed to generate a laser resonance is established by a periodic spatial modulation of the gain medium. A pump beam is split in two by using symmetrical diffraction orders of a grating. The two resulting beams are superimposed in a dye cell, causing an interference pattern. Regions of constructive interference create periodic gain regions in the amplifying medium. The gain medium modulation partly reflects waves with half the wavelength equal to the optical thickness of the modulation period. Amplified spontaneous emission is partially reflected back and forth in the distribution structure and further am-

plified by stimulated emission. When the excitation intensity surpasses the laser threshold, a pulse in the femtosecond regime is generated.

2.6 Other Sources of Short Coherence Length

While femtosecond laserpulses are not the only source of spectrally broad emission and therefore short coherence length, they feature experimentally necessary requirements like high energy density and polarization. Moreover, ultrashort laserpulses physically separate the scattering orders of an illuminated particle in time and space. This feature is essential for future work on particle characterization with time resolved instead of integrated detection. However, devices like CW semiconductor laserdiodes do not reach the high output intensities of a Ti:Sa system, but are lower priced and a physically smaller alternative for applications requiring only short coherence length.

A semiconductor is a material with a weak ability to conduct charge carriers. Typically, semiconductors consist of a poor conductor which has been doped with a small amount of impurities. In the case of light emitting diodes, the conductor material is typically aluminium-gallium-arsenide (AlGaAs). In pure aluminium-gallium-arsenide the atoms bond consistently to their neighbors, leaving no free electrons to conduct electric current. In doped material additional atoms add free electrons (n-type semiconductor) or positively charged holes (p-type semiconductor). If voltage is applied to n-type material, free electrons move from a negatively-charged area to a positively charged area. A semiconductor with extra holes is called p-type material, since it effectively has extra positively-charged particles. A diode consists of n-type material which is joined with a section of p-type material. This arrangement conducts electricity in only one direction. When no voltage is applied to the diode, electrons from the n-type material fill holes from the p-type material along the junction between the layers, forming a depletion zone. In a depletion zone, the semiconductor material is returned to its original insulating state because all of the holes are filled, so there are no free electrons or empty spaces for electrons, and the flow of charge carriers is prevented. To undo the depletion zone, the n-type side of the diode has to be connected to the negative end of a circuit and the p-type side to the positive end. The free electrons in the n-type material are repelled by the negative electrode and drawn to the positive electrode. The holes in the p-type material move the other way. When the voltage difference between the electrodes is high enough, the electrons in the depletion zone part out of their holes and begin moving freely again. The depletion zone disappears, and charge moves across the diode. Free electrons moving across a diode can nevertheless recombine with positive charge carriers from the p-type layer. During such a transition from the conduction band to a lower orbital the

electrons release energy in the form of photons. In light emitting diodes (LED) the doped semiconductor is choosen to emit around a desired frequency, mostly in the visible and near infrared spectrum. The spectral width varies from a dozen to a few hundred nanometers. At the lower end, this leads to a coherence length suitable for applications discussed in this work. Moreover, broadband LED´s can be combined with spectral filters to adjust the output intensity´s coherence length to the application. Also, an external cavity incorporating, e.g., an optical grating can be used to narrow the spectrum of a light emitting diode. The possibilities of applying cost efficient broadband LED´s for particle characterization in combination with fluorescence and the time-shift technique (Damaschke et al. 2002a) have been investigated in Koroll (2009).

In semiconductor-laserdiodes (e.g. Agrawal 1995) the recombination of charge carriers doesn't occur between well defined energy levels, but between quasi-continuous energy bands called valence and conduction band. By doping the semiconductor material with donators (n-type semiconductor) and acceptors (p-type semiconductor) respectively, the Fermi level of the charge carriers in the semiconductor is lifted to the conduction band and lowered to the valence band. Because the Fermi level is spatially constant in thermal equilibrium, the energy bands at the pn-junction are dislocated by a combination of p- and n-domain. This creates a potential barrier that prevents an outflow of free charge carriers into the neighbouring domain. If an external voltage is applied with antipodal polarity and additional charge carriers are injected, a thin layer at the pn-junction allows for a population inversion which is necessary for laser operation. In this so-called active zone electromagnetic radiation is created by recombination of charge carriers. In an edge emitting laserdiode this radiation is partially reflected, amplified by stimulated emission and eventually emitted. The reflection is possible due to the, in comparison with the ambient atmosphere, high refractive index of the semiconductor material. Therefore no additional mirrors are necessary to design a resonator. As discussed in chapter 5.2, the laser cavity of the semiconductor laserdiode can be combined with an external cavity to allow a resonance condition which leads to a tunable broadband emission very valuably substituting illumination with femtosecond-laserpulses for time integrated detection (Peil et al. 2006).

As indicated by name, the "Vertical Cavity Surface Emitting Laser" (VCSEL, Jewel et al. 1989) emission occurs not parallel but perpendicular to the semiconductor wafer surface. A fundamental difference between a VCSEL and a common edge emitting semiconductor laser is the lack of facet mirrors. This is made possible by the use of two highly reflective distributed Bragg reflector (DBR) mirrors which form a Fabry-Perot laser cavity. The DBR mirrors are needed for longitudinal confinement of light within the laser. They are build of multiple pairs of $\lambda/4$ size higher and lower refractive index layers, made of semiconductors or other

dielectric materials. By spacing the interfaces properly, the reflectivity of each interface adds constructively, producing mirrors with almost full reflectance. If hybrid dielectric DBR mirrors are used, a large refractive index difference between the layers can be achieved, and therefore only a few mirror periods are necessary to obtain high reflectivity. Semiconductor DBR mirrors require a larger number of periods for high reflectivity, due to the lower achieveable refractive index contrast. Furthermore, the composition of the semiconductor layers has to be chosen to be transparent to the laser light. A VCSEL emitting at $\lambda = 850$ nm, e.g., uses AlGaAs and AlAs for the refractive index layers in the DBR mirrors. VCSEL´s have several advantages, like, e.g. a circular, low divergence laser beam, which makes them well suited for beam guidance in any experimental setup. Also, the short cavity length and therefore the small active volume compared to a common edge emitting laser, leads to a very low current ($I = 1$ mA) required for operation. With a spectral width of a few nanometers this devices can deliver illumination with a coherence length in the micrometer range and are therefore another conveniently sized alternative for applications in particle characterization relying only on short coherence length instead of the physical separation of scattering orders in time and space.

Chapter 3

Characteristics of the Scattering Function for Short Coherence Length Laser Sources

When light waves interact with a scattering medium, electrons in the atomic shell are excited and act as scattering centers. As outlined in Pedrotti (2002), the electrons can be interpreted as harmonic oscillators, which complete forced oscillations and therefore act as dipole antennas according to Hertz. For low excitation frequencies a harmonic oscillator follows nearly without lagging behind and has therefore a frequency independent amplitude. For particles significantly smaller then the wavelength, and for low excitation frequencies, this is called Rayleigh-scattering and can be quantified by applying:

$$I_s \propto \omega^4 sin^2 I_{in} \tag{3.1}$$

with incoming intensity I_{in}, emitted intensity I_s and ω as the frequency of light. Therefore the emitted intensity is inversely proportional to the fourth power of the wavelength. An example for this process is the scattering of sunlight in the atmosphere with nitrogen and oxygen as scattering centers. Light with longer wavelength is scattered less by a magnitude compared to light with shorter wavelength. This explains the blue color of a cloud-free daytime sky.

On the other hand, If the sunlight interacts with a particle which has a comparable or larger diameter to the wavelength, the process is called Mie-scattering. The intensity of light scattered by such a particle gives an unique distribution if,

e.g., local maximas are depicted over scattering angle and diameter. For coherent illumination, by, e.g., a laser beam, interference in the far field generates a seemingly unmanageable number of intensity peaks. The distribution depends, amongst others, on refractive index, polarization and wavelength. In the following the numerical construction of this scattering function will be discussed. Because the rigorous numerics of Mie-theory lack direct physical interpretation, Airy-theory is discussed first and illustrated along the first-order rainbow, which is a detail of the overall scattering function essential to rainbow refractometry. When not stated differently perpendicular polarization was assumed because it brings out the examined, favorable rainbow intensity distribution.

3.1 Airy-Theory and the Rainbow

If a fixed, favorable angular position is assumed for a detector, the rainbow phenomena can be illustrated by two partial rays of the same scattering order passing through a spherical particle, as depicted in fig 3.1. Its intensity at the given scattering angle can be calculated by considering the phase difference $\Delta\Phi$ between the two rays. They are parallel in the far field and destructive and constructive interference for different scattering angles results in minima and maxima of the angular intensity distribution. This approach originates in geometrical optics. It is insufficient first of all because geometrical optics originally does not consider the effect of interference and has to be expanded to do so by incorporating the phase relationship between rays. Moreover, even the expanded model does not consider the phenomena of diffraction and therefore develops a singularity at the so-called rainbow angle.

The Airy approach considers diffraction in the rainbow angle by applying Huygens principle. Huygens principle declares that each point on a wave front emits a spherical wave. The envelope of these secondary waves can be interpreted as a new wave front including the effect of constructive interference. As outlined in van Beeck (1997), in accordance to Fresnel, this can be quantified in an expression for the amplitude of an electric field E_P at a point of observation P:

$$E_P = \frac{iexp(-i\omega t)}{\lambda \parallel \vec{r}_{pos} - \vec{r}_p \parallel} \int\int_{pos} exp\left(i\frac{2\pi}{\lambda} \parallel \vec{r}_{pos} - \vec{r}_p \parallel\right) \, d\alpha \tag{3.2}$$

$\vec{r}_{pos}$ is the position vector of the wave front and $\vec{r}_p$ indicates the point of observation. The shortcoming of the Huygens principle however is the prediction of a second

wavefront propagating opposite to the direction of the actual light wave. Therefore the propagation direction of the overall vector $\vec{r}_{pos}$-$\vec{r}_p$ has to be adjacent to the physical propagation.

By adding the Huygens principle to geometrical optics, the distance between the wavefront and the point of observation is described by:

$$\parallel \vec{r}_{pos} - \vec{r}_p \parallel = r_p - v(\Theta - \Theta_{rb}) - h\frac{v^3}{d_p}, \quad h = \frac{sin\Theta_i}{cos^3\Theta_i} \tag{3.3}$$

The wavefront around the rainbow part of the angular intensity distribution can be approximated in geometrical optics by a cubic function f(v). Θ_{rb} is the rainbow angle, Θ_i the angle of incidence of an incoming ray and d_p the particle diameter. With this, the Fresnel integral can be written as:

$$E_p = \frac{iexp[i(\frac{2\pi}{\lambda}r_p - \omega t)]}{\lambda r_p}\int_{-\infty}^{+\infty} exp\left[i\frac{2\pi}{\lambda}\left(-v(\Theta - \Theta_{rb}) - h\frac{v^3}{d_p^2}\right)\right]\, dv \tag{3.4}$$

Equation (3.4) gives the electric field strength in the rainbow region. The term in front of the integral can be dropped to give the dimensionless Airy-function:

$$\Omega_{rb}(z) = \int_0^{\infty} cos\frac{1}{2}\pi(z\delta - \delta^3)\, d\delta,\ \delta = v\left(\frac{4h}{\lambda d_p^2}\right)^{\frac{1}{3}},\ z = -(\Theta - \Theta_{rb})\left(\frac{16d_p^2}{h\lambda^2}\right)^{\frac{1}{3}} \tag{3.5}$$

Ω^2 over z gives the intensity distribution of the Airy-rainbow. $z = 0$ is the angular starting point of the rainbow, called the rainbow angle. Because of the interference between the two involved partial rays, the overall intensity at $z = 0$ is smaller in absolute value compared to the main rainbow maximum which can be found for positive z. For even higher values of z the intensity oscillates between local maxima of ever smaller intensity and local minima. However, the rainbow is only accurately predicted for values near $z = 0$. This includes the main rainbow maximum, but not the secondary maxima. The first secondary maximum is displaced

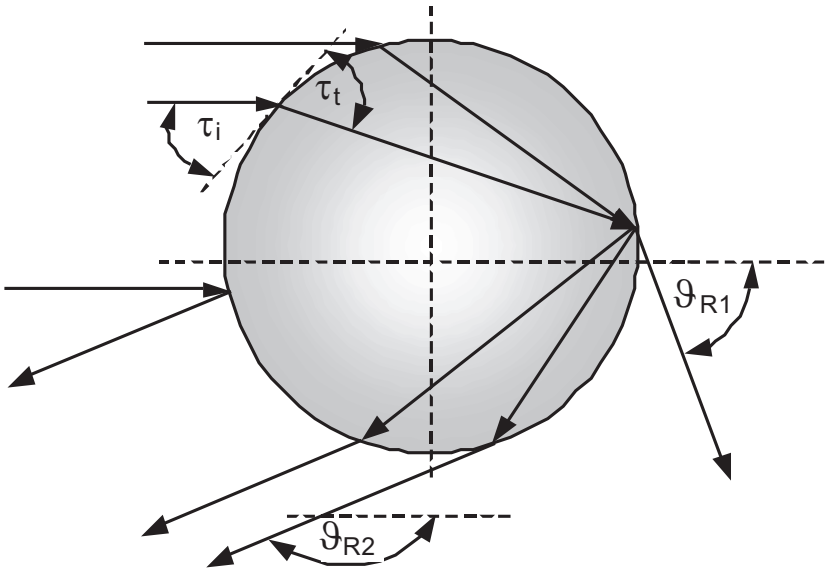

Figure 3.1: Two possibilities of ray transition in a spherical particle in the case of second-order refraction, with detection under the scattering angle Θ_{R2}. Adapted from Bech (2006).

by $\Theta = 0.07°$, which is beyond the tolerance of measurement techniques depending on the positions of the local rainbow maxima to precisely determine particle size and especially temperature for in-situ measurements, as discussed in chapter 3.5.

Significant deviations from the physical angular intensity distribution of the rainbow also occur for particles with diameters smaller then a few hundred microns. For particles in this size range the mentioned two-ray interference in the rainbow angle becomes a three-ray interference pattern. The additional ray is due to surface reflection and adds oscillations with higher angular frequency on top of the two-ray interference. For particles with diameters as low as $d_p = 20$ μm this so-called ripple structure is hardly distinguishable from the Airy oscillations. If a local maxima of the underlying rainbow is recovered by numerical means, its angular position will deviate substantially from the Airy results. For even smaller particles with d_p = 10 μm an additional effect distorting the rainbow becomes noticeable. Surface waves account for a fourth light ray influencing the angular intensity distribution given by the discussed three-ray interference.

Despite the difficulties of quantifying the angular rainbow pattern, geometrical optics is sufficient to calculate the spatial path differences between light rays representing scattering orders or multiple ray paths within a scattering order for defined detection angles (Bech 2006). As depicted in fig. 3.1 it is obvious to assume

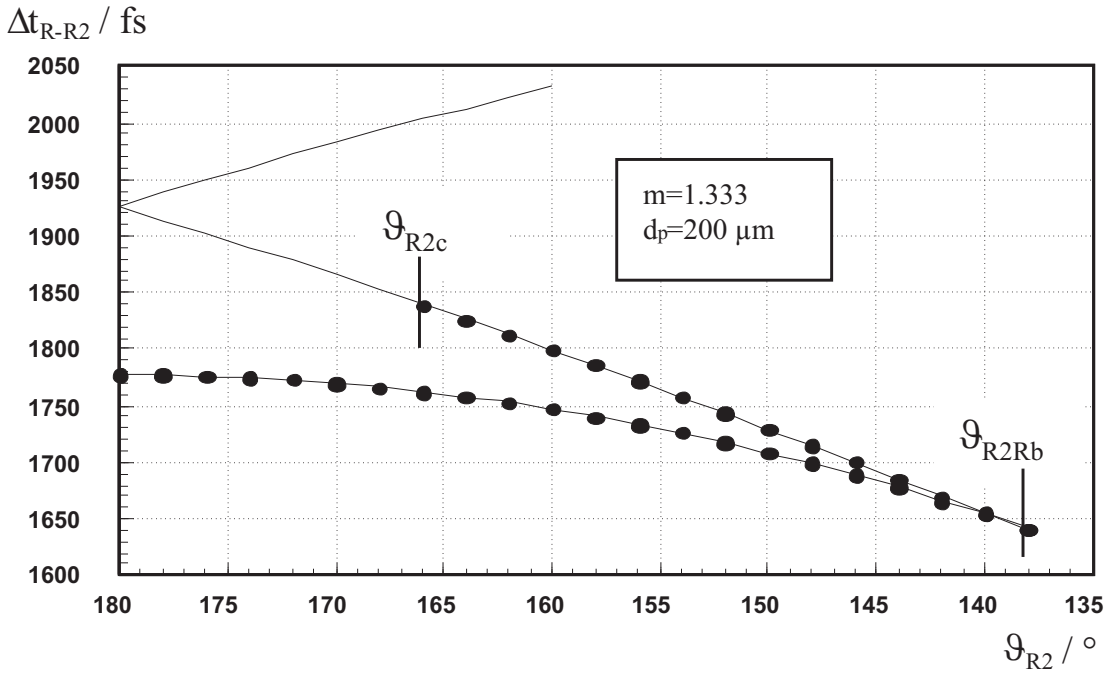

Figure 3.2: Depiction of the time differences Δt_{R-R2} and therefore path differences of Mie calculations (solid curves) and the time differences Δt_{R-R2} calculated by geometrical optics (black full dots) for a particle with $d_p = 200$ μm and $n = 1{,}333$. Considering the time axis, the earlier curve represents reflection and the subsequent curve second-order refraction (longer path). The part of the Mie calculation not covered by the dashed curve exists due to surface waves. Adapted from Bech (2006).

the scattering angle of the rainbow Θ_{R2} not to be exclusively defined by the angle of incidence τ_i. As mentioned before, two paths of ray transit within the particle, with subsequent detection under a unique scattering angle Θ_{R2}, are possible. Therefore a spatially shorter and a longer optical path between the reflection order and the second-order of refraction occur. In the case of coherent illumination this path difference can be physically interpreted as a phase difference between the two rays, leading to interference at a detector in the far field. On the other hand a time difference can be assigned to the spatial interval of the path difference if the velocity of light is considered. This becomes important if ultrashort laser pulses are applied instead of a coherent source. The time difference allows for an assertion whether the extremely short pulses following the discussed ray paths either overlap or are separated in time and space. As outlined in Bech (2006), the associated time differences Δt_{R-RB} to those two path differences can be quantified as follows:

$$\Delta t - R - R2 = \frac{d_p}{c}\left[\sqrt{1+n^2-2ncos\left(\frac{\Theta_{R1}}{2}\right)}+nsin\left(\frac{\Theta_{R2}-\Theta_{R1}}{2}\right)\right] \quad (3.6)$$

For an incident angle $90° \geq \tau_i \geq \tau_{iRB}$ equation (3.6) gives the time difference of the shorter path. τ_{iRB} is the incidence angle resulting in the physically lowest possible absolute value of the rainbow scattering angle. For $\tau_{iRB} \geq \tau_i \geq 0$ the same equation gives the time difference of the longer path. The following equation quantifies the relation between the scattering angle of first order refraction and the angle of incidence τ_i necessary to solve equation (3.6):

$$\Theta_{R1} = 2\left[arccos\left(\frac{cos(\tau_i)}{m}\right)-\tau_i\right] \quad (3.7)$$

Fig. 3.2 compares the time differences Δt_{R-RB} between reflection and the longer path of second-order refraction produced by equation (3.6) with physically more accurate Mie theory. The physically accurate Mie solution is depicted as solid line, while the geometrical solution is given by the dashed curve. Θ_{R2c} is, in absolute value, the highest possible scattering angle for the rainbow based on geometrical optics. Θ_{R2Rb} is the lowest. The angle Θ_{R2c} increases in absolute value with increasing refractive index. For $n = \sqrt{2}$ it reaches $\Theta_{R2c} = 180°$ and therefore completes the long path function predicted by Mie theory.

For refractive indices m $\leq \sqrt{2}$ however, in the angular region in question, the Mie solution is not explainable by pure second-order refraction. To explain this section of the angular intensity distribution without Mie theory, a geometrical approach which includes surface waves is needed. As discussed in Bech (2006), surface waves travel in both clockwise and counterclockwise direction along the particles surface. This results in multiple surface waves with shorter and longer optical path differences. To explain the geometry of surface waves it is assumed that they are generated by tangentially incident rays which emit radiation in tangential direction into the surrounding medium with exponentially decreasing intensity (Nussenzveig 1969a,b). For second-order refraction a grazing incident ray completes a single internal reflection before leaving the surface tangentially. Fig. 3.3 depicts the according ray paths which occur as follows:

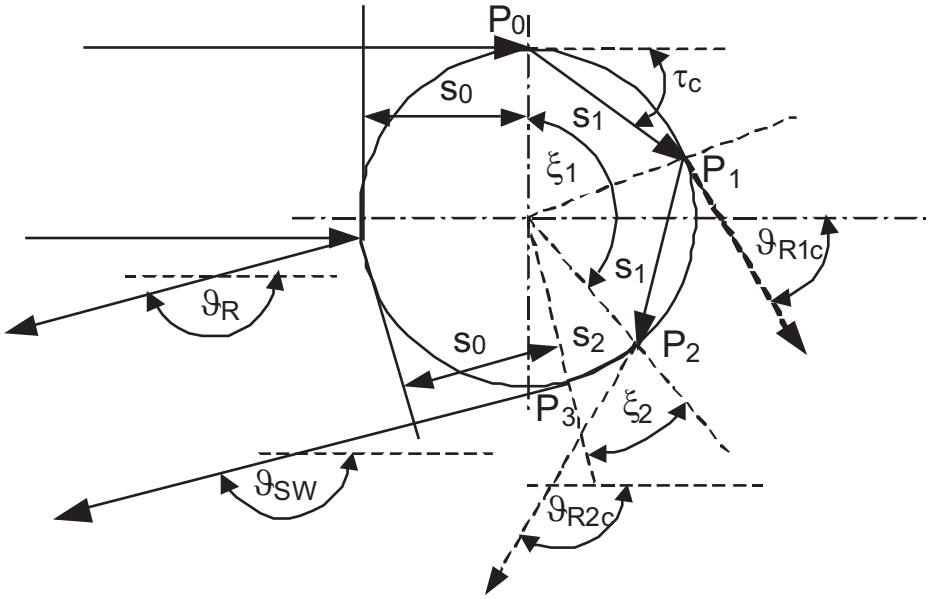

Figure 3.3: Ray path approach to surface waves on spherical particles (shorter path). Adapted from Bech (2006).

The ray with tangential incidence at point P_0 is deflected into the particle by refraction with the critical angle τ_c:

$$\tau_c = arccos\left(\frac{1}{m}\right) \tag{3.8}$$

For a ray with a single internal reflection at point P_1 the two shortcuts s_1 within the particle form an angle of $\xi_1 = 4\tau_c$. At point P_2 the ray is deflected tangentially to the surface of the particle and travels as a surface wave to point P_3, covering the circular arc s_2 with associated angle ξ_2. At P_3 the surface wave is separated from the particle surface and radiates tangentially into the surrounding medium, becoming detectable at the scattering angle Θ_{SW} ($= \Theta_{R2} = \Theta_R$). These geometrical assumptions allow for a quantification of the path difference Δl_s between the shorter surface wave ray path and the reflection order:

$$\Delta l_s = d_p \left[sin\left(\frac{\Theta_{SW}}{2}\right) + 2sin\left(\frac{\Theta_{R2c}}{4}\right) n + \frac{\Theta_{SW} - \Theta_{R2c}}{2} \right] \tag{3.9}$$

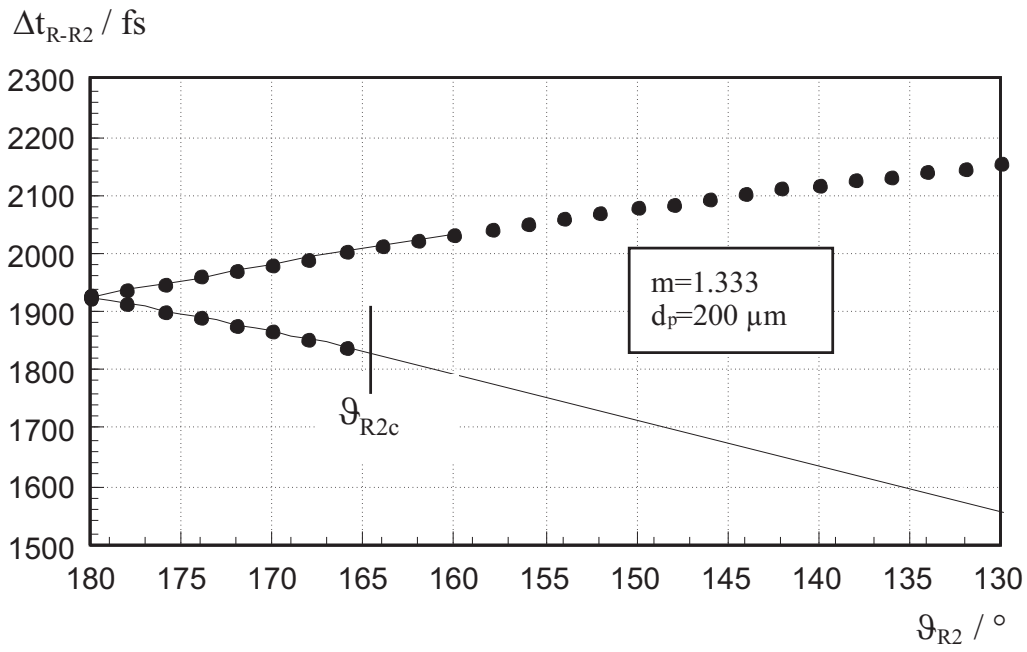

Figure 3.4: Depiction of Mie solutions (solid curve) and results of the geometrical assumptions for the propagation of surface waves for a particle with $d_p = 200$ μm and $n = 1{,}333$ (black full dots). Considering the time axis, the earlier dashed curve represents the shorter path of surface waves geometrically constructed in detail in fig 3.3. Subsequently the later dashed curve represents the longer path length of surface waves. Adapted from Bech (2006).

The first sine in equation (3.9) quantifies the ray path $2s_0$ in the surrounding medium. The two shortcuts $2s_1$ within the particle are expressed by the second sine. Also, the arc s_2 is added. For the longer surface wave path with grazing incidence at the lower edge of the particle, the first two sines of equation (3.9) remain the same. However, the third term has to be adjusted:

$$s_{21} = -\left(\frac{\Theta_{R2c} + \Theta_{R2}}{2} - \pi\right) \tag{3.10}$$

Therefore the optical path difference Δl_1 for the longer surface wave path is quantified as:

$$\Delta l_s = d_p \left[sin\left(\frac{\Theta_{R2}}{2}\right) + 2sin\left(\frac{\Theta_{R2c}}{4}\right) n - \left(\frac{\Theta_{R2c} + \Theta_{R2}}{2} - \pi\right)\right] \tag{3.11}$$

The corresponding time differences are obtained by division with the speed of light in vacuum c_0. With this description the shorter path differences in the angular region $180° \geq \Theta_{R2} \geq \Theta_{R2c}$ and the longer path difference for the range $\Theta_{R2} \leq 180°$ can be explained. However, the detectability of the surface waves declines quickly due to the exponentially decreasing intensity.

In fig. 3.4 the time differences Δt for surface waves quantified by equation (3.9) and (3.11) are depicted as a function of the detection angle $180° \geq \Theta_{R2} \geq \Theta_{R2c}$. Also, the results of the Mie solution for $d_p = 200$ μm and n = 1,333 are added. In fig. 3.2 part of the Mie solution was not fully explainable by the geometrical second-order refraction approach. If the geometrical contribution in fig 3.3 given by the outlined model for surface wave propagation is considered, the results given by Mie theory overlap with the overall geometrical model.

As will be further discussed in chapter 3.4, surface waves set a lower particle size limit to the three-ray approach of rainbow refractometry, which explains the angular intensity distribution of the rainbow region with the two-ray interference of second-order refraction and the additional ray of reflection which evokes further oscillations with higher angular frequency.

3.2 Lorenz-Mie Theory

The Lorenz-Mie theory solves the problem of calculating the scattering of a plane wave of light by an isotropic and homogeneous spherical particle with a given diameter and refractive index (Mie 1908, Lorenz 1890). The particle is numerically characterized by the scattering functions for incident and scattered light. To obtain them the vector wave equations for electromagnetic waves have to be solved with the according boundary conditions (Kerker 1969, Born 1981, Bohren and Huffman 1983, Born and Wolf 1999). This is achieved by introducing a spherical coordinate system and the decomposition of the incident plane wave into spherical partial waves. Due to symmetry the problem can be reduced to a scalar calculation. The sum of the scattered partial waves is the desired scattered field. In the far field the scattering functions are:

$$S_1(\theta_s) = \sum_{n=1}^{\infty} a_n \pi_n(\theta_s) + b_n \tau_n(\theta_s) \tag{3.12}$$

$$S_2(\theta_s) = \sum_{n=1}^{\infty} a_n \tau_n(\theta_s) + b_n \pi_n(\theta_s) \tag{3.13}$$

θ_s is the scattering angle. As a consequence of the description of the problem in spherical coordinates the functions $\pi_n(\theta_s)$ and $\tau_n(\theta s)$ depend on the associated Legendre functions. Similarly, the complex coefficients a_n and b_n depend on Riccati-Bessel functions. They specify the partial wave amplitudes.

The analytical approach is efficient but fails to reflect the physical process of overlapping scattering orders. Geometrical optics is more graphic, but inaccurate. Therefore the Debye-Series decomposition is used as a tool to evaluate the scattering of light by a spherical particle (Debye 1908, Hovenac and Lock 1992).

A particle radiates many scattering orders as a result of illumination. This is due to reflection and refraction at the particle surface. Except for the combination of reflection and diffraction, the Debye-Series establishes individual complex terms representing individual scattering orders. The scattering functions for the far field (3.12/13) can be rewritten to represent only single scattering orders g. They result from the sum of all partial waves describing a single scattering order. Furthermore, a sum of this partial scattering functions $S_1^{(g)}$, $S_2^{(g)}$ gives the original scattering functions (3.12/13):

$$S_1(\theta_s) = \sum_{g=1}^{\infty} S_1^{(g)}(\theta_s), \tag{3.14}$$

$$S_2(\theta_s) = \sum_{g=1}^{\infty} S_2^{(g)}(\theta_s) \tag{3.15}$$

While geometrical optics yields a description for independent scattering orders, the Debye series description adds an in-depth characterization of surface waves and other complex wave phenomena.

3.3 Fourier-Lorenz-Mie Theory

Differing from Lorenz-Mie theory, which characterizes the scattering of a homogeneous plane wave, most applications in particle characterization involve inhomogeneous incident waves. For light scattering by spherical particles this can be described by extending Lorenz-Mie Theory to either (the more common) generalized Lorenz-Mie theory (GLMT) or Fourier-Lorenz-Mie theory (FLMT). In FLMT many individual, monochromatic plane waves are superimposed. This superposition of the involved plane waves results in the total scattered field. GLMT is an analytical extension of the Lorenz-Mie theory for inhomogeneous waves (Gouesbet et al. 1989 and 2000a,b). For the time being GLMT has been extended to radially inhomogeneous spheres (Onofri et al. 1995), cylinders of circular and elliptical cross sections (Ren et al. 1997, Gouesbet and Mees 1999) and to spheroids (Xu et al. 2007, 2008). For the work at hand FLMT was chosen, because of straightforward implementation, and as well straightforward combination with the physically more descriptive Debye-series. This is crucial, because the Debye-series allows the separation of contributions to the scattered angular intensity distribution by various orders. For a sphere, Debye-series has been determined for LMT in Debye (1909) and for GLMT in Gouesbet (2003).

So far only quasi-stationary, monochromatic waves have been considered. The amplitude of the incident wave is therefore temporally constant and the phase evolves linearly in time at all points in space. A laser pulse however is Gaussian in time:

$$E(z,t) = E_0(x,y,z)\exp\left[j\omega_0\left(t-\frac{k}{z_0}z\right)\right]\exp\left[-\frac{8}{t_p^2}\left(t-\frac{k}{z_0}z\right)\right]. \tag{3.16}$$

k represents the wavenumber, t_p the temporal pulse length and E_0 the initial electric field at time $t = 0$ and position $x = 0$.

To compute the total scattered field for a spherical particle with FLMT, this pulse has to be disassembled into a discrete spectrum of waves in the frequency domain (Michel 2002). Presuming an equidistant spacing with the period T, the individual waves are

$$A_i = E_0\frac{1}{2T}\sqrt{\frac{\pi}{2}}\exp\left[-\frac{[(\omega_0 - i\Delta\omega)t_p]^2}{32}\right]. \tag{3.17}$$

A_i are the electric field strength amplitudes with spectral lines at $\omega_i = i\Delta\omega$ with ($\Delta\omega = 2\pi/T$, i = 0, 1, ...). The boundaries of i are:

$$\frac{\omega}{\Delta\omega}\left(1 - \frac{\sqrt{32L}}{\omega_0 t_p}\right) \leq i \leq \frac{\omega}{\Delta\omega}\left(1 + \frac{\sqrt{32L}}{\omega_0 t_p}\right) \tag{3.18}$$

It is reasonable to set a lower limit L for amplitudes. The subsequent error becomes neglectable following $\exp(-L)$, for example for $L = 8$. The spectral lines stand for monochromatic waves. The scattering from the particle is calculated for each single wave. The total scattered field in the time domain is received by application of a reverse Fourier transform:

$$E_s = \sum_{i_{min}}^{i_{max}} E_s(i) \exp(ji\Delta\omega t) \tag{3.19}$$

As established in signal theory and Fourier optics, The broad spectral bandwidth of a laser pulse is equivalent to a short coherence length.

In-depth analysis of this so-called plane wave approximation and plane wave decomposition is provided in Clemmow (1966), Colak (1978), Albrecht (1995) and Damaschke (2003). In Michel (2002) the extension of FLMT to femtosecond laser pulses has been implemented with commercially available software, e.g. MATHCAD and MATLAB. In Damaschke (2003) light scattering for small particles was implemented with an object-oriented programming structure based on C++. For the study at hand this structure was extended to include the description of femtosecond laser pulses for small particles and conveniently vary parameters like droplet size, scattering angle, refractive index, pulse length and central wavelength at the same time.

3.4 Temporal and Spatial Separation of the Scattering Orders

A $t_p = 10$ fs pulse is equivalent to 3 μm pulse length, therefore femtosecond laser pulses correspond to a pulse length in the same order as the diameter of small

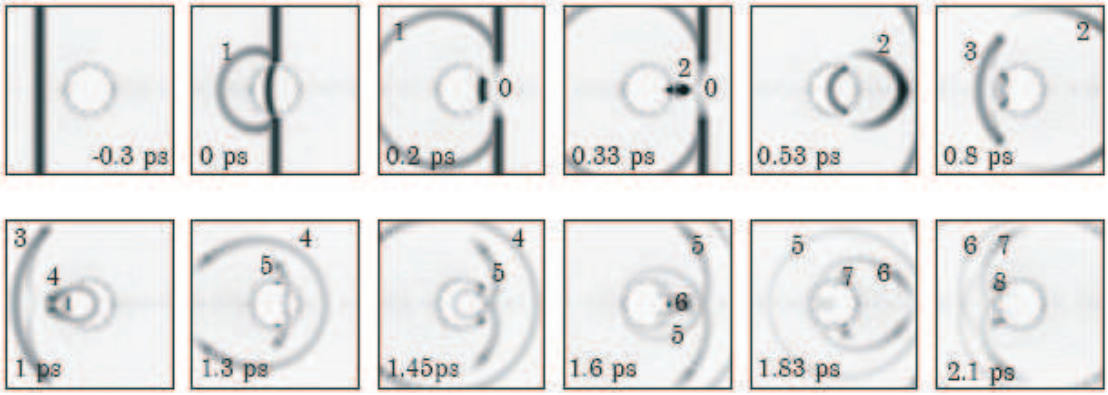

Figure 3.5: Numerical, temporally progressing simulation of the scattering of a sinistrally applied femotsecond laserpulse (t_p = 50 fs) on a spherical, homogenous particle with λ = 600 nm, n = 1,333 and d_p = 100 μm. The time relative to the center of the incident wave is given in each image. In addition the scattering orders are indicated. Adapted from Damaschke (2003).

particles. Consequently scattering orders are leaving the particle temporally and spatially separated. In fig. 3.5 a numerically obtained sequence of temporally progressing diagrams (Damaschke 2003) illustrate the proportions between pulse length and particle size.

The temporal separation of the scattering orders for specific scattering angles and particle-detector distance was also calculated on the basis of FLMT and is depicted in fig 3.6 (Michel 2002). A detector with appropriate temporal resolution would measure the various scattering orders sequentially. The time between the individual intensities depends heavily on detection angle and also on wavelength, polarization and refractive index. The temporal separation increases linearly in absolute value with particle diameter. Such a setup could therefore be used as particle sizing technique, which has not been realized so far experimentally. The sizing of particles with such a method was mentioned by Gouesbet et al. (2000a,b) and Mees et al. (2001a,b,c), and studied in depth by Bech and Leder (2004, 2006), including multi-particle scattering of individual scattering orders.

The scattering orders in fig 3.6 can be identified by using Debye-series decomposition within Fourier-Lorenz-Mie theory. A multi-angle view of the scattered intensities in a specific particle-detector geometry is obtained by calculation of local maximas. In fig 3.7 they are depicted for the full angular intensity distribution over detection time. The angle $\Theta = 0°$ represents the direction of the incoming laser beam and $\Theta = 180°$ is therefore the backscatter direction. In this form of illustration it is easy to locate angular windows in which a presumed detector for

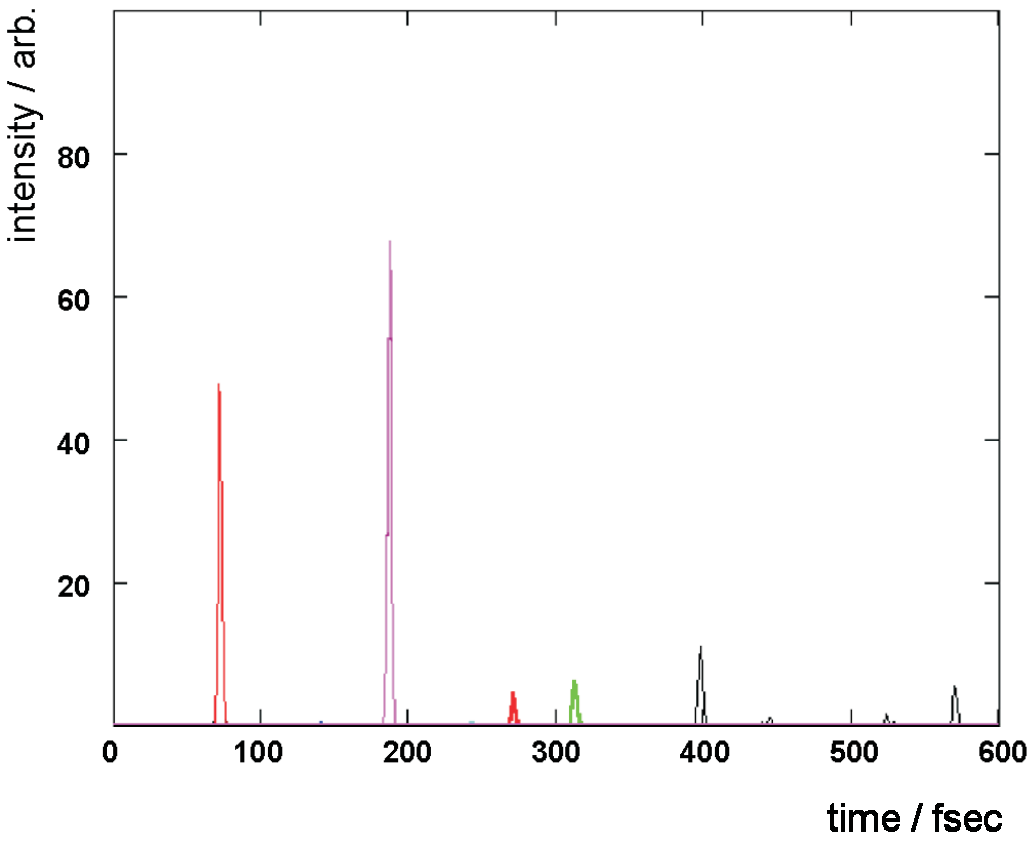

Figure 3.6: Numerical, temporally progressing simulation of the scattering orders given by a femotsecond laserpulse interacting with a spherical particle in direction of the incoming illumination. Adapted from Michel (2002).

temporal resolution of the scattering orders should be positioned. Because of the experimental complexity of temporally resolving intensity peaks in the femtosecond regime it is favorable to find a detection angle with a relatively wide time gap between events. In fig. 3.7, first and second-order refraction can be avoided at an angle of around $\alpha = 118°$ in favor of diffraction and third order refraction. In addition, FLMT gives the absolute values of the intensity peaks. At $\alpha = 118°$ the absolute values of the intensities of diffraction and third-order refraction are identical and therefore easier to detect.

Beside the very high temporal resolution which would be needed for a detector, another limitation is the size of the particle in comparison to the pulse length. If the pulse length is too long compared to the particle size, the scattering orders overlap. In signal theory coherence is defined as the normalized average cross-spectral

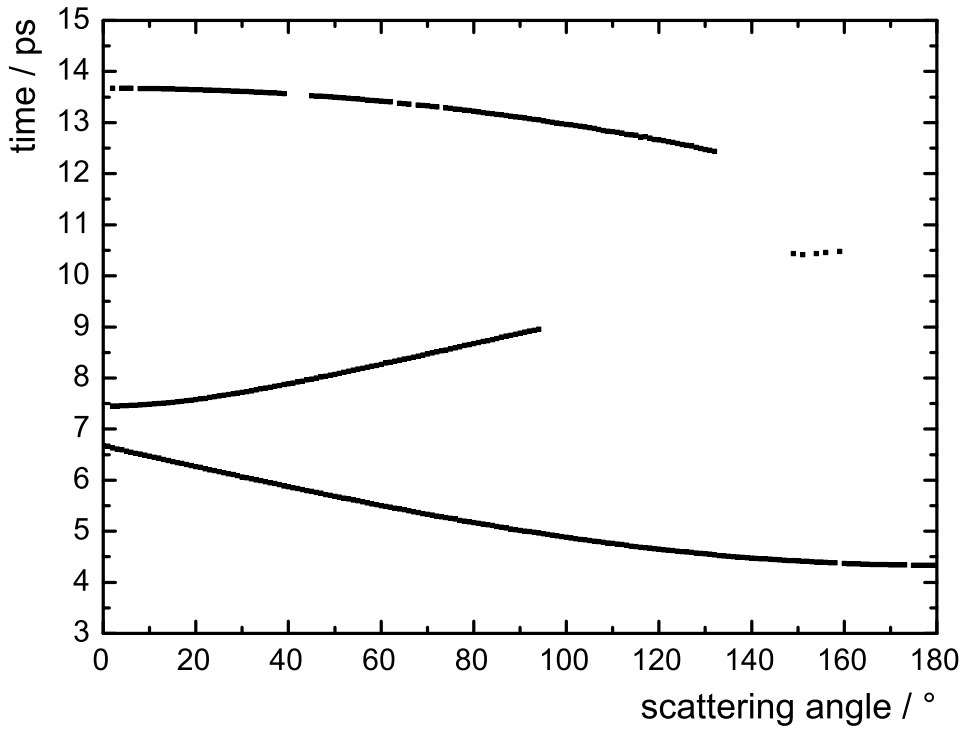

Figure 3.7: Numerical simulation of the scattering of a femotsecond laser pulse (t_p = 50 fs) on a spherical, homogenous particle with λ = 780 nm, n = 1,333 and d_p = 1 mm. The diagramm indicates the time the intensity maxima of a scattering order would need, over the full angular intensity distribution, to reach a detector in a distance of $D = 2$ mm. Scattering orders upwardly in time: Interwined reflection (for higher absolute angles) and diffraction (for lower absolute angles) between t 4 and 7 ps, first order refraction between t = 7 and 9 ps, second order refraction between t = 10 and 11 ps, and third order refraction between t = 12 and 14 ps.

density of two signals. Because in the case at hand the overlap takes place between two copies of the same signal, the degree of coherence can be obtained by considering the power spectral density, which is a special case of the cross-spectral density for identical signals:

$$I \propto (E_{rl} + E_{rr})(E_{rl} + E_{rr})^* = E_{rl}^2 + E_{rr}^2 + 2E_{rl}E_{rr}cos(\Phi_{rl} - \Phi_{rr}) \qquad (3.20)$$

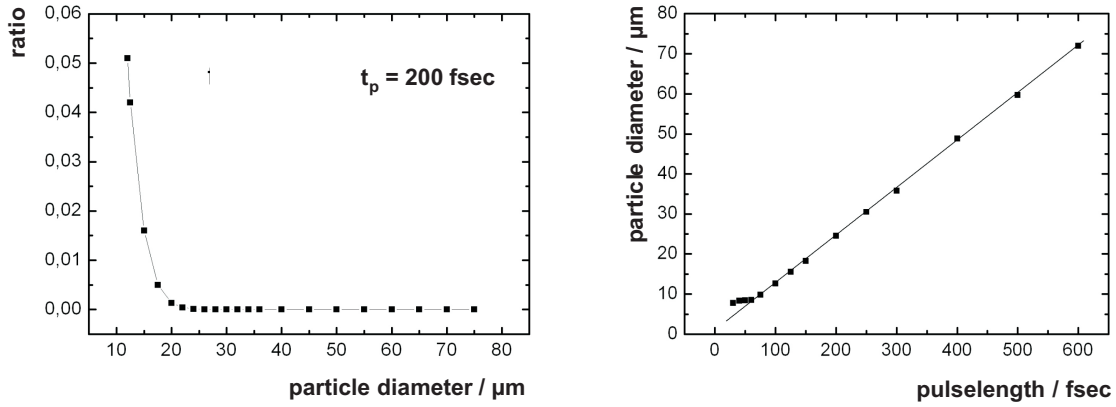

Figure 3.8: left: Ratio between AC and DC part of the intensities of reflection and second-order refraction for a range of particle diameters and $t_{pp} = 200$ fs. right: Connection between particle diameter and laser pulse length for a ratio between AC and DC part of 1/10000.

In equation (3.20) the subscript "rf" stands for reflection and "rr" for second order refraction. The squared electric field components are together the DC part of the signal. The cosine term is the AC part. The absolute value of the AC part rises with increasing overlap and, if normalized with the DC part, gives a measure for the overlap of the assumed scattering orders or rather the degree of coherence between them. For fig. 3.8 the signal parts of second-order refraction and reflection have been determined by Debye-series for a scattering angle $\Theta = 140°$ in the rainbow region. It depicts the ratio for this case between AC and DC part for a range of particle diameters and a laser pulse length of $t_p = 200$ fs. Because a single pulse has a spatial length of $l_p = 60$ μm, and because for second-order refraction it needs to pass up to twice the particle diameter, the absolute value of the AC part rises steeply for $d_p < 30$ μm.

To determine a possible lower particle size limit for the assumption of two-ray interference for the chosen scattering angle, a very low ratio between the AC and DC signal part of 1/10000 was applied, and therefore an extremely well separation of the surface reflection and second-order refraction. In fig 3.8 the pulse lengths necessary for such a separation are depicted over the particle diameter. A pulse length of $t_p = 70$ fs would therefore separate the scattering orders for the assumed ratio for particles with $d_p > 10$ μm. As will be obvious in chapter 3.5, a somewhat higher ratio and therefore a longer pulse length would be sufficient to already significantly reduce the ripple structure in the angular rainbow region. However, the deviation from linearity in fig. 3.8 for particle sizes of $d_p < 10$ μm supports

the assumption, that the geometrical optics approach of two-ray interference is not valid for ever smaller particles. Based on the discussion in chapter 3.1, these deviations presumably occur due to the additional influence of surface waves for particles of this size.

3.5 The Scattering Function and the Rainbow for Pulsed Illumination

The consequences of temporal and spatial separation of the scattering orders for a particle can be observed well and applied in the rainbow region of the angular intensity distribution. As was discussed in chapter 3.1, an angular scattering region which, for fixed angles and in regard to geometrical optics, multiple ray-paths exist for a single scattering order, is called "rainbow". The well known primary rainbow observed in nature originates from the second-order refraction in water droplets. Two separate partial rays of the second-order refraction interfere with each other. This results in intensity maxima and minima in the angular intensity distribution. The diameter of a spherical, homogeneous droplet is characterized by the angular distances between the maxima, while the exact angular positions depend on the refractive index. Far field interference of the second-order refraction with the surface reflexion creates the so-called ripple structure. In fig. 3.9 the numerical angular intensity distributions in the far field of a spherical, homogeneous droplet are displayed for CW and pulsed illumination. Also the individual scattering orders are depicted. The region of the first rainbow is located approximately between the scattering angles of $\Theta = 140°$ and $160°$. Clearly, as outlined in Bakic et al. (2008), for ultrashort pulse illumination, the intensities of the scattering orders add up to give a smoothed Mie sum, compared to the result for CW illumination. Instead, for CW illumination, the electric field vectors add up in the far field. Therefore the scattering orders interfere with each other, creating strong angular oscillations in the Mie sum. The absolute value of the pulse length has to remain non-negligible, because a coherence length of the order of microns is necessary to allow interference between the ray paths within the scattering orders, namely second and third-order refraction. Avoiding coherence completely would remove the intensity modulation of the rainbow, and therefore the information on particle size and refractive index. In fig 3.10 a detail of the numerically obtained, full angular intensity distribution is displayed to point out the importance of the femtosecond time scale. For a particle with $d_p = 20$ μm a pulse length of $t_p = 50$ fs is necessary to smooth the angular intensity distribution completely. If the pulse length increases to only $t_p = 125$ fs, the influence of the reflection order can already be identified. For longer pulse lengths, which remain on a femtosecond timescale, the oscillations due to the overlap between scattering orders become

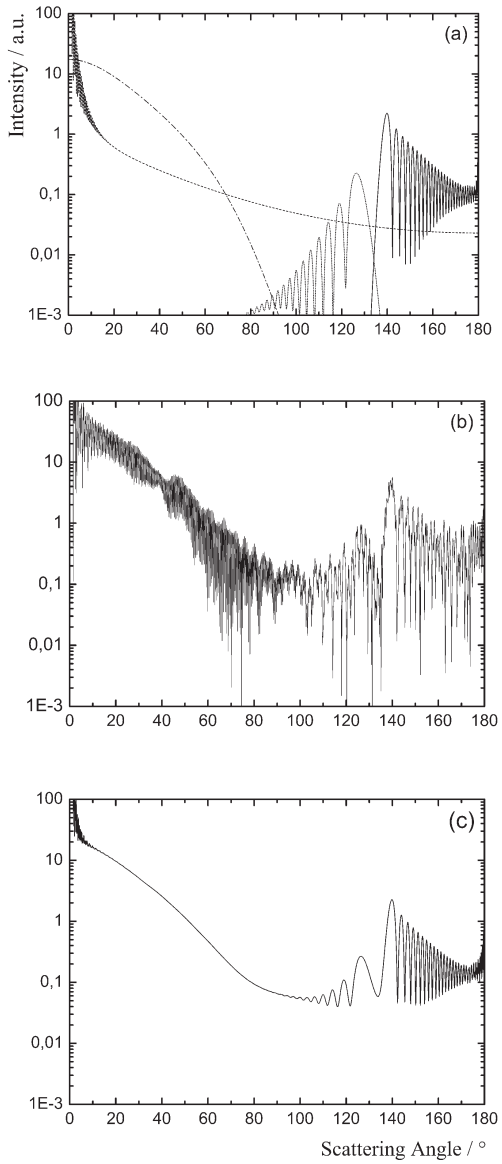

Figure 3.9: Numerical angular intensity distributions in the far field of a spherical, homogeneous droplet ($d_p = 94$ μm, $n = 1{,}333$). (a) Individual scattering orders, namely reflection and diffraction (dashed), first-order refraction (dashed and dotted), second-order (full) and third-order refraction (dotted). (b) The Mie sum is a result of interfering scattering orders for continuous illumination at $\lambda = 780$ nm. (c) Simulated $t_p = 70$ fs pulses at a central wavelength of $\lambda = 780$ nm yield a Mie sum which follows from added intensities of different scattering orders.

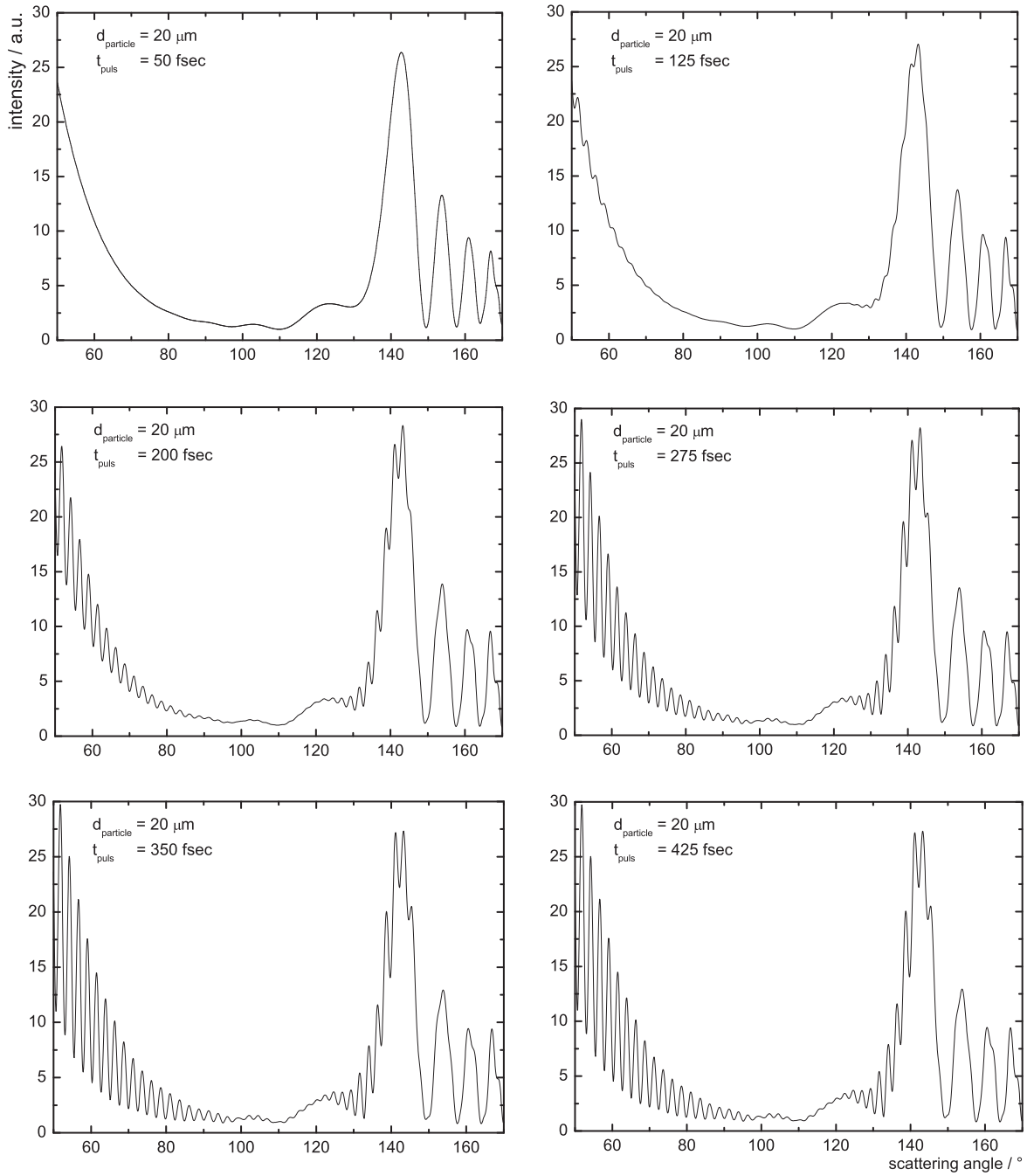

Figure 3.10: Numerically obtained angular intensity distributions in the far field of a spherical, homogeneous droplet ($d_p = 20$ μm, $n = 1{,}333$) for various femtosecond pulse-lengths ($\lambda = 780$ nm).

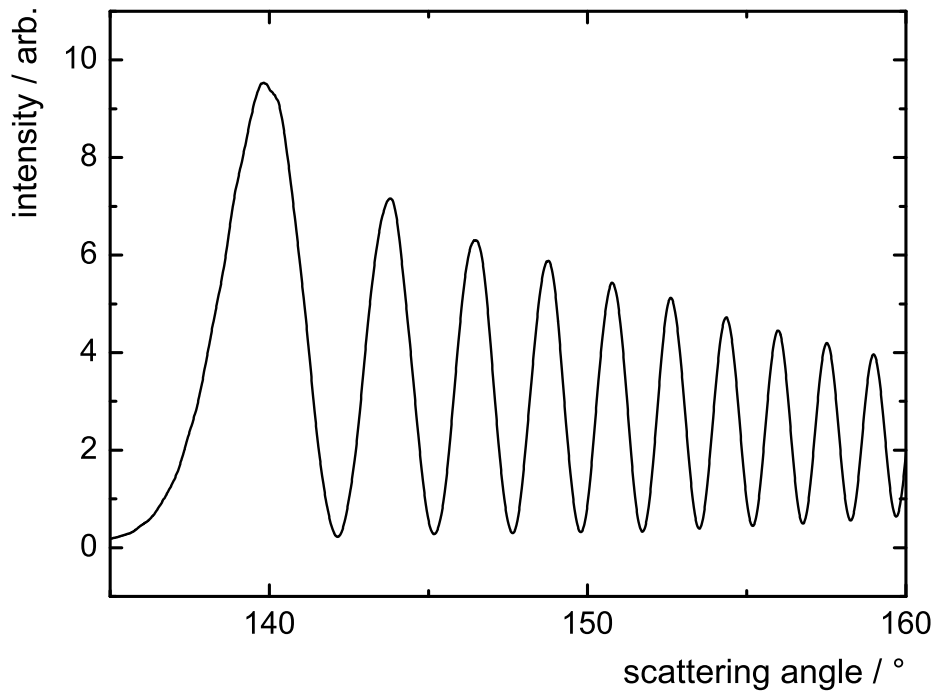

Figure 3.11: Smoothed angular intensity distribution in the rainbow region computed for CW illumination with a coherence length of $l_p = 15$ μm ($d_p = 100$ μm, $\lambda = 780$ nm, $n = 1{,}333$).

more pronounced until they resemble a distribution with CW illumination.

As discussed in chapter 3.4, the significant characteristic of femtosecond laser pulses for time integrated detection is the corresponding coherence length on the scale of microns. FLMT can be utilized to quantify angular intensity distributions of particles illuminated by sources providing a broad spectral width but lacking the phase relationship between the contributing wavelengths. This approach was experimentally investigated in Peil et al. (2006b). The novel semiconductor laser source with optical feedback provided a CW spectral width of $\Delta\lambda = 7$ nm at half maximum, matching the width of the spectral distribution available by application of femtosecond laser pulses with $t_p = 200$ fs. To numerically disregard the phase relationship, the contributions of individual wavelengths to each scattering angle of the overall intensity distribution have been computed with FLMT (as implemented by Damaschke (2003)) and subsequently added up with a MATHCAD routine. For

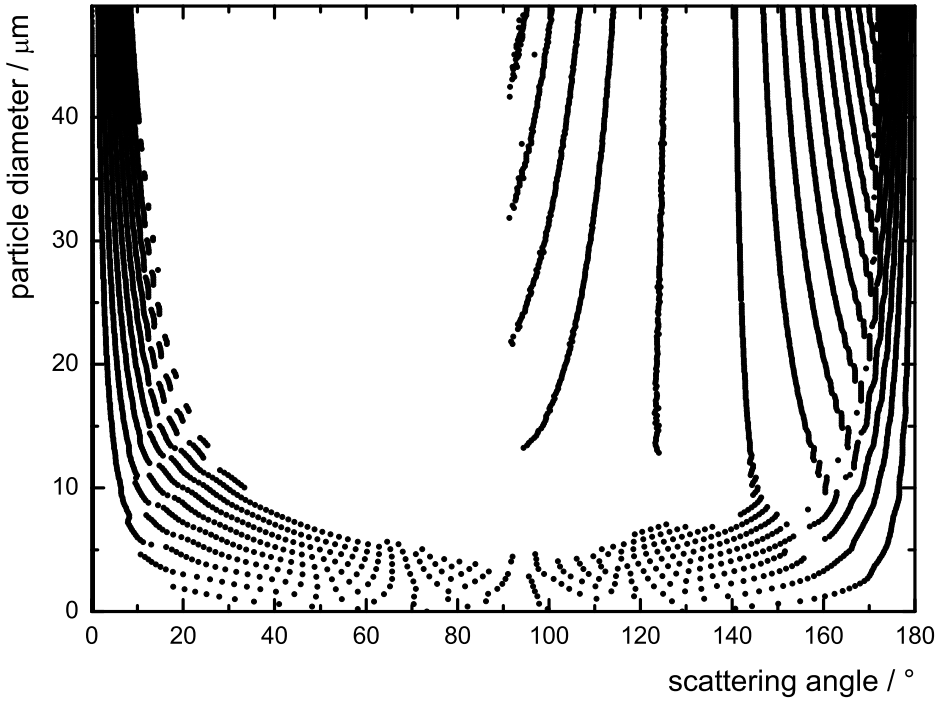

Figure 3.12: Angular distribution of local maxima of the scattering function for a range of diameters ($t_p = 50$ fs, $\lambda = 780$ nm, $n = 1.333$, perpendicular polarization).

a spectral width of $\Delta\lambda = 18$ nm at half maximum (consistent with $t_p = 50$ fs) a rectangular wavelength distribution instead of the Gaussian spectrum of a laser pulse was assumed. Fig 3.11 depicts the resulting angular intensity distribution in the rainbow region for a central wavelength of $\lambda = 780$ nm and a particle diameter of $d_p = 100$ μm. As expected, the ripple structure is smoothed and the angular position of the second-order refraction resembles a computation for femtosecond laser pulses with according pulse length in detail. Therefore the angular intensity distributions caused by sources of illumination besides ultrashort laser pulses, as e.g. described in Peil et al. (2006b), can be modeled physically more accurate if the according spectral intensity distribution is well known.

While the angular intensity distributions in figs. 3.9 and 3.10 represent particles of a fixed diameter and therefore details of the broader scattering function, fig 3.12 shows the angular distribution of local maxima of the scattering function for a spherical water droplet illuminated with $t_p = 50$ fs laser pulses and for diameters up to $d_p = 50$ μm ($n = 1.333$). For CW illumination the diagram would display a great number of additional maxima due to interference between different scattering orders and also due to morphology dependent resonances. With femtosecond laser

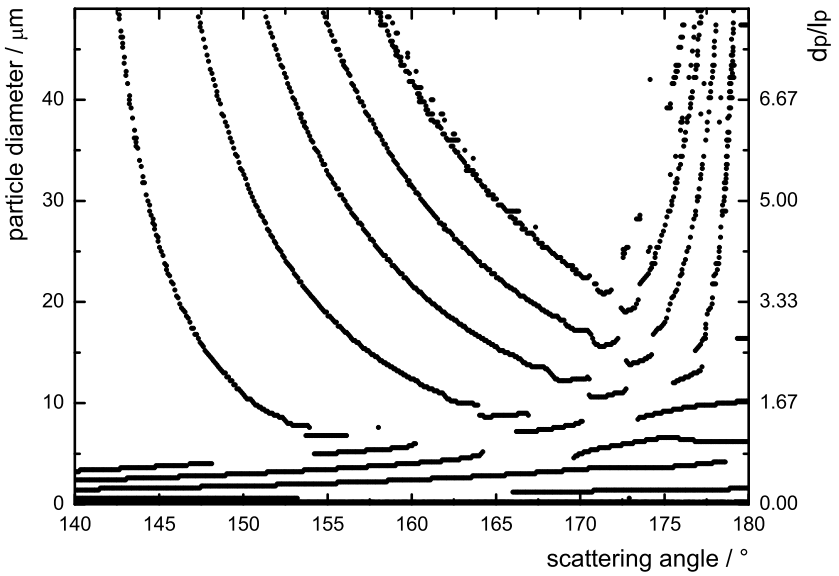

Figure 3.13: Rainbow section of the angular distribution of local maxima of the scattering function under ultrashort laser pulse illumination (t_p = 20 fs, λ = 780 nm, n = 1.333, perpendicular polarization).

pulses, the scattering function however is smoothed, even for droplet diameters down to approximately $d_p = 5$ μm at certain scattering angles (Bakic et al. 2009). The positions of the primary and secondary rainbow and the change in angular position of the supernumerary bows due to different diameters are clearly visible. The secondary rainbow decreased for diameters $d_p < 20$ μm while the primary rainbow maxima steadily altered their position with diameters down to $d_p = 15$ μm. For smaller droplets the progression of the maxima is still visible but less steady.

Figures 3.13 and 3.14 depict the region of the primary rainbow for illumination with laser pulses of $t_p = 20$ fs and $t_p = 10$ fs. The spatial equivalent to the temporal pulse length t_p is symbolized by l_p. Supernumerary bows of higher order disappear while the remaining rainbow maxima change their position with diameter steadily down to $d_p = 5$ μm. It is of extraordinary importance that the first and second supernumerary bows remain visible even at $t_p = 10$ fs. Their exact position can be utilized as the basis for in-situ refractive index measurement.

Ultrashort pulse lengths in the order of $t_p = 10$ fs correspond to an extremely wide spectral bandwidth. The spectral bandwidths (full width at half maximum) of the utilized pulse lengths were $\Delta\lambda$ = 90 nm, 45 nm and 18 nm for t_p = 10 fs, 20 fs and 50 fs, respectively. As discussed in chapter 2.4, the wavelength dependence of the

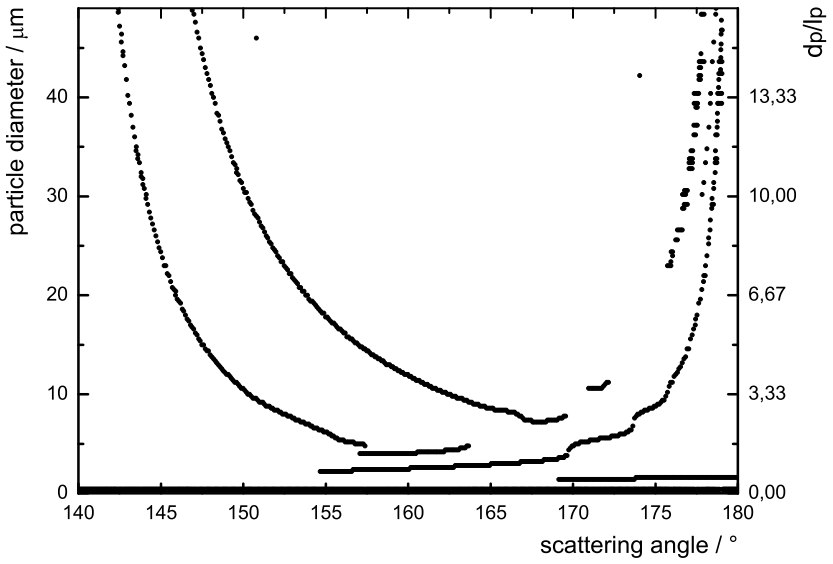

Figure 3.14: Rainbow section of the angular distribution of local maxima of the scattering function under ultrashort laser pulse illumination (t_p = 10 fs, λ = 780 nm, n = 1.333, perpendicular polarization).

refractive index of water for wavelengths from λ = 200 nm to 1100 nm (Quan and Fry 1995, Huibers 1997) is given by equation 2.28. Propagation of a pulse through a transparent but dispersive medium therefore results, among others, in a duration broadening of the pulse and a frequency chirp. These effects scale with the traveled distance in the medium and are to be considered and corrected for experimental setups including lenses. For small particle characterization, the necessary pulse length declines together with the distance traveled within the medium. For a d = 5 μm particle the traveled distance is only a few times the wavelength and is therefore neglectable for the qualitative results. The separation of reflection and second-order refraction, and therefore the smoothing of the ripple structure, is not affected because the reflection scattering order does not penetrate the particle.

The absolute angular position of the rainbow maxima is a function of the refractive index, which in turn can be used to quantify the droplet temperature. For a spherical droplet with d_p = 15 μm and illuminated with t_p = 50 fs laser pulses ($d_p/l_p = 1$), fig. 3.15 displays the angular positions of the first and second primary rainbow maxima for a range of refractive indices. The dependence of the first maxima angular position on the refractive index is linear. Because of the assumed parameters there was no interference between different scattering orders. They arrive at the detector at different times. These maxima positions are determined solely by the second-order refraction, which contains information on both particle

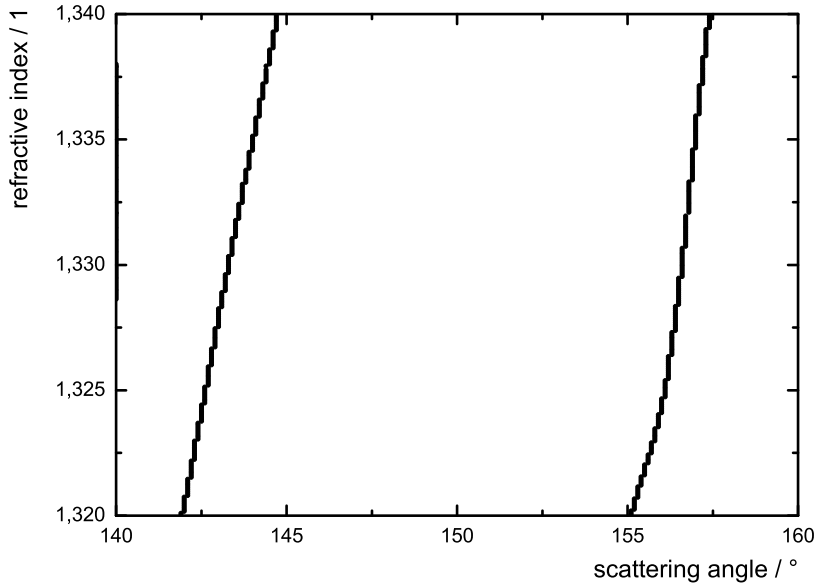

Figure 3.15: Angular progression of the primary rainbow first- and second-order local maxima for a range of refractive indices under ultrashort laser pulse illumination ($d_p = 15\mu$m, $t_p = 50$ fs, $d_p/l_p = 1$, $\lambda = 780$ nm, perpendicular polarization).

size and refractive index; hence they can be used for calibration. The position of the second maxima shown in this diagram is not exactly linear with refractive index, since additional scattering orders begin to overlap with second-order refraction. This is different for $t_p = 20$ fs and shorter laser pulses due to the missing overlap of scattering orders, as can be seen from fig. 3.13 and 3.14. Due to the shorter pulse length the second primary rainbow maximum follows the same linear progression with refractive index. According to Figure 3.13 the first rainbow maximum changes its angular position with diameter steadily down to $d_p = 5$ μm ($d_p/l_p = 0.83$). Thus the first rainbow maximum progresses linearly with refractive index for a droplet with $d_p = 5$ μm if illuminated with $t_p = 10$ fs. The deviation from linearity for this slope is smaller than $\Delta\Theta = 0.01°$, which corresponds to a change in temperature of up to 1 K (Thormählen et al. 1985).

The implementation of Rainbow refractometry failed for larger particles due to the sensitivity of the rainbow position to non-sphericity. However, small particles ($d_p < 30$ μm) are highly spherical because of the strong influence of surface tension. Extended GLMT was used to estimate the deviation in the angular position of the

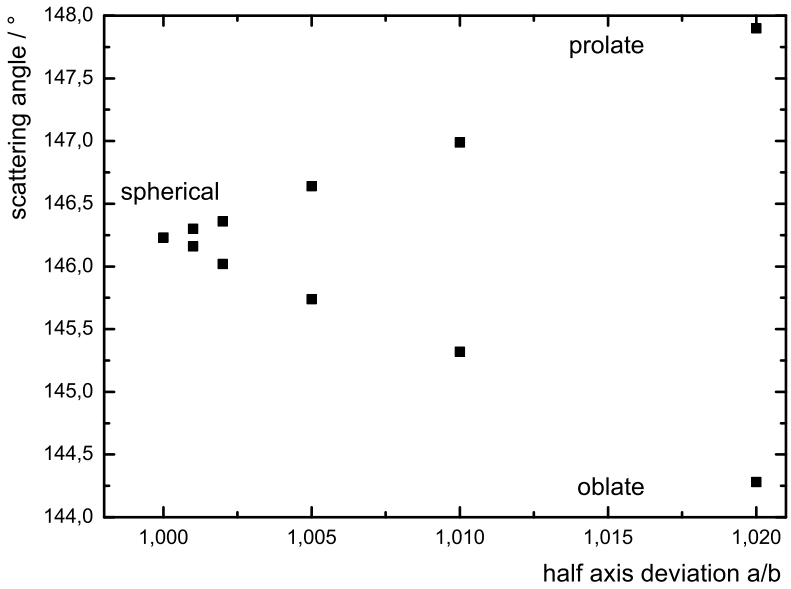

Figure 3.16: Angular deviation of the first maximum of the primary rainbow for a non-spherical droplet under ultrashort laser pulse illumination, calculated with extended GLMT (d_p = 8 μm, t_p = 10 fs, n = 1.33, λ = 800 nm, perpendicular polarization).

first rainbow maximum for small prolate and oblate droplets with $d_p = 8$ μm under pulsed illumination (t_p = 10 fs) (Xu et al. 2007). On the basis of the pioneering work of Gouesbet et al. on GLMT describing the interaction between a Gaussian beam and a sphere (Gousbet et al. 1988), Xu et al. extended the theory to the case of a spheroid illuminated by arbitrary laser beams (Xu, Ren et al. 2007). To study the case of a laser pulse with plane waves scattered by a spheroid, the waist radius of a Gaussian beam was set to be infinitely large. After transforming the pulses from the time domain into the frequency domain, the scattering amplitudes were calculated for each frequency. Using an inverse transformation of these amplitudes back to the time domain and making a summation brought out the time integrated scattering pattern for a spheroid. The whole scheme of calculation is comparable to that for a sphere (Mees et al. 2001a). Figure 3.16 depicts the angular deviation of the first maximum of the primary rainbow for prolate and oblate deformations of a small sphere. Half-axis deviations of only $\pm\ a/b = 1{+}10^{-2}$ already displaced the maximum by $\Delta\Theta = 1°$ for oblate and $\Delta\Theta = 0.75°$ for prolate deformation. Half-axis deviations of $\pm\ a/b = 1{+}10^{-3}$ are necessary for an angular deviation of

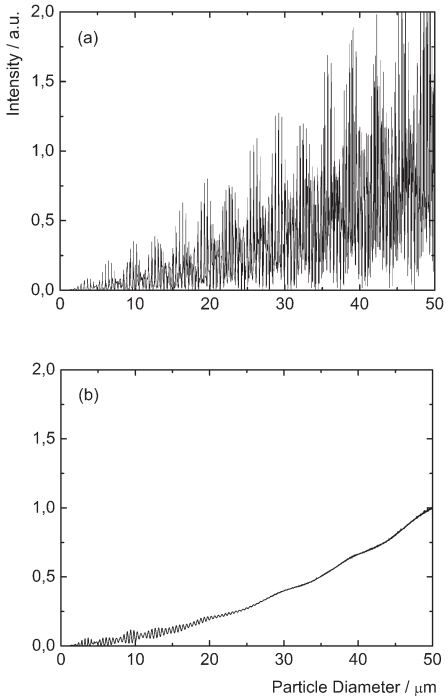

Figure 3.17: Numerically obtained intensity distribution in the far field for a range of diameters of a spherical, homogeneous droplet (n=1.333, $\Theta = 70°$). (a) CW illumination with $\lambda = 780$ nm and (b) pulsed illumination with $t_p = 200$ fs, $\lambda = 780$ nm.

less then $\Delta\Theta = 0.1°$ for both oblate and prolate spheroids which corresponds to a deviation in temperature of up to 10 K. To attain the proposed angular deviation of $\Delta\Theta = 0.01°$, which matches a deviation in temperature of only 1 K, a necessary half-axis deviation as low as $\pm\ a/b = 1{+}10^{-4}$ must be assumed (Bakic et al. 2009).

3.6 Intensity-Diameter Function and Morphology Dependent Resonances

Fig. 3.17 depicts numerically determined scattering intensities for different particle diameters under a favorable scattering angle and a) CW and b) pulsed illumination. The separation of individual scattering orders by femtosecond laser pulses is followed by a smoothing of the scattering function concerning the droplet diameter. This result is in regard to the smoothing of the rainbow not self-evident, because not only scattering lobes evoke oscillations. While interference between

the scattering orders explains the lower frequency oscillations in intensity regarding to particle size, morphology dependent resonances (MDR) emerge at exactly defined size parameters $x_s = 2\pi\ r_p\ /\ \lambda$ (also know as Mie parameter) and are distinguishable from interference between scattering orders by the width at half maximum which is at the scale of nanometers.

As outlined in detail by Roll (1999) and for optical microcavities in general in Vahala (2004), particles can function as optical resonators. While a simple laser cavity is built from two coplanar dielectric mirrors, amongst others, spherical transparent particles can align electromagnetic waves to circulate within them by following polygonal internal reflections. The case of constructive interference is called resonance, in which the internal field is boosted sharply. Obviously parameters like particle size, wavelength and refractive index have to meet the conditions of overlapping electromagnetic waves precisely, as is also know from acoustic whispering gallery modes (Rayleigh 1910). The width at half maximum for the size parameter of the resonance modes within such a spherical cavity depends on the lossless circulation of electromagnetic waves. Narrow resonance modes indicate a high capacity for storing energy. Numerically the electromagnetic field can be inflated by staggering 20 orders of magnitude. Physical particles are imperfect, but especially small droplets ($d_p < 30\ \mu$m) are highly spherical due to surface tension. Therefore experimentally observed optical resonances can still exceed the original field amplitude by many orders of magnitude.

While Lorenz-Mie theory provides precise results for computing the appearance of MDRs, Kahre and Nussenzweig (1977) have proposed a more comprehensible model on the basis of geometrical optics. In this model it is assumed, that a light ray contacts a dielectric sphere by grazing incidence. Due to the limit of total reflection such a ray is refracted into the sphere and follows polygonal internal reflections. Between two reflections an angle of $\alpha = 2\ \arccos(1/n)$ is passed. To close the loop, the path of the light-ray has to fulfill the condition:

$$\frac{1}{n} = cos\left(\frac{M\pi}{m}\right) \tag{3.21}$$

M represents the number of revolutions around the center of the sphere and m the number of reflections. For resonances to occur, the circumference C of the m-sided path needs to be an integral multiple l of the wavelength:

$$C_{cir} = 2\ r_p\ m\ cos\left(\frac{M\pi}{m}\right) = l\frac{\lambda}{n} \tag{3.22}$$

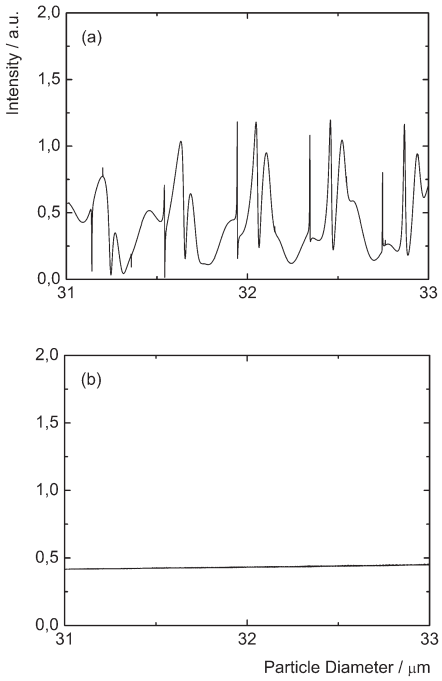

Figure 3.18: Numerically obtained intensity distribution in the far field for a range of diameters of a spherical, homogeneous droplet ($n = 1.333$, $\Theta = 70°$). (a) for CW illumination ($\lambda = 780$ nm) the contribution of MDRs becomes apparent on a nanometer scale. (b) For pulsed illumination ($t_p = 200$ fs, $\lambda = 780$ nm) the intensity distribution is free of MDRs and scattering lobes.

For the Mie-parameter this leads to resonances under the condition:

$$x_s = \frac{l\ \pi}{n\ m\ cos\left(\frac{M\pi}{m}\right)} \tag{3.23}$$

Unfortunately this model has its limitations, e.g. the physically wrong assumption of discrete refractive indices. A more sophisticated geometrical optics approach aligning with the precise Lorenz-Mie solution is given in Roll (1999).

In fig. 3.18 the contribution of MDRs is clearly recognizable for CW illumination due to the narrow width of the according peaks. The figure highlights details of the distributions depicted in fig 3.17. For illumination with femtosecond laser pulses, clearly not only the oscillations due to interference between scattering orders are

smoothed, also the MDR-modes are eliminated. Femtosecond laser pulses smooth the MDRs because the intensity of the illumination is spectrally broadened. The conditions necessary for MDRs to occur include a precise knowledge of the involved wavelength. For femtosecond laser pulses a spread of wavelengths is involved and therefore the intensity does not build up in resonance. Moreover, the principle of reciprocity (Favre et al. 2002, Hill et al. 2000) prevents the formation of MDRs if small droplets are illuminated by femtosecond laser pulses.

Chapter 4

Generation and Preparation of Small Particles

The inversion strategies discussed in chapter 3.1 - 3.3 are valid for spherical, homogeneous particles. Therefore a favorable experimental implementation with many industrial applications is to create and position small liquid droplets. In the following the corresponding devices and methods utilized in this work are discussed. Commonly, methods with moving and fixed droplet positions have to be considered separately. While single droplets with fixed positions are more suited for verification of numerical results and evaporation studies, moving droplet systems represent the majority of applications. Monodisperse droplet streams, atomization and acoustic levitation are outlined in Frohn and Roth (2000). A Paul trap with novel geometry of optical access and crucial to the experimental results in the study at hand is discussed (Heinisch 2006, Bakic 2008).

4.1 Monodisperse Particle Streams and Atomization

As depicted in fig 4.1, a stream of droplets can be produced by a piezoelectric droplet generator, based on the Rayleigh-breakup of a cylindrical liquid jet, which is created by passing the liquid through a circular orifice (Brenn et al. 1996). The droplet stream is called monodisperse when droplets of the same size and shape leave the orifice one by one in a uniform direction with constant spacing. When the liquid jet is perturbed regularly with the frequency f_{dis}, periodic disturbances with the wavelength λ_{dis} can be observed along the jet. These instabilities trigger the process of disintegration of the liquid jet. The disintegration leads to the formation of a chain of droplets. The velocity v of these droplets is assumed to be approximately the same as the velocity of the jet v_{jet}. Similarly the droplet

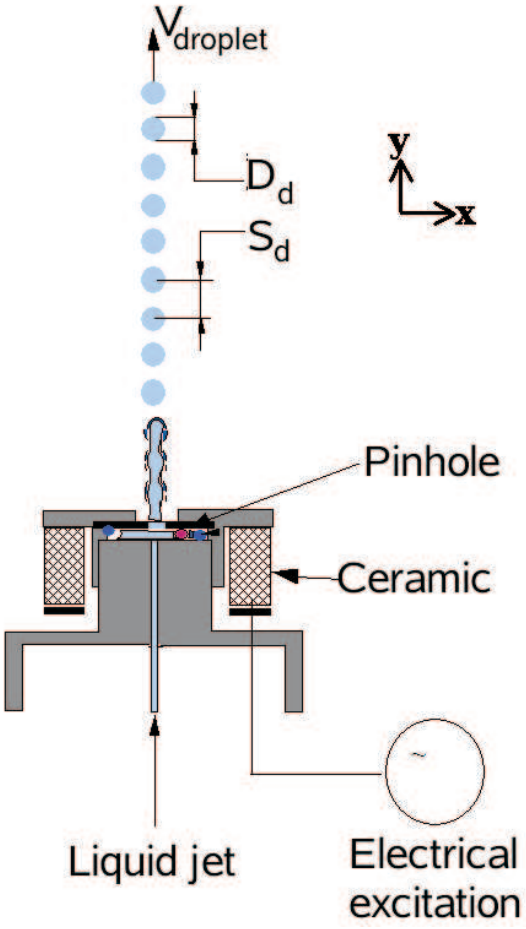

Figure 4.1: Monodisperse stream of spherical droplets with droplet diameter D_d and spacing S_d generated by an orifice with piezoelectric vibration.

temperature is determined by the temperature in the injector holding the liquid just in front of the orifice plate. Then a monodisperse droplet stream is obtained with distance $s = \lambda_{dis}$ between neighboring droplets. If it is assumed that the radius r_{jet} is determined by the diameter d_{ori} of the orifice with $r_{jet} = d_{ori}$ / 2, the droplet diameter is given by $d_p = 2{*}1.89 r_{jet}$; hence approximately twice the diameter of the orifice. A more accurate estimation of droplet size considers the flow rate at the orifice and the frequency ν of the piezoelectric oscillation. The flow rate Φ_f is given by mass transport per time:

$$d_p = \sqrt[3]{\frac{6\ \Phi_f}{\pi\ \nu}} \tag{4.1}$$

By variation of the frequency ν for a specific orifice and constant liquid pressure the droplet diameter can be varied around the previously assumed value:

$$1,68 * d_{ori} < d_p < 2,19 * d_{ori} \tag{4.2}$$

The liquid jet is stable only for a narrow band of disturbance wavelengths λ_{dis}, therefore the range of droplet diameter is limited for a given orifice diameter and flow rate. Outside of this wavelength range for the Rayleigh instability (Rayleigh 1879) the jet breakup can be much more irregular, leading to different droplet sizes and spacing.

In contrast to monodisperse droplet streams sprays are particle ensembles, which are composed of a high quantity of liquid droplets in a carrier medium like air or a composition of air and the vapor released by the droplets. To a first approximation the spray may be considered as an ensemble of polydisperse solid particles. The trajectories of the individual particles can therefore be quantified by the formalism of classical mechanics. Even with the recent generation of computers such a computation is only feasible for multiple droplets representing a subsystem of the actual spray. However, if the particle ensemble is characterized in terms of a distribution function containing statistical information on the intrinsic properties of the droplets like size, velocity, refractive index and so on, it becomes quantifiable. Because a spray evolves in time, a corresponding distribution function will as well consider time as a parameter. The distribution function also has to consider the consequences caused by, e.g., evaporation, droplet-to-droplet or droplet-to-wall interaction and convective transport. In regard to the kinetic theory of gases distribution functions following Boltzmann are in use for describing the progression of the distribution function of sprays (Frohn and Roth 2000). In the case of a monodisperse droplet stream the distribution function turns into a near delta function, because the size range of the droplets becomes very small.

Sprays can be implemented with a variety of methods. In a pressure atomizer the liquid leaves a small aperture or nozzle as a thin jet which disintegrates into a spray. During this process the energy previously available as mechanical pressure is converted into kinetic energy and is also stored as surface energy associated with the emerging droplets. In literature, many different types and designs of pressure atomizers are described (e.g. Lefebvre 1986). Rotary atomizers apply a disk or wheel rotating at high speed. The liquid moves from the center to the circumference of the rotating device, where it runs off in form of a thin sheet, which again disintegrates through the influence of aerodynamic forces of the surrounding air

or a supplemental injector creating additional air flow. For the study at hand an ultrasonic atomizer has been used. A thin liquid film is deployed on a small solid surface vibrating with high frequency. Due to the oscillations the liquid shows a pattern of microscopic standing waves. For large oscillation amplitudes the wave peaks disintegrate and a mist of tiny droplets is observed above the surface of the liquid. The ultrasonic atomizer can deliver very fine sprays in the size range necessary for small particle characterization ($d_p < 30\mu$m). The droplets in the produced spray have a very low velocity, which eases the conditions necessary for detection and imaging of scattered laser illumination.

4.2 Acoustic Levitation of Particles

To study a single, fixed droplet it can be levitated in an acoustic field generated between an oscillating surface and a reflector. The minimal supported droplet size of such a system is commonly larger than $d_p = 100$ μm. It is possible to levitate droplets with diameters up to a few millimeters. Droplets of this scale however do not remain spherical. The distance between the vibrating plate and reflector has to be set up very precisely for a given frequency to obtain a standing wave. Also, this distance, which is a multiple of $\lambda/2$, should be large enough to allow suitable optical access to a levitated droplet and the scattered light. The vibrating plate produces an acoustic wave which is then reflected and interferes with the primary wave. This leads to a standing wave with, usually only a few, nodes and antinodes of air pressure. A particle interacting with such a sound wave is influenced by hydrodynamic forces. The value of these forces is equal to the average flux of momentum through an arbitrary closed surface around the particle:

$$F_i = \oint \Pi_{ik} dA_k, \quad \Pi_{ik} = p\delta_{ik} + \sigma_{gas} v_i v_k \tag{4.3}$$

p stands for the static pressure and v_i, v_k are the components of the gas velocity. δ_{ik} is the Kronecker symbol. With such a device, regulated levitation of not only a liquid droplet but also a solid body is possible. The force exerted by acoustic pressure nodes on a sample within a standing wave has been discussed in Leung et al. (1981) and Gor´kov (1962). King (1934) has deduced the relation describing the mechanical equilibrium between the forces of acoustic radiation and gravitation acting on a small solid sphere:

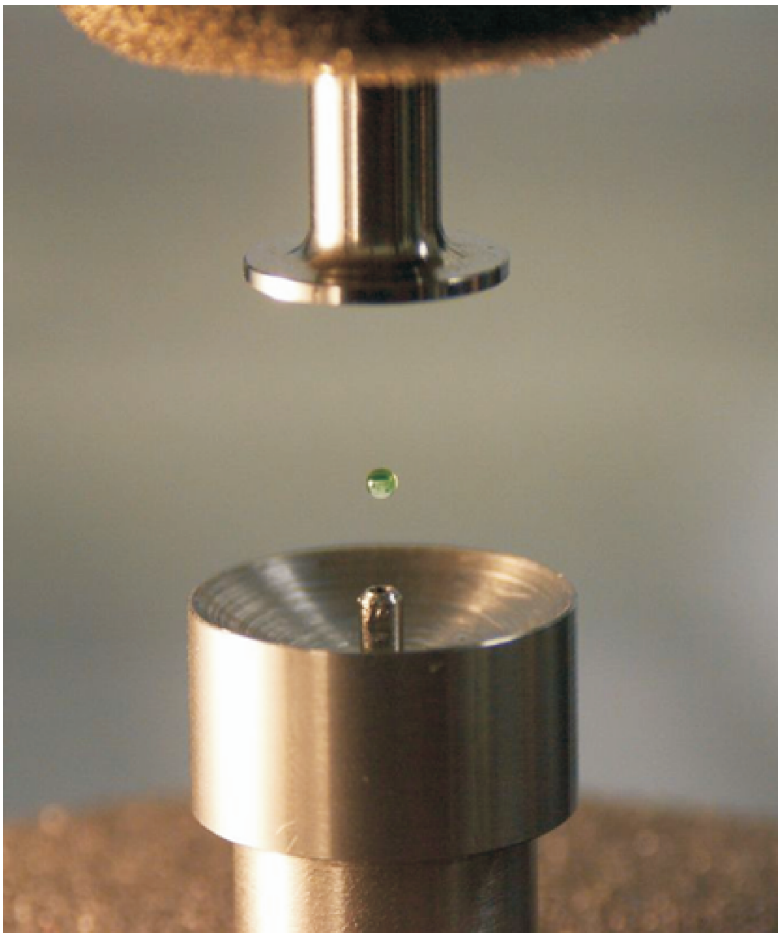

Figure 4.2: Vibrating plate (above) and reflector (below) of the utilized acoustic levitator. Adapted from Al Zaitone (2009).

$$F = \frac{5}{6}\frac{p_1^2}{\delta_{gas} c_s^2} k sin(2kz) \geq \frac{4}{3}\delta_d g \tag{4.4}$$

δ_{gas} stands for the density of the surrounding atmosphere and δ_d is the density of the levitated object. C_s is the sound velocity and k the wavenumber. Common devices create the frequency necessary for a standing wave and therefore levitation by means of a piezoelectric transducer considering the rotational symmetry of the droplet. As in the utilized levitator (fig 4.2), a typical value for the distance between the plates containing the standing wave is $x = 2$ cm. The ultrasonic frequency in the setup at hand was $\nu = 38$ kHz. The droplet diameter has to fulfill

the condition $d_p < \lambda/2$. This is necessary to keep a physically reasonable distance between the nodes within the standing wave.

Many techniques can be used to place a liquid droplet between the vibrating plate and the reflector. One possibility to achieve this, is to adjust the orifice of an ultrasonic droplet generator in direction of the plates. Some of the droplets of the very thin spray get caught within the standing wave. Multiple droplets caught in a single pressure node combine to a larger single droplet. Alternatively, a single droplet is suspended on a thin fiber or needle and positioned manually. With a droplet on demand generator small droplets can be injected into the levitator. An already levitating droplet can be enlarged by simple addition of another droplet.

4.3 Electrodynamic Levitation of Particles

A Paul trap levitates particles in the diameter range of $d_p = 10$ μm to 300 μm and is therefore well suited for the characterization of fixed small particles with $d_p < 30$ μm. Compared to an optical trap it is not constricted to transparent matter. So far a disadvantage of a Paul trap was the limited optical access to the levitated particle, due to the geometry of the involved electrodes. Therefore a novel geometry for Paul traps was proposed in Heinisch et al. (2006) which skillfully provides a 360° horizontal view at the target. Additionally it has built in drains for gas flow and the injection of droplets. An ideal electrical potential inside an axial-symmetric Paul trap is given, in cylindrical coordinates r, ϕ and z, by:

$$\Phi(r, \phi, z, t) = \frac{\Phi_0}{z_0^2} sin(\omega t)(z^2 - \frac{r^2}{2}) \tag{4.5}$$

(Wuerker 1959). t is the time coordinate and ω the angular frequency of the oscillating potential. Φ_0 is the potential at position z_0 on the z-axis. The potential is parabolic in every spatial direction. At the center it has in axial direction a maximum and a minimum in radial direction and vice versa as the oscillation progresses. Therefore at the center of the trap the potential exerts no force on a charged particle. The motions along the radial and axial direction are independent of each other, hence it is not necessary to consider both in order to understand the

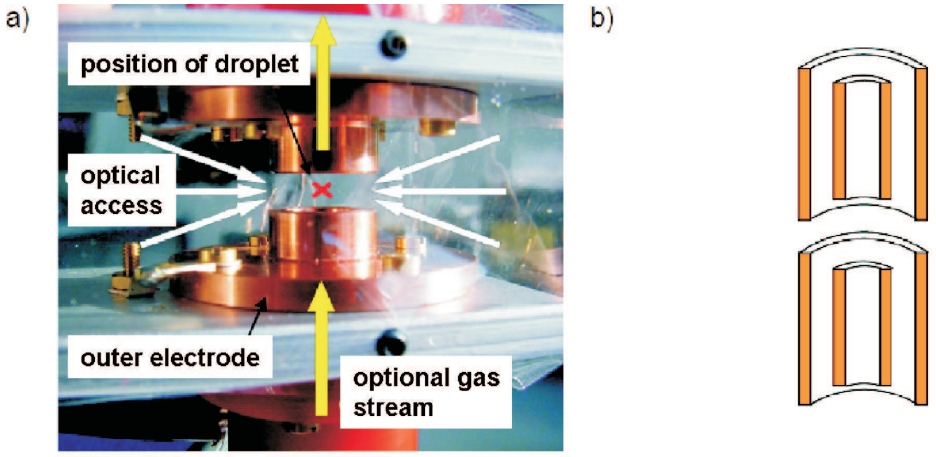

Figure 4.3: (a) Photograph of the utilized Paul trap. (b) schematic depiction of the electrode alignment cut in half. Adapted from Christian Heinisch: "Optische Messtechnik für umströmte Tropfen in einer neuen elektrodynamischen Falle", 2008, PhD-Thesis, TU Darmstadt.

functional principle of the trap. Outside the center of the trap, at an arbitrary position where the particle can be displaced, a force periodically changing its polarity takes effect. Its amplitude increases with distance from the center. If averaged over a period, the force exerts no pull on an ideal charge. However, the droplet is movable and carries out oscillations. For appropriately chosen parameters and a half period of this movement an acceleration towards the center of the trap takes place. But closer to the center the amplitude of the electrical force decreases. During the subsequent half period the droplet is therefore closer to the center. The charged particle is pushed successively towards the center, no matter the polarity of its charge. This force can be described as the gradient of a function, a so-called pseudo-potential, which is proportional to the squared electrical field. An exact analytical description of the motion in vacuum is given by Mathieus´ differential equations. The influence of air friction is normally beneficial for stability. For a permanent external force like weight or air friction in a gas stream induced by a drain the particle carries out oscillations outside the center of the trap. To make the particle keep its position anyway, these external forces are compensated by an additional constant electric field.

According to the previous considerations about the electrodynamic potential inside a Paul trap, such a device, as seen in fig. 4.3, was assembled and integrated into the experimental setup depicted in fig 4.4. In this way, as outlined in Heinisch et al. (2006), the diameter of an evaporating water droplet in ambient air and

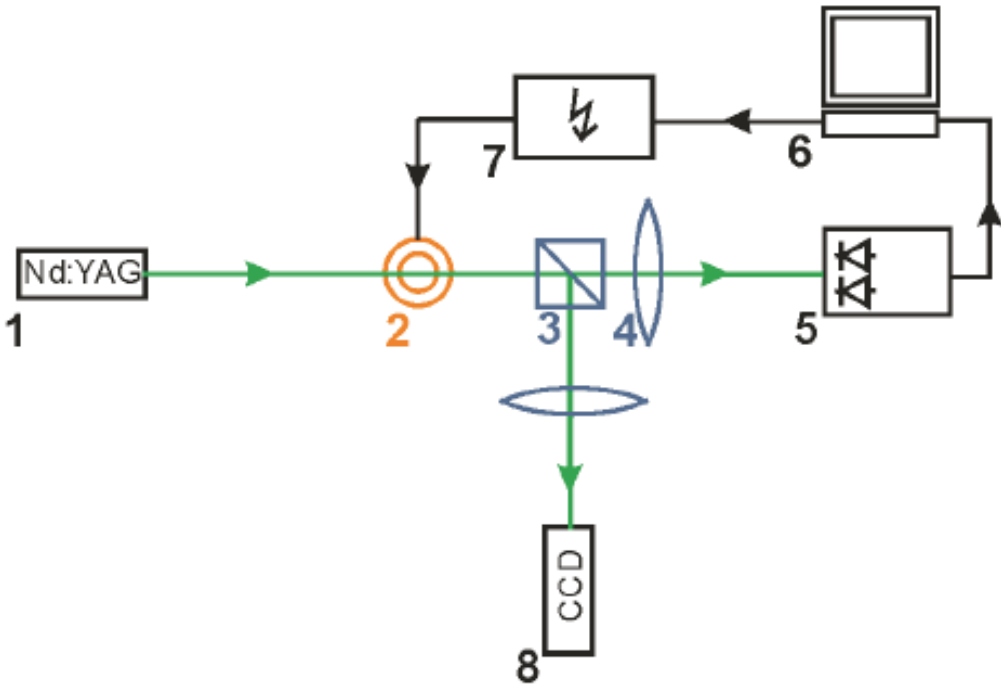

Figure 4.4: Experimental setup for measurement of refraction of an evapourating droplet. (1) Nd:YAG laser, (2) Paul trap, (3) beam splitter, (4) lense, (5) segmented photodiode, (6) PC with DA/AD transformation, (7) high voltage amplification, (8) CCD-camera. Adapted from Heinisch et al. (2006).

in an air stream was successfully measured. With it the operability of the trap and the possibility of application in laser diagnostics was demonstrated. In the experiment an inkjet cartridge HP 51604A was used to inject a water droplet into the Paul trap. The electric charging of the droplet at the exit of the cartridge is achieved by the influence of a ring-electrode with a $U = 1$kV potential positioned in a distance of $d = 1$ mm. The droplet was illuminated with a CW laser beam of a Nd:YAG-Laser at $\lambda = 532$ nm with an output power of $P = 5$ mW. The beam waist was $z = 2$ mm at the center of the Paul trap. The angular intensity distribution of the droplet was recorded by a CCD-camera with 25 frames per second. The camera was positioned in the focal point of a lense with a focal length of $f = 80$ mm. The angular intensity distribution was analyzed by digital image processing. Moreover a servo loop including a segmented photo diode was added. A lens (4) imaged the droplet on this diode. With this the changing weight of the droplet was compensated, keeping it in the center of the trap. The signal of the diode was evaluated by a computer (6), which controls the vertical position of the droplet by using an amplifier (7). For it a DC voltage is superimposed to the AC

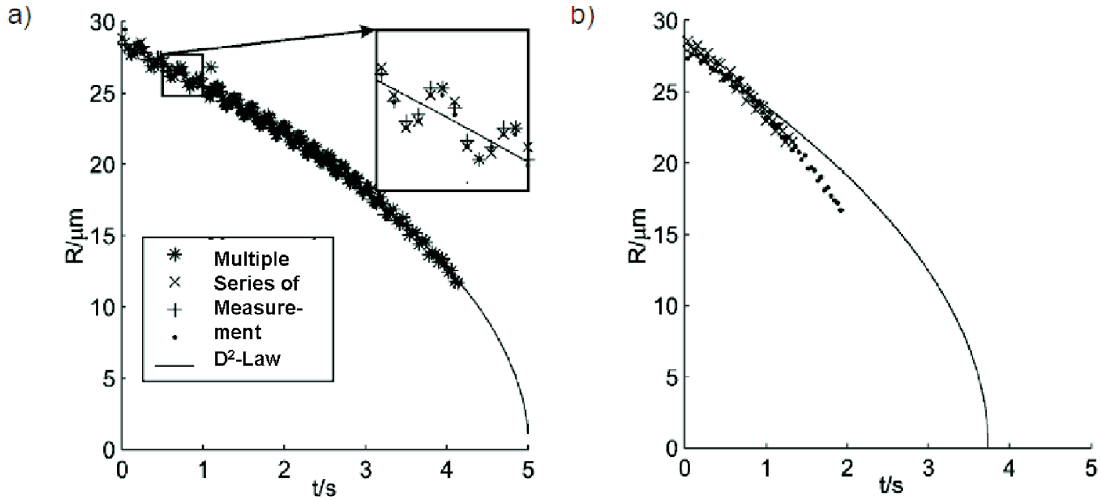

Figure 4.5: Diameter of an evaporating water droplet in resting ambient air and in an air stream suspended by the disussed Paul trap with novel geometry of optical access. Adapted from Heinisch et al. (2006).

voltage on the upper inside electrode (2). The AC voltage, applied at the inner electrodes opposite to the grounded outer electrodes, was also computer generated and amplified. Additionally the AC voltage had to be reduced from its peak value of $U = 400$ V at $\nu = 50$ Hz while the droplet evaporated, due to the ratio of charge to weight of the droplet. During evaporation the charge of the droplet remains the same, but not its weight. Therefore a droplet cannot be stabilized continuously without this computer controlled adjustment.

The data in fig. 4.5 depicts the experimentally obtained droplet diameter as a function of time (Heinisch et al. 2006). Many droplets have been investigated, therefore data associated with different droplets was depicted with different symbols and shifted on the time axis to overlap with each other. The diameter of the droplets was obtained by analyzing the ring minima of first order refraction. Reflection and diffraction was neglected. In Fig 4.5 a) oscillations of the droplet diameter are recognizable. This effect depends only on the absolute diameter of the droplet, not on its initial size. It is a consequence of the neglected influence of reflection and diffraction of laser light by the droplet. In theory, a homogeneous, resting droplet evaporates by loosing surface area linearly with time (in case of nonexisting convection and steady temperature):

$$D^2(t) = \sqrt{D_0^2 - \beta t} \tag{4.6}$$

This is the so-called D^2 law (Wilms 2005). D=2*r stands for the droplet diameter. D_0 is the droplet diameter at time $t = 0$. β is the evaporation rate. The parameters β = 6,44 m^2/s and D_0 = 2*28,4 μm result in an analytical graph fitting the measured data closely. In the case of an evaporating droplet with ambient air stream (fig 4.5 b) the graph deviates from the prediction. As recognizable in the diagram, the evaporation is more rapid. Therefore the presented Paul trap can hold water droplets with a radius between r = 28 μm and 12 μm and makes an examination possible. Likewise it was proven that an ambient air stream can be induced to the center of the trap and be used to change the experimental circumstances (Heinisch et al. 2006).

Chapter 5

Strategies for Exploiting Short Coherence Length Laser Sources for Particle Characterization

To verify several numerical characteristics of the scattering function for short coherence length laser sources stated in chapter 3, time integrated detection of scattered illumination has been experimentally implemented in various combinations considering the properties of the detection device, the type of laser source, and, as discussed in chapter 4, the generation and preparation of droplets. While paragraphs 5.1 to 5.3 consider the detection of the angular intensity distribution of small particles, 5.4 and 5.5 focus on the diameter-intensity relationship.

With regard to the detection device, the influence of femtosecond laser pulses on the rainbow region of the angular intensity distribution originating from an illuminated droplet has been detected with the plain, spacious surface of a CCD-chip without imaging optics. Imaging optics numerically imply a Fourier-transform of the signal and therefore obscure, in this specific measurement, the desired far-field intensity distribution holding clear information on particle size and refractive index. To test alternative sources of illumination and prove the assumption of short coherence length causing the desired effect, the measurement aiming to remove the so-called ripple structure, but not the angular intensity oscillations of second order refraction in the rainbow region, was repeated with a small and cost effective semiconductor laser source utilizing optical feedback. The actual imaging of the angular intensity distribution on a CCD-chip with a set of lenses, for example inside a long distance microscope, leads to the detection of glare points, bright isolated spots on the droplet surface, representing the various scattering orders. The behavior of glare point intensities of different scattering orders has been studied experimentally for femtosecond laser pulse illumination.

Moreover, to investigate the influence of scattering angle independent morphology dependent resonances (MDRs) on the diameter-intensity relationship of a rapidly evaporating droplet a lens was used to, not image, but focus the scattered intensity on a fast photodiode serving as point detector. In addition, the diameter-intensity relationship was examined to facilitate the determination of the Sauter mean diameter of small droplets. For this the scattered intensity was, in place of a lens and a fast photodiode, imaged with an intensified camera including a long distance microscope.

It remains important to be aware of the three major, differing causes for interference structures contributing to the shape of the scattered intensity distribution of a droplet. While the temporal and spatial overlap of scattering orders emitted by an illuminated droplet leads to angular intensity oscillations, e.g. the second refractive scattering order (first rainbow) has more then one ray-path contributing to the overall scattering. Therefore angular intensity oscillations can also be caused by interference within the same scattering order. In addition, MDRs result in strong disruptions in the diameter-intensity distribution.

5.1 Rainbow Measurement Technique

In chapter 3.1 and 3.5 the numerics of the first rainbow have been discussed as a component of the overall scattering function for a spherical, homogeneous particle. In terms of geometrical optics, second-order refraction results in two light rays with slightly different path lengths for any given detection angle in the rainbow region. As depicted before (e.g. fig 3.9/10), the interference between the two different partial rays of the second-order refraction results in intensity maxima and minima in the angular intensity distribution. For an observer noticing the rainbow in the sky arising from light scattering from water droplets, commonly only the main intensity maxima will be visible, distributed over multiple colors given by the broad spectrum of the sun. However, in the laboratory, with a laser emitting only at a specific wavelength, the lesser maxima of the rainbow region are also revealed. The angular distances between the maxima contain information about the diameter of a spherical, homogeneous droplet. Furthermore, the absolute angular position of the maxima is a function of the refractive index, which can be used to quantify the droplet temperature. Unfortunately, far-field interference with the surface reflection and higher scattering orders creates the ripple structure which obscures the intensity distribution of second-order refraction. For small particles with a diameter less than $d_p = 20$ μm the ripple structure conceals the angular structure of the second-order refraction and prevents accurate particle characterization, except under the most well controlled laboratory conditions (Onofri et al 2004). As described in chapter 3, numerical simulations indicate an adequate

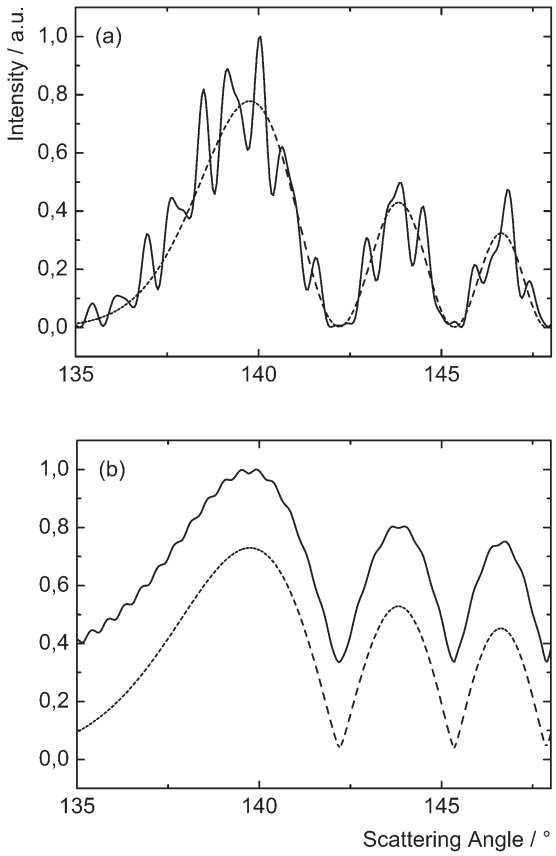

Figure 5.1: Numerically obtained angular intensity distribution in the rainbow region for (a) CW and (b) pulsed illumination (t_p = 200 fs, λ = 780 nm) with regard to a spherical droplet (d_p = 94 μm, n = 1,333). (a) The Mie sum (full line) follows from interference between surface reflection and second-order refraction, which obscures the underlying oscillations of the rainbow (dashed line). (b) The intensity of the surface reflection adds to the intensity of the rainbow, leaving the position of its local maxima.

suppression of the ripple structure if corresponding droplets are illuminated with femtosecond laser pulses. Also, it was shown that even the spectral width of pulses as short as t_p = 10 fs will not lead to a blurring of the angular positions of local intensity maxima for small particles. In comparison, the effect of dispersion is very pronounced for a natural rainbow in the sky due to the average diameter of raindrops, which is considerably larger than the small particles investigated in this work. The pulse length has to be chosen appropriately, because on the one hand, we want to make possible the interference between partial rays within the second-order refraction, and on the other hand suppress the interference with other

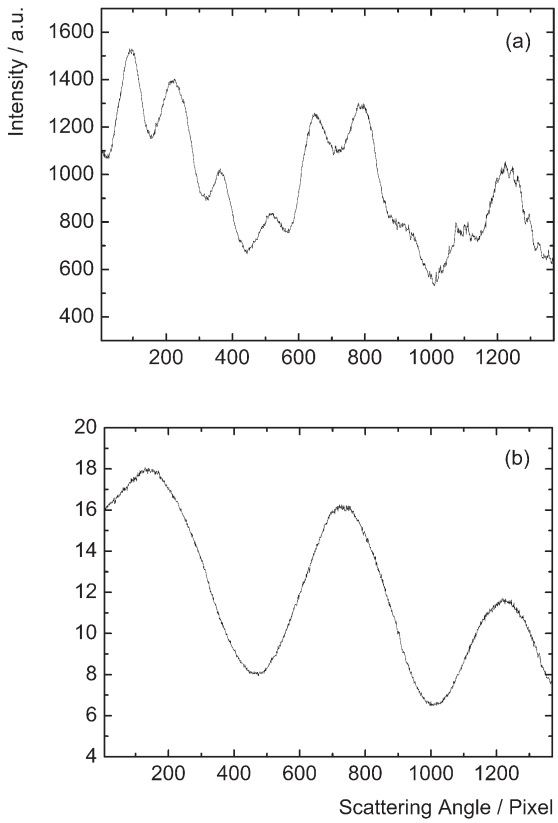

Figure 5.2: Experimentally obtained angular intensity distribution for (a) CW and (b) pulsed illumination (t_p = 200 fs, λ = 780 nm) with regard to a monodisperse stream of spherical droplets (d_p = 94 μm and n = 1,333).

scattering orders. Without coherence not only the ripple structure, but also the intensity modulation resulting from the two-ray-solution of second-order refraction would be eliminated, and therefore the information contained about particle size and refractive index.

The droplet stream was produced by a piezoelectric droplet generator, based on the breakup of a cylindrical liquid jet, which is created by passing the liquid through a circular orifice (Brenn et al. 1996). Experimental verification was realized by illuminating a jet of monodisperse water droplets with pulses and the CW output of a Ti:sapphire femtosecond laser (pulse length t_p = 200 fs, central wavelength λ = 780 nm, repetition frequency ν = 75 MHz). For the investigation of the effect of femtosecond laser pulses on the rainbow the quality of the jet was checked by recording the transmitted light of a triggered streaker lamp with a CCD-camera.

In the experimental setup the water flux and excitation frequency yielded a droplet diameter of $d = 94\ \mu$m. No significant difference arises compared to scattering from a single droplet because the angle dependent intensities of single droplets in the jet are identical and add up at the detector. The angle deviation produced by changing particle position within the spatially extended laser beam was negligible due to the wide beam waist. Detection was realized with a PCO SensiCam QE CCD-Camera, positioned at an angle of $\alpha = 150°$. Fig 5.1 depicts the numerically predicted angular intensity distributions in the rainbow region for the parameters utilized in the experimental setup. The predicted suppression of the ripple structure obscuring the angular intensity distribution of second-order refraction was confirmed (Bakic et al. 2008). Figure 5.2 shows the measured intensity distribution for illumination with CW and ultrashort pulses. A perfect agreement between the calculated scattering function in fig. 5.1 and the measurement in fig. 5.2 was not expected, because the actual ripple structure is extremely sensitive to any diameter change and, because of evaporation and flow fluctuations, the monodisperse droplet generator is clearly not able to produce droplets with a higher accuracy.

5.2 Semiconductor-Laser Source with Optical Feedback and Adaptable Coherence Length

To experimentally verify the notion that the smoothing of the ripple structure is an effect that is in reality based on short coherence length and not on some other property of femtosecond laser pulses, a novel, CW semiconductor laser source based on optical feedback was used to repeat the rainbow refractometry experiment as depicted in fig 5.3 (Peil et al. 2006b). With femtosecond laser pulses the desired effect is established due to the correlation of pulse length and coherence length. With the novel laser source CW illumination is preserved, but due to shortening of the coherence length, comparable to a femtosecond time scale, the results presented in 5.1 for illumination with femtosecond laser pulses have been expected to be met.

In contrast to the experimental setup used for fig. 5.2, an acoustic levitator was employed to make a droplet available instead of a monodisperse droplet stream. The utilized source of illumination (Peil et al. 2006a) was a commercially available $x = 1.6$ mm long ridge waveguide Fabry-Perot semiconductor laser (SL) emitting at a center wavelength of $\lambda = 785$ nm. As depicted in fig 5.3, the emitted illumination was collimated by a lens L, partially reflected by a mirror M, and fed back into the source after a round trip time τ in the external cavity with the phase difference $\Delta\Phi = \Phi(t)\text{-}\Phi(t\text{-}\tau)$. To generate broadband emission, a resonance condi-

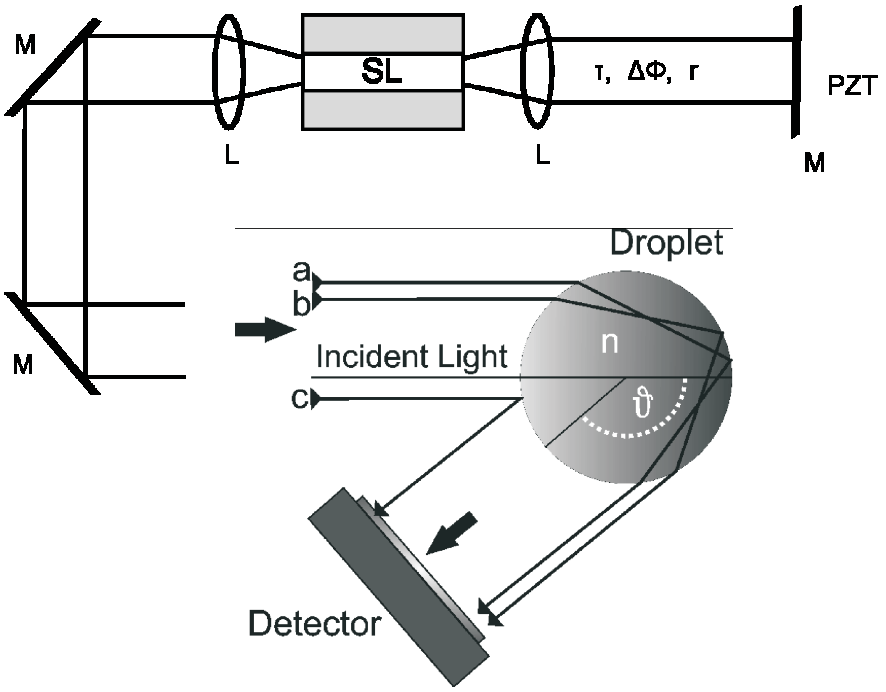

Figure 5.3: Schematic of the incoherent semiconductor laser source and the rainbow refractometry experiment. Adapted from Peil et al. (2006b).

tion between the fundamental frequency of the laser cavity and the external cavity has to be realized, both being of comparable order of magnitude. This enhances coupling between the longitudinal laser modes and allows for spectrally broadband emission (Peil 2006a). The ratio between the length of the external cavity (L_{EC} = 14.8 mm) and the optical length of the source cavity ($L_{SL,opt}$ = 5.92 mm) was set to 2.5 with high precision, a ratio for which good coupling of the laser modes can be achieved. The particular parameters which determine the emission properties of the source under these conditions are the delay time τ, the pump current I_{dc} of the source, the feedback ratio r, and the feedback phase $\Delta\Phi$ being a 2π-cyclic parameter. The feedback ratio r is defined as the quotient between the power of the feedback and the emitted light, $r = P_{fb} \,/\, P_{out}$. $\Delta\Phi$ was used as the control parameter, which can be changed by shifting the mirror on a sub-wavelength scale with a piezoelectric transducer. The other parameters were kept constant at r = 0.16, τ = 98.7 ps, and the pump parameter $p = I_{dc} \,/\, I_{th,sol}$ = 3.3, with $I_{th,sol}$ = 46 mA being the threshold current of the solitary semiconductor laser. In Peil et al. (2006a) it was shown that $\Delta\Phi$ is a very good control parameter which allows for stepwise adjustment of the emission properties. This makes possible two characteristic states of emission. Depending on $\Delta\Phi$, either stable emission on one laser mode was adjustable with the assigned phase value $\Delta\Phi_{stab}$, or spectrally broad-

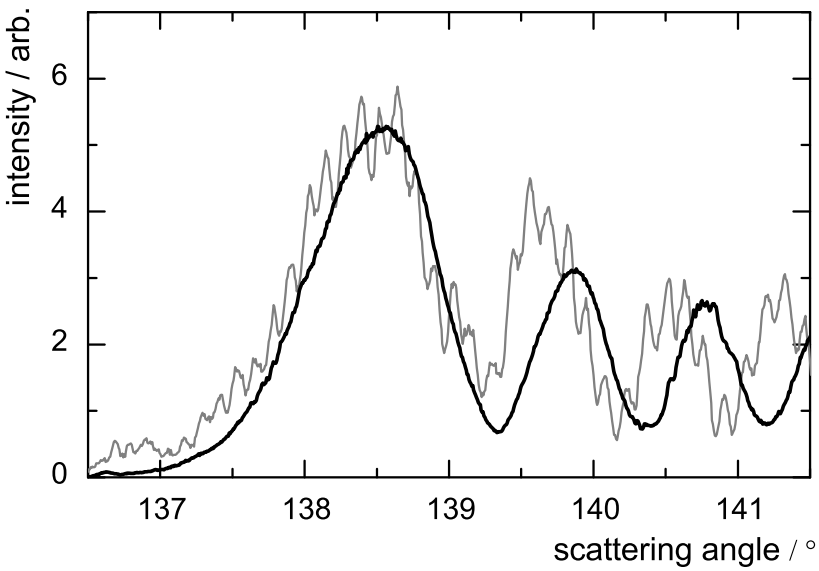

Figure 5.4: Experimentally obtained angular intensity distributions for rainbow refractometry with the novel SL source and a water droplet for coherent (grey lines) and incoherent (black lines) illumination.

band (BB) emission for slightly reduced $\Delta\Phi_{BB} = \Delta\Phi_{stab}$ - 0.4π rad. The emission spectrum for Δ_{stab} showed single mode emission with a side-mode suppression of more than $I = 30$ dB. The spectrum for $\Delta\Phi_{BB}$ resulted in emission with a spectral spectral range of about $\Delta n = 7$ nm. This is equivalent to the spectral width of a femtosecond pulse with $t_p = 200$ fs. For broadband emission the output power was $I = 110$ mW. A continuous rf spectrum with a bandwidth beyond $\nu = 4$ GHz was observable, representing the underlying chaotic dynamics. The low frequency portion of the rf spectrum was at the noise floor of the detection at I = -82 dBm. From this follows that the average power of the SL source for this state of emission had low relative intensity noise on the relevant time scales for technical applications. The broadband emission state was robust despite being dependent on dynamical instabilities. Therefore, the dynamically induced low coherence properties of the utilized light source can be considered as an excellent alternative for the costly and spacious generation of femtosecond laserpulses concerning rainbow refractometry.

To conduct the experiment (Peil et al. 2006b), a water droplet was illuminated

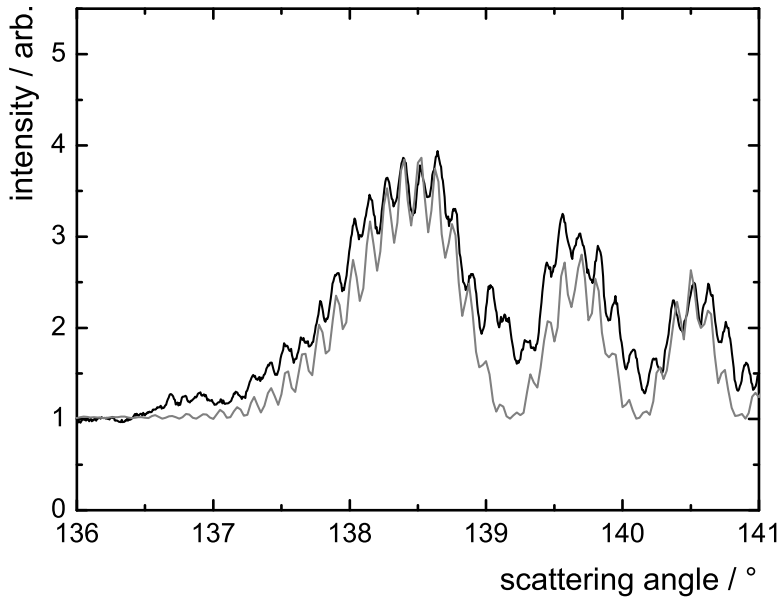

Figure 5.5: Comparison between experimentally (black lines) and numerically (grey lines) obtained angular intensity distributions for a water droplet under coherent illumination.

with collimated light from the semiconductor laser source. The droplet was held between the vibrating plate and reflector of an acoustic tec5 AG ultrasonic levitator, which can properly suspend spherically shaped droplets with diameters between $d_p = 400$ μm and 1 mm. The droplet was illuminated with coherent light with $L_{coh} = 7.8$ m and the angular intensity distribution of the scattered light was detected and recorded by a 12 bit SENSICAM QE CCD-camera with a shutter time of $t_s = 1$ ms. Afterwards, the measurement was repeated for incoherent illumination with $L_{coh} = 120$ μm. The experimental results are depicted in fig. 5.4. The grey data corresponds to coherent illumination and the measurement depicted in black to incoherent illumination.

As expected, for coherent illumination the unwanted ripple structure on top of the supernumerary arcs from second order refraction was obtained, while a smooth intensity distribution without superimposed ripples revealing the undisturbed interference structure given by second order refraction was obtained for incoherent illumination. As discussed in chapter 5.1, the smoothed structure allows accurate determination of the position of the supernumerary arcs which can be used to estimate the diameter of the droplet. To determine the exact scattering angle, the

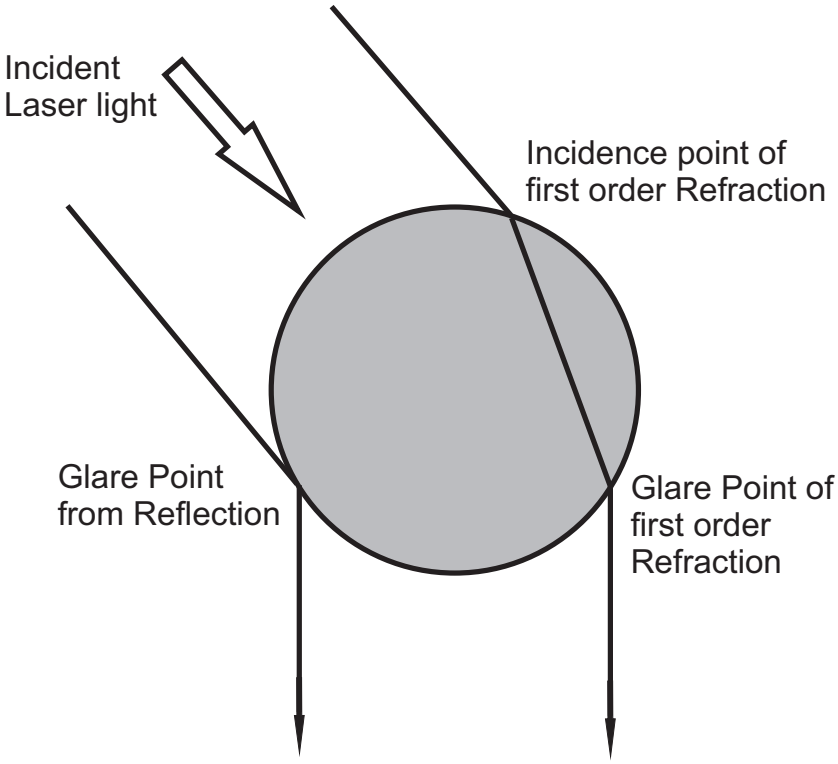

Figure 5.6: Glare points of highest intensity as explained by geometrical optics.

diameter of the droplet has been varied numerically with FLMT until excellent agreement has been achieved for incoherent illumination between the experiment and numerics. The droplet size was estimated to be $d_p = 515 \pm 5$ μm. For the calculations a refractive index of $n = 1.33$ and a central wavelength of $\lambda = 780$ nm have been assumed. Due to the size of the droplet beyond the diameter of small particles, numerical modeling was possible for proper estimation of the droplet size under coherent illumination as well. In fig 5.5 good agreement was achieved for a droplet size of $d_p = 600$ μm, but in sharp contrast to incoherent illumination with an uncertainty of $\Delta d_p = \pm 50$ μm. The difference in diameter between the case of coherent and incoherent illumination developed due to evaporation and therefore a contraction of the droplet.

Alternatively to laser pulse computation with FLMT, the case of short coherence length can be modeled more in accordance with the physical process of optical feedback. The feedback-source provided a CW spectral width of $\Delta\lambda = 7$ nm at half maximum, matching the width of the spectral distribution available by application of Ti:Sa-laser femtosecond pulses with $t_p = 200$ fs. Therefore the coherence length of $L_{coh} = 120$ μm is computable, as outlined in chapter 3.5, by ignoring the

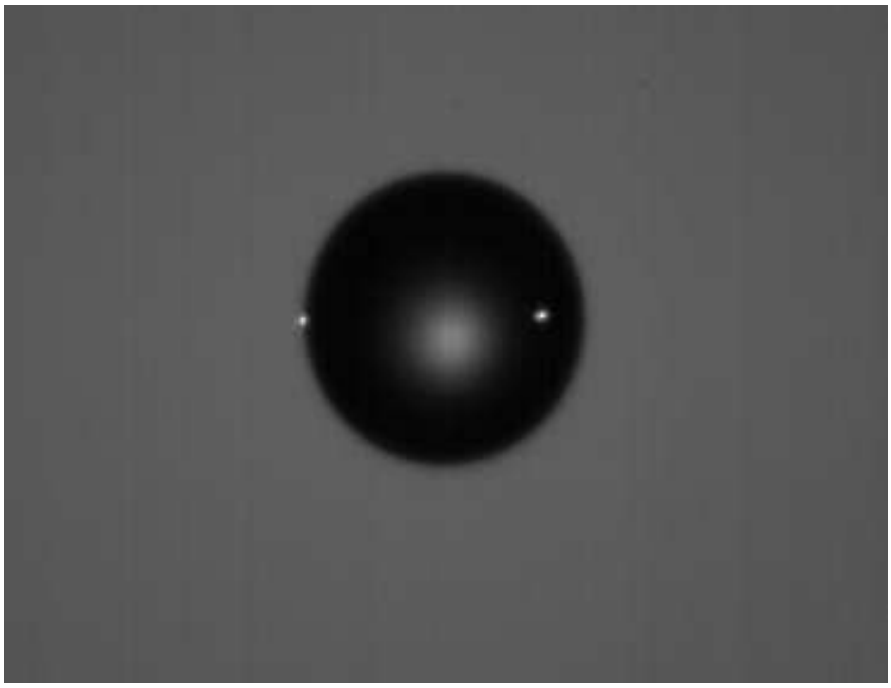

Figure 5.7: Glare points of reflexion (right) and first order refraction ($n = 1{,}333$ and $d_p = 400$ μm). Pulsed illumination with $t_p = 200$ fs.

phase relationship between the contributing wavelengths in the according spectral interval. Hence this study offers the experimental and the numerical foundation for future applications of the feedback-source in Rainbow refractometry.

5.3 Glare Points

So far, the detection of the angular intensity distribution of particles was realized without imaging optics. With imaging optics on top of a bare, e.g., CCD-chip, a transparent, illuminated particle will show multiple bright spots on its surface. The imaging optics can be interpreted as a Fourier transform of the unaltered angular intensity distribution. Fig. 5.6 depicts two rays contributing to glare points in forward direction. One glare point is due to reflection and the other arises from first-order refraction. In general the various scattering orders are each represented by one glare point. Therefore the angle of observation is crucial in determining which glare points will be visible. The case in fig. 5.6 is demonstrated in the laboratory in fig. 5.7. The water droplet, held by the acoustic levitator, was imaged by a CCD-camera. The brightness and the distance between glare points depends on the direction of observation. The absolute distance between glare points on

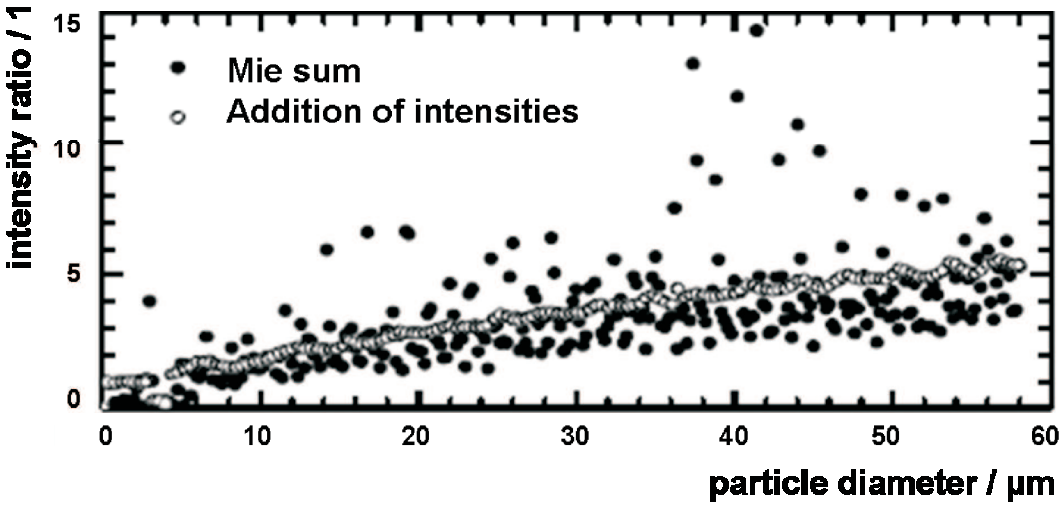

Figure 5.8: Smoothing of the glare point intensity ratio by ultrashort laser pulse illumination. Pulsed illumination leads to the addition of intensities of various scattering orders while cw illumination results in the Mie sum.

the particle is obviously also a function of droplet size. The refractive index of the particle also influences this parameters. Glare points of higher scattering orders have far lower intensities and are therefore difficult to observe. According to Schaller (2000), the ratio of glare point intensities can be used to estimate particle size and refractive index. The ratio of the reflective and first order refraction glare point is depicted in fig. 5.8. For CW illumination the ratio varies strongly for different particle diameters. This is due to interference between scattering orders. The diagram also highlights the striking difference when pulsed illumination is used. Pulsed illumination yields a linear relationship between the ratio of the two glare point intensities and particle diameter. For femtosecond pulse illumination the different scattering orders arrive at the camera lens at different times and therefore can not interfere with one another. This lack of interference results in a smooth linear function.

To experimentally verify this prediction a spray nozzle was chosen, resulting in a polydispersed distribution of particle sizes. The main obstacles encountered while imaging a spray was to identify and assign proper intensity values to sets of glare point pairs. Due to the large number of illuminated droplets per picture, it was necessary to find a method of identifying multiple glare point pairs per single picture to calculate the ratio of the detected intensities. The highly convenient experimental setup used for data collection is depicted in fig. 5.9. An example of a picture that was used for analysis is shown in fig. 5.10. Note the relative

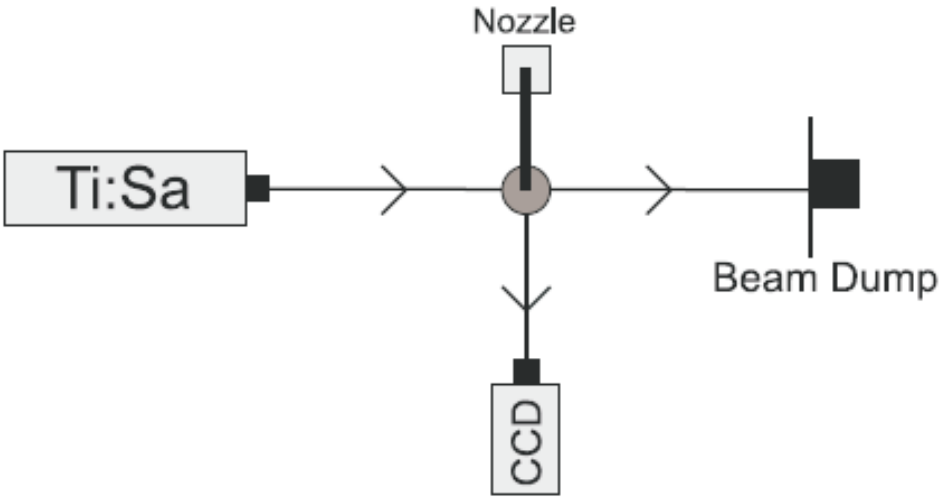

Figure 5.9: Experimental Setup for glare point detection.

weakness of the imaged points, this is due to the high shutter speed required to avoid a blurry picture of the spray.

The Ti:Sa laser provided either CW or $t_p = 200$ fs laser pulse illumination of the droplets leaving the atomizer nozzle at a central wavelength of $\lambda = 780$ nm. The Sensicam QE cooled digital 12bit CCD-detector was equipped with a microscope. The experiment was performed using an ultrasonic atomizer US2 water nozzle. The polarization of the light was parallel to the scattering plane because then the intensities of reflection and first-order refraction are of comparable magnitude. The obtained images were stored in bitmap format. An application specific software uses a function named "subdivider", which scans images in discrete 24*24 pixel squares. These squares are each saved in a 2D array and passed to a second function, which scans the square for both the pixel with the highest grayscale value (most white), which corresponds to the glare point of first order refraction, and the pixel with the second highest grayscale value, for the reflection glare point. The function then returns the positions of both the highest and second highest peaks in intensity as well as their position in the image. The function also checks to see if the pair of points are, in fact, associated glare point pairs. It does this first by taking the mean value of the 24*24 pixel square and checking if both intensity peaks found are above this. It then checks wether the highest peak is at least 20 arbitrary grayscale points above the mean. If the intensity peaks match these criteria and are far enough in x-separation and close enough in y-separation to actually constitute an associated pair of glare points, the function returns that the two peaks are indeed glare points.

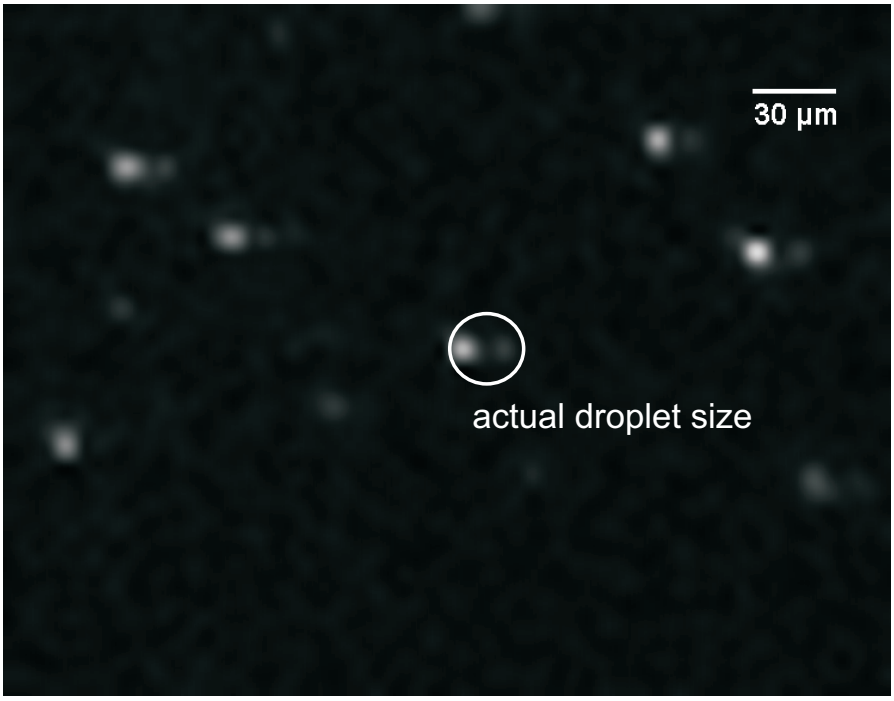

Figure 5.10: Detail of an applied image of glare points in the illuminated spray.

Since pixel data is discrete, the determined peaks had to be refined by fitting the area around the peak to a Gaussian. The fitting of two 1D Gaussians curves, horizontally and vertically, along the intensity peak was sufficient to accurately estimate the correct value of the peak. In order to fit the 1D Gaussians, the value at the peak was used as well as the two surrounding points (either horizontally or vertically). Accordingly, the natural logarithm of the values was calculated. Therefore only a quadratic fitting function was necessary. Gaussian curves are generally expressed as:

$$A \exp[-a(x-b)^2] \tag{5.1}$$

Hence we can form a fit on the data by treating it as a linear combination of fitting functions:

$$f(t) \;=\; \sum_{k=1}^{m} a_k f_k(t) \tag{5.2}$$

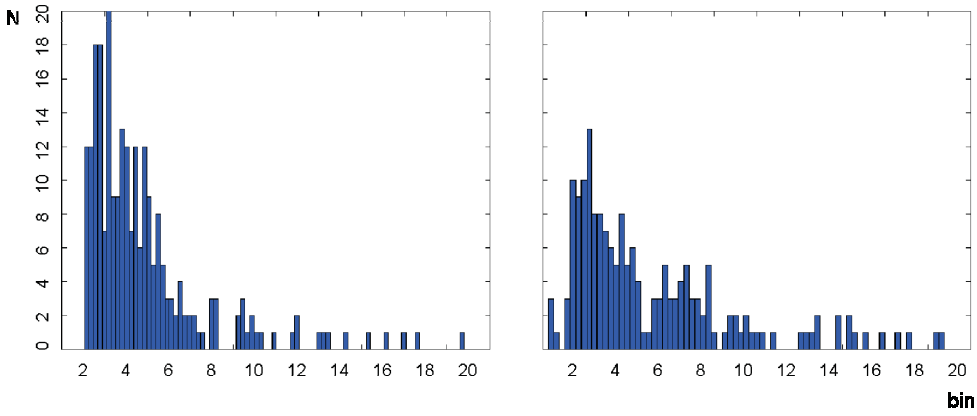

Figure 5.11: Histograms of glare point ratios for (left) pulsed illumination and (right) CW illumination.

f_k(t) are the individual fitting functions (1, x, x^2) with the coefficients a_k. This setup can be treated as a linear system defined by:

$$F\vec{a} \;=\; \vec{b} \tag{5.3}$$

In order to solve it, a pivotless Gauss-Jordan elimination was implemented. The Gaussian amplitude, and therefore the intensity of the glarepoint was retrieved by reverting a quadratic to a Gaussian function:

$$\exp[-ax^2 + bx + c] \;=\; \exp[-a(x + k_1)^2 + k_2] \tag{5.4}$$

Therefore the intensity of the glare point is given by $\exp(c+b^2/4a)$, and the choice of whether to use the horizontal or vertical fit comes from whichever gives us the greatest yield. In other words, both the vertical and horizontal fits were performed and the highest estimated peak was selected.

The plots in fig. 5.11 have been determined from multiple stacks of data. Numerous pictures of the illuminated spray have been analysed with the described

software (fig 5.10). The identified glare point ratios are depicted by absolute value (x-axis) and quantity, for pulsed and CW illumination. An overestimation of absolute values for CW illumination was expected (fig 5.8). Many more glare point pairs are detected in the pulsed illumination case. This is because the CW-ratio tends to drop down to zero for numerous particle diameters (fig 5.8). For the CW case many more pairs with high absolute value are detected. The plot for the pulsed case resembles the expected poisson shape of the nozzle particle size distribution. In contrast the plot for the CW case is not useful in determining the size distribution. The absolute value of the peak position in the pulsed case deviates slightly from the expected mean particle size of $d_p = 30$ μm. This deviation is most likely due to a high signal-to-noise ratio and the neglected influence of overlaps and layering in the spray, which is another source of error.

5.4 Smoothing of the Intensity-Diameter-Function

In the previous paragraphs the angular intensity distribution of illuminated droplets was detected and imaged on a spacious CCD-chip to study the interference phenomena between and within scattering orders. To investigate the local disruptions in the diameter-intensity relationship caused by scattering angle independent morphology independent resonances (MDR), the scattered intensity was focused on a photodiode serving as point detector. By application of a newly developed Paul trap (Heinisch 2006) it was possible to follow the evaporation process of small water droplets illuminated by femtosecond laser pulses.

The experimental setup used to investigate MDR´s under CW and pulsed illumination was almost identical to fig. 4.4. Instead of a CCD-camera a photodiode was used as detector. A water droplet, produced by a HP 51604A Inkjet cartridge, levitated in an electrodynamic Paul trap in ordinary air and without wall contact. Especially droplets in the lower diameter range ($d_p < 30$ μm) are, due to the overwhelming influence of surface tension, nearly ideal spheres and therefore well suited to verify numerical predictions. The droplet was illuminated with a Ti:Sa laser in CW-mode at a wavelength of $\lambda = 784$ nm and an output power of up to $P_{out} = 800$ mW. In pulsed mode $\nu = 75$ MHz repetition rate and a pulse energy of $P_p = 11$ nJ have been applied. The scattered intensity leaving the droplet was directed to the mentioned photodiode detecting with a frequency of $\nu = 10$ kHz. The droplet was imaged onto the diode by a lens collecting scattered light over a horizontal angle of $\alpha = 55°$ to $\alpha = 97°$. Fig. 5.12 depicts the measured intensity distributions for the levitated droplets in the Paul trap in CW and pulsed laser emission mode. The diameter of the droplets has been estimated to be $d_p < 60$

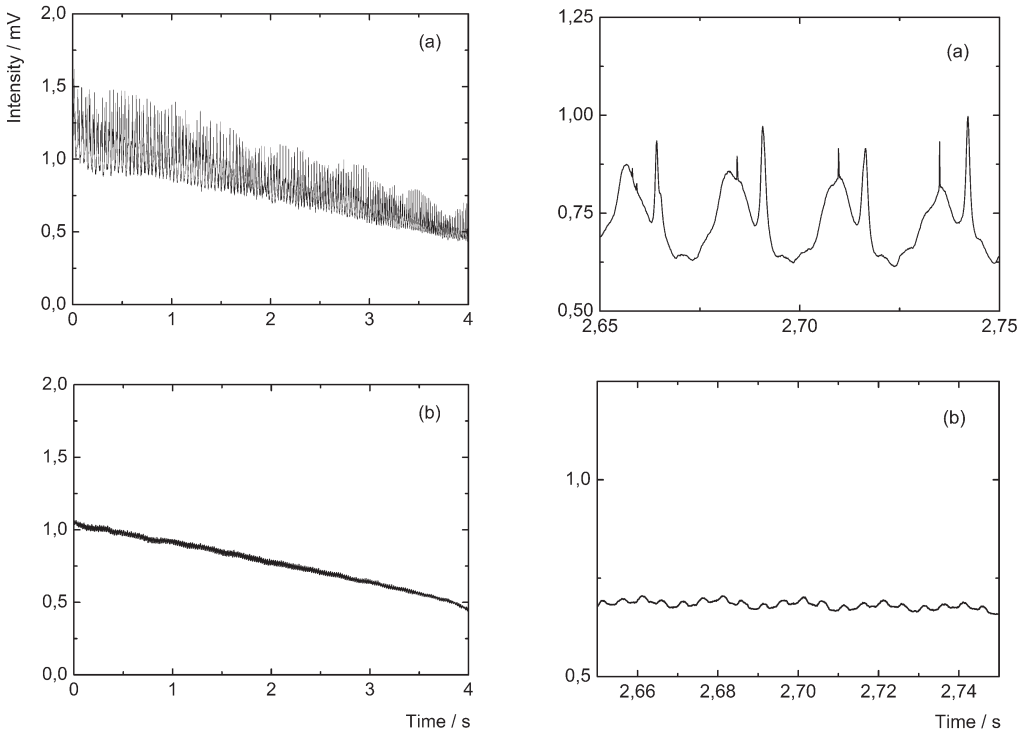

Figure 5.12: Experimentally obtained, temporal intensity distribution in the far field for a range of diameters of an evaporating spherical, homogeneous water droplet positioned in a Paul trap. Upper left diagram: CW illumination ($\lambda = 780$ nm) Upper right diagram: The contribution of MDR´s becomes apparent on an enlarged scale. Lower left diagram: Pulsed illumination ($t_p = 200$ fs, $\lambda = 780$ nm). Lower right diagram: The temporal intensity distribution is free of MDR´s and scattering lobes.

μm by the same method as applied before (Heinisch 2006). The temporal evolution was determined by the evaporation of the droplet. The pronounced intensity variations are consistent with the numerically determined oscillations depicted in fig. 3.16. They are considerably smoothed under pulsed illumination. Moreover, MDR´s are reduced significantly. In fig. 5.12 the right column enlarges part of the left column and highlights the contribution of MDR´s (temporally short peaks in contrast to the wider scattering lobes) to the total scattered intensity fluctuations dependent on the droplet diameter and their absence in the case of illumination with short pulses. The absence results from the pulse energy of ultrashort laser pulses being distributed over a considerable spectral width and the principle of reciprocity in droplets (Hill et al. 2000, Favre et al. 2002). Of course, due to the

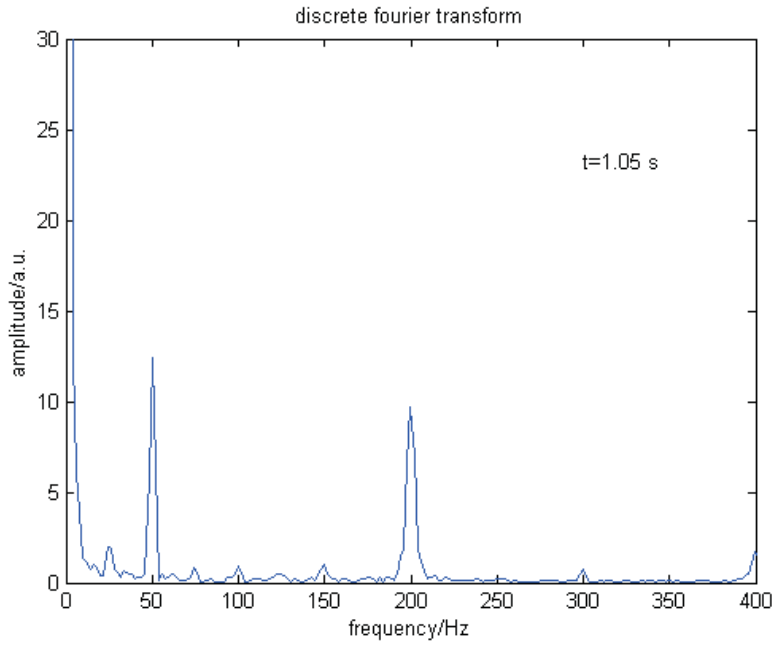

Figure 5.13: Fourier transform of the temporal intensity distribution given in Fig. 5.12 for pulsed illumination.

complex interaction of scattering orders, the scattering function is not monotonic to an equal degree for all scattering angles.

Analysis of the Fourier transform (fig 5.13) confirms the assumption, that the remaining oscillations for pulsed illumination, which can be seen in the enlarged section of fig. 5.12, are caused by the frequency of the ground loop noise ($\nu = 50$ Hz) and the oscillating electrodynamic potential of the Paul trap ($\nu = 200$ Hz). Furthermore, the Fourier transform in fig 5.14 confirms the assumption that the fine intensity peaks on top of the oscillations caused by interference between scattering orders in fig 5.12 for CW illumination are indeed MDR´s. This is because MDR´s of the same full width at half maximum can be idealized as equidistant delta functions in an intensity distribution over particle diameter. Because the Fourier transform of equidistant delta functions is again a spread of equidistant delta functions, the peaks in fig. 5.14 confirm the presence of such a pattern in the original temporal intensity distribution (Bakic et al. 2008).

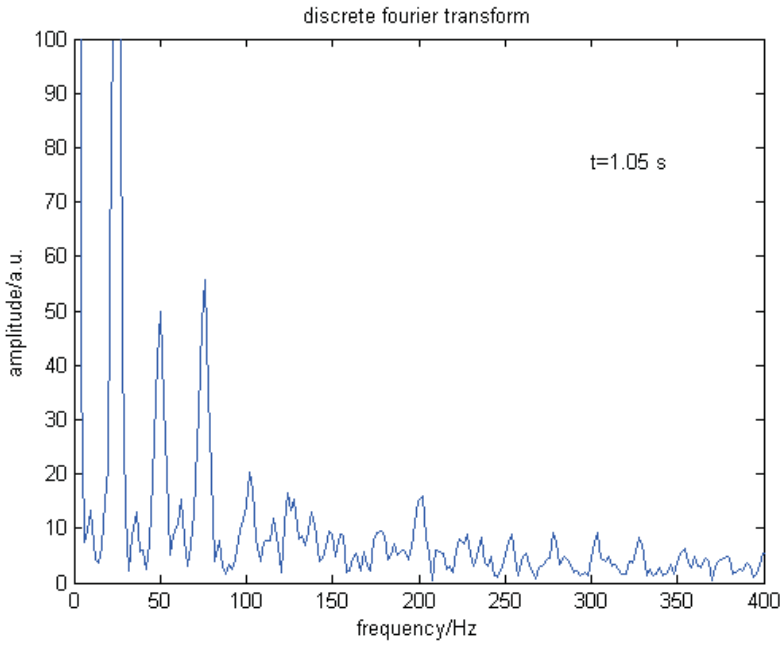

Figure 5.14: Fourier transform of the temporal intensity distribution given in fig. 5.12 for CW illumination.

5.5 Sauter Mean Diameter

The Sauter mean diameter (SMD) is a common parameter used in fluid dynamics to estimate the average particle size in a spray and is defined as the average droplet volume divided by the average droplet surface:

$$SMD = \frac{\frac{1}{N}\sum_{i=1}^{N} d_i^3}{\frac{1}{N}\sum_{i=1}^{N} d_i^2} \tag{5.5}$$

N stands for the number of particles and d_i is the diameter of the according droplet i. Physically this stands for the assumption that all involved particles have the same diameter and in result the same ratio of d^3 to d^2. Because d^2 is proportional to the average droplet surface and therefore the evaporation rate, and d^3 is proportional to the average droplet volume and therefore the evaporated mass, the SMD is especially useful in combustion or evaporating environments.

A method for SMD measurement, and therefore spray characterization, is planar

droplet sizing (PDS) (Yeh 1993, Sankar 1999). It gives results to some extent independent of fluctuations of the incident laser intensity and is applicable in dense sprays. The spray is illuminated with a laser light sheet and the Mie-intensity scattered by the dye doped particles is measured, as well as the laser induced fluorescence. The PDS technique relies on the assumption that the intensity emitted by the fluorescent dye is proportional to the volume of the droplet ($\propto \mathrm{d}_p^3$) and that the scattered Mie-intensity is proportional to its surface area ($\propto \mathrm{d}_p^2$). It is also assumed, that this is valid for multiple droplets with a spectrum of droplet sizes (Sankar 1999, LeGal 1999). If the absorption of the incident laser beam in the dye doped particle is insignificant, the ratio of the average fluorescence and Mie signals is proportional to the SMD:

$$SMD \;\propto\; C_{SMD}\frac{\sum_{i=1}^{N} d_i^3}{\sum_{i=1}^{N} d_i^2} \;=\; \frac{I_{fluorescence}}{I_{mie}} \tag{5.6}$$

The scattered light measured from particles in a laser light sheet brings to mind the diameter-intensity relationship for small particles described in chapter 3.6 and experimentally investigated in chapter 5.4. For small particles the oscillations from interference between scattering orders and intensity peaks due to MDR's become overwhelming, inducing an error in relationship 5.6 (Domann and Hardalupas 2001a). As discussed in chapter 3.5, with femtosecond laser pulses of $t_p = 50$ fs the diameter-intensity relationship can be, in certain angles, significantly smoothed for particles down to $\mathrm{d}_p = 5\ \mu$m.

How does addition of a dye to the liquid account for fluorescence? According to Guilbault (1990), the fluorescence intensity emitted due to absorbtion over a specific pathlength x within a liquid with a dye concentration c_{dye} is given by:

$$I_{fl} = \Phi_{qe} I_0 [1 - exp(-\epsilon x c_{dye})] \tag{5.7}$$

Φ_{qe} is the quantum efficiency and I_0 the incident intensity. The molar extinction coefficient ϵ is fixed for the corresponding dye. In order to use this method to calculate the fluorescence intensity emitted by a droplet within an experimentally neglectable error margin, light absorption over the corresponding distances within the sphere covered by the first three refractive scattering orders has to be determined for all angles of incidence. Reverse raytracing of scattered light calculations,

using geometrical optics, provides the total intensity entering the sphere at each incident angle. A problem arises at angles leaving the sphere around the rainbow angles, where geometrical optics are not applicable. These intensities are obtainable by either linear interpolation or geometric surface wave approximation. The intensity ratios of the reflected and transmitted rays at the particle surface are given by the Fresnel coefficients.

To assess the accuracy of the geometrical optics approximation for the fluorescence intensity given by dye loaded droplets, the internal intensity distribution is calculated in Domann and Hardalupas (2001b). The internal energy-density distribution is calculated in the meridional plane of a liquid droplet and can be assumed to be proportional to the fluorescence intensity (Zhang and Alexander 1992). For spherical particles of large size parameter, elastic scattering processes are generally treated by geometrical optics in the formulation of van de Hulst (1981). This approach can be expanded to calculate the energy-density distribution inside a non-resonant, non-absorbing sphere illuminated by a plane wave (Chowdhury et al. 1992, Velesco et al. 1997). With the exception of the energy density at focal points and focal lines, it provides a good approximation if the computational grid is larger than the wavelength. As mentioned before, using the notation of van de Hulst (1981), reverse ray tracing of scattered light provides the total intensity of a ray entering the sphere for each incidence angle, while the intensity ratios of the reflected and transmitted rays at each interface are given by the Fresnel coefficients. Consequently, the intensity at the start of the path of a ray entering the sphere can be determined. The known path distance is then divided into discrete segments and, using the Lambert-Beer law, it is possible to determine the absorbed intensity on each segment, and consequently the intensity of the ray at discrete positions on its path. The internal energy-density distribution can then be calculated on a 2D uniform grid. This approach provides the correct energy density, if uniform absorption and unpolarized light are assumed.

In the work at hand a fluorescence model was utilized which is based on Lorenz-Mie theory (Mees et al. 2001c), the determination of the incident fluence field inside the droplet and on the raytracing methods to calculate the fluorescence intensity (Frackowiak et al. 2007). The laser fluence field E_{liq} is computed in the liquid phase with a code developed at CORIA (Mees et al. 2001c). In this model the complete resolution of the Maxwell equations inside a sphere illuminated by a continuous monochromatic plane wave is incorporated. The computation is axisymmetric, and the refractive index inside the sphere is set to be uniform. The absorption is taken into account through the imaginary part of the complex refractive index. The light scattering is also modeled. Assuming the temperature, pressure and density to be uniform, and the fluorescence to be isotropic in the liquid phase, the signal $S_{fluo,liq}$ is proportional to the local laser fluence E_{liq}, with

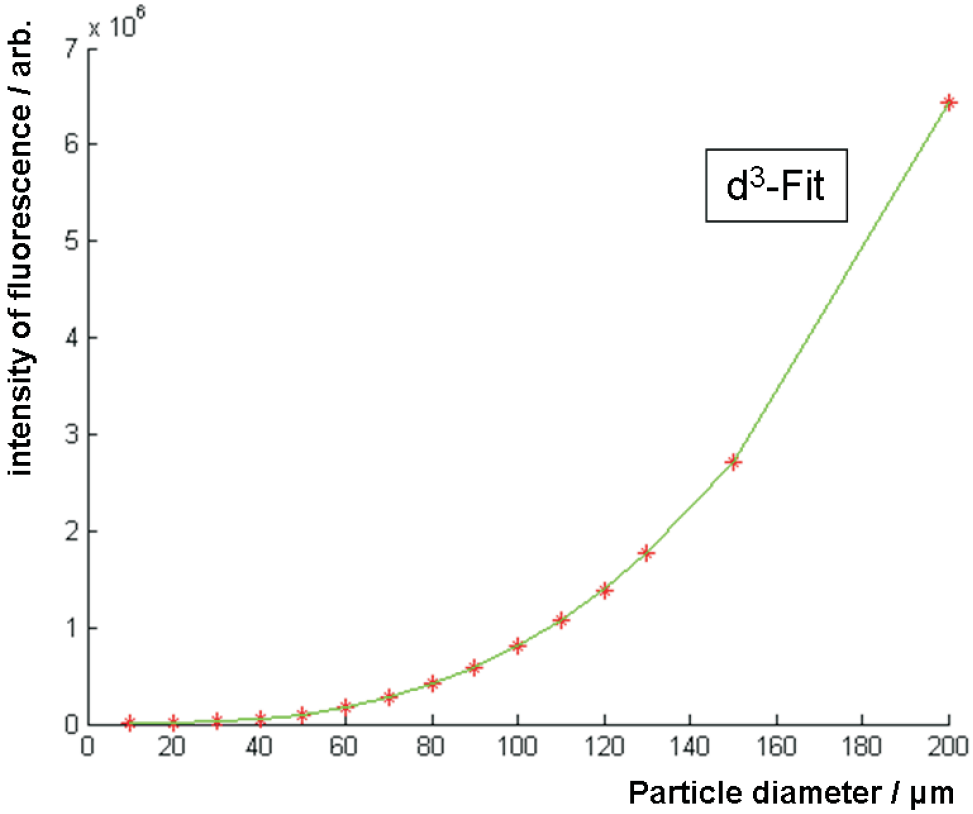

Figure 5.15: Numerically obtained intensity distribution for fluorescence for various droplet diameters. Coumarin 102 (concentration $c = 1.5{*}10^{-5}$ mol/l) was assumed to be dissolved in ethanol ($n = 1.3614$).

the same factor at every point in the droplet (Thurber 1999). In contrast to the incident laser light, due to a different wavelength range, the fluorescence signal is not absorbed by the liquid. The fluorescence contribution of a ray is deduced by adding the fluence values on each discrete volume dV_c of the liquid phase intersecting the ray, taking into account the non-uniform transmission factor T_{trans} over the droplet surface. Consequently the fluorescence contribution of each discrete emerging ray can be computed. This allows the construction of a fluorescence image for a single droplet, as well as a distribution of fluorescence intensities for multiple droplets with different diameters.

Such a distribution is depicted in fig. 5.15, with parameters provided by the experimental verification outlined in the following paragraphs. The depicted intensities are in line with the predicted D^3-distribution, in contrast to experimental results (Domann and Hardalupas 2001b). The experimental deviation, manifest-

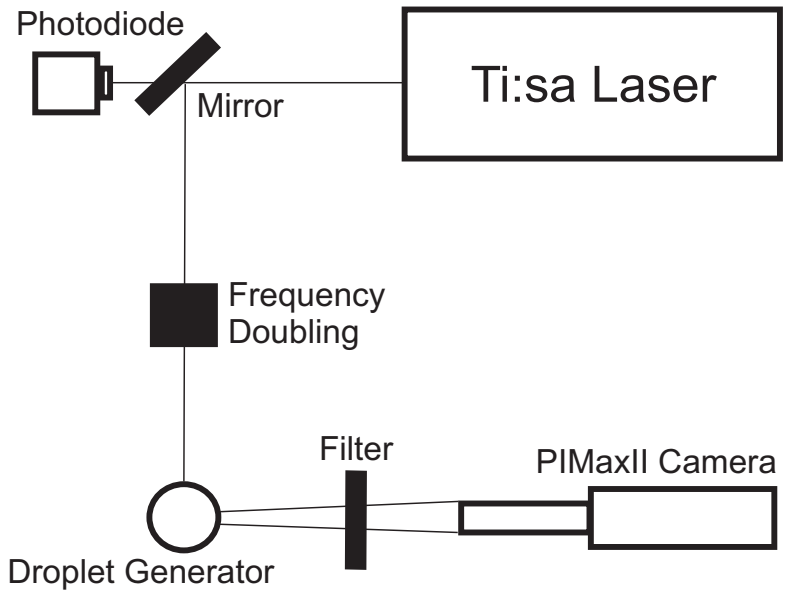

Figure 5.16: Experimental setup for the measurement of LIF and Mie signals from monodisperse droplet streams illuminated with femtosecond laserpulses.

ing itself in oscillations of fluorescence intensities around the expected D^3-fit for various droplet diameters, is not well understood. It is suspected to be a consequence of MDR´s due to the causality of incident light and fluorescence (Domann and Hardalupas 2001b). Therefore an experimental smoothing of the intensity-diameter distribution for fluorescence is expected as well for illumination with femtosecond laserpulses.

While the effect of smoothing the Mie signal for various diameters was proven on a stationary, single, evaporating small particle (chapter 5.4), the spray environment for SMD measurements was approximated by utilizing a monodisperse droplet stream to verify the principle of error reduction for future applications in sprays. The corresponding experimental setup depicted in fig. 5.16 included, besides a droplet stream generator, an Ar+ pumped Ti:Sa fs-laser system (Spectra Physics: Solstice) with variable pulse length minimal at $t_{pulse} = 100$ fs and $\lambda = 400$ nm in combination with a nonlinear crystal for frequency doubling. Illumination at $\lambda = 400$ nm was necessary due to the poor quantum efficiency of the Camera PIMaxII ICCD (Princeton Instruments, $n_{pixel} = 1300$*1340, $t_{gate} = 2.6$ μs) with long distance microscope ($x_{res} = 5$ μm / pixel) and fluorescent dyes in general at the commonly used wavelength of $\lambda = 780$ nm. A photodiode was used as reference for the output intensity of the laser. Due to the vast difference in magnitude between the scattered Mie signal and the intensity of the laser induced fluorescence (LIF) a GG435 filter was placed in front of the camera. LIF was made possible

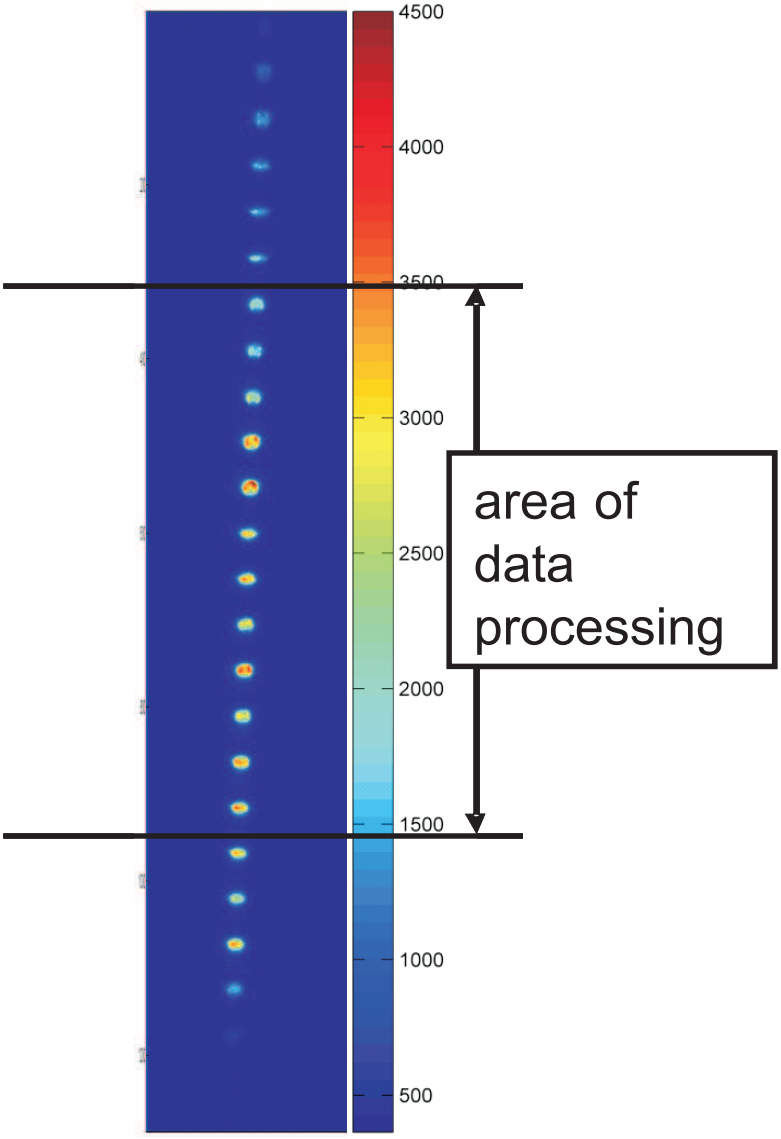

Figure 5.17: Image of the LIF signal from a droplet stream illuminated with femtosecond laserpulses (t_p = 300 fs, Coumarin 102 with $c = 1.5{*}10^{-5}$ mol/l dissolved in ethanol) (Bareiss 2009)).

by dissolving traces of Coumarin 102 in ethanol. The absorbtion maximum of Coumarin 102 in ethanol (refractive index n = 1.3614) is at λ = 389 nm and the fluorescence maximum at λ = 465 nm. Correspondingly, the filter blocked any illumination up to λ = 420 nm and therefore the Mie signal. The transmission of the filter is T_{trans} = 0.9 for λ = 450 nm and higher wavelengths. Conversely,

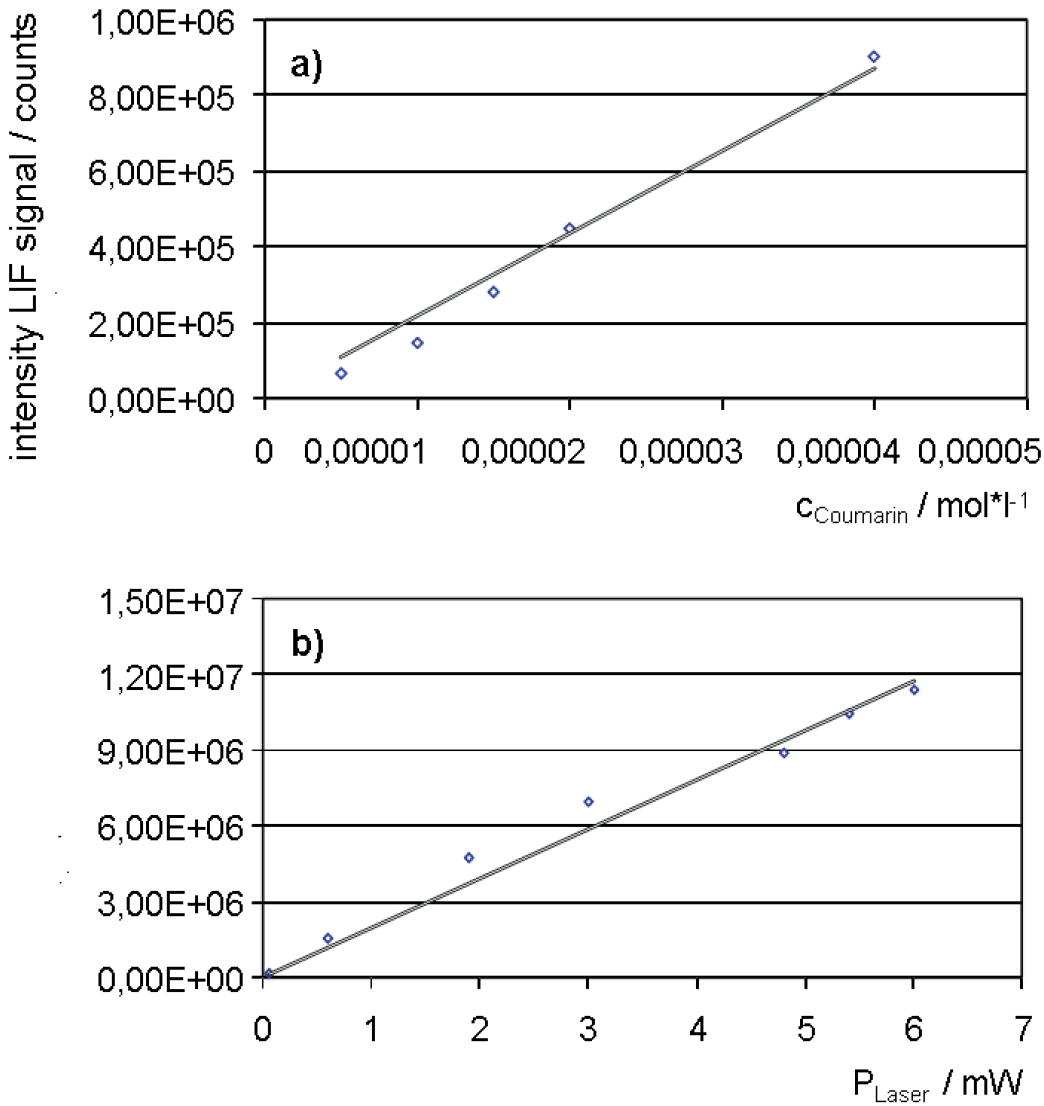

Figure 5.18: Linearity verification for a range of dye concentrations (Coumarin 102 in ethanol) and laser intensities for the experimental setup at hand (Bareiss 2009).

no filter was necessary to record the Mie signal. The fluorescence was to weak to alter the results.

To quantify the detected LIF and Mie intensities an area of interest was defined in the images recorded by the camera (fig. 5.17), constricted to the droplets made visible by the well illuminated center of the 2-dimensional Gaussian laser beam

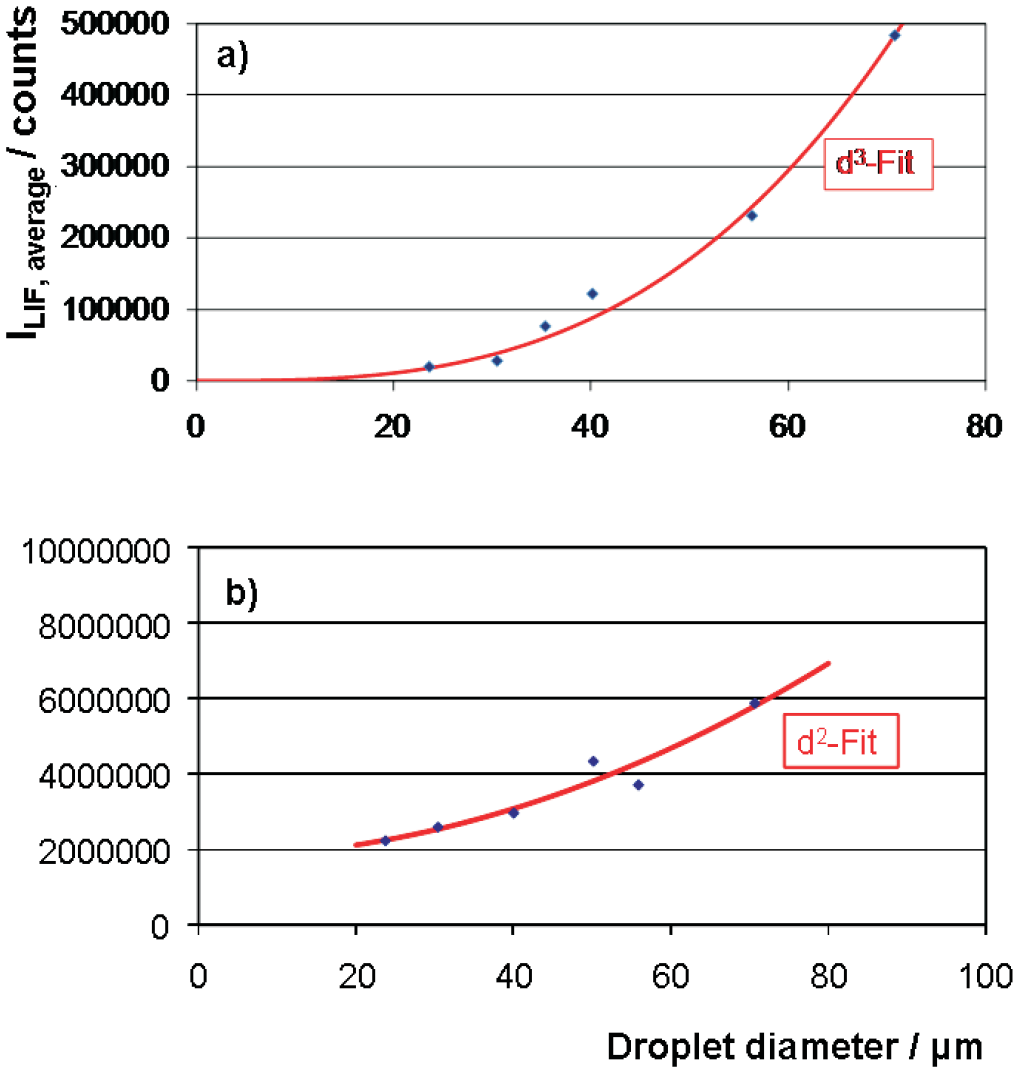

Figure 5.19: Fitted LIF and Mie signals from monodisperse droplet streams with a range of average diameters (Bareiss 2009).

profile (D_{beam} = 1 cm). It was then possible to average over a statistically relevant amount (>2000) of mean intensity values determined from each droplet by

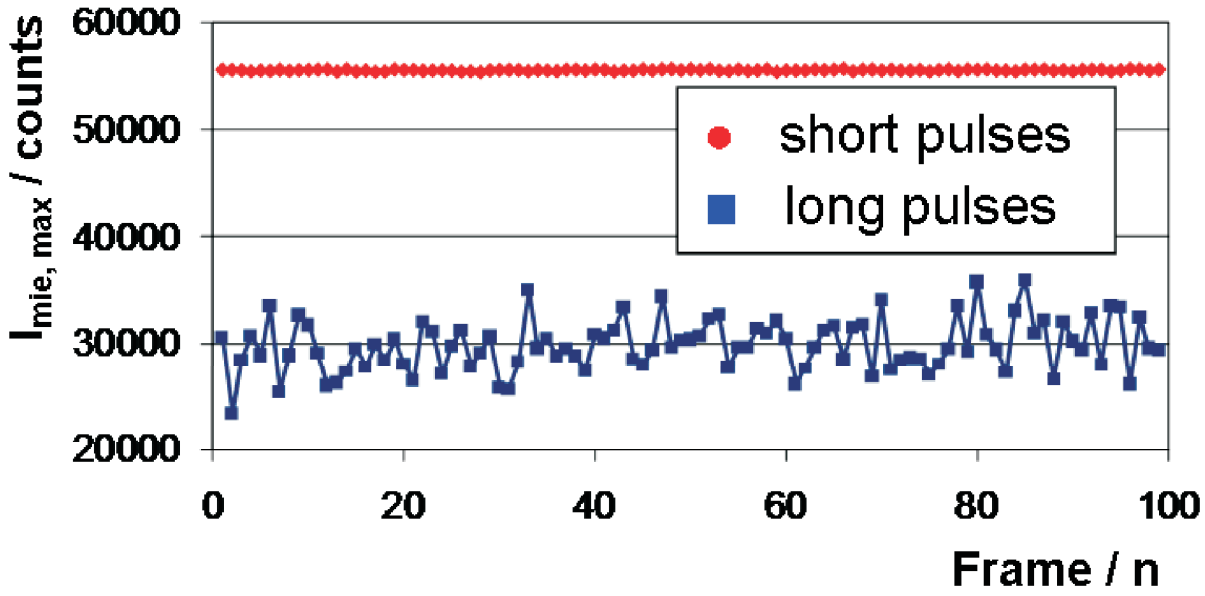

Figure 5.20: Averaged maximal intensities of the Mie signal within single droplets (d_p = 20 μm) illuminated with femtoseond laserpulses (t_p = 300 fs and t_p > 1 ps) for a series of images. Adapted from FG Energie- und Kraftwerkstechnik (Prof. J. Janicka, Prof. A. Dreizler, Stefan Bareiss).

summing up the counts per pixel. The droplet positions and diameters in the images have been determined with software appendant to the camera system. Three pinhole sizes (d_{ph} = 10 μm, 20 μm, 30 μm) have been used in combination with the droplet generator to alter the average size of the droplets in the monodisperse stream. To double the amount of available diameters, the frequency of the droplet stream was modified as well.

As depicted in fig. 5.18, to assure the comparability of the measured intensities for different droplet diameters, the linearity of the LIF signal to the chosen range of dye concentration and the laser power was confirmed respectively. Evidently, these measurements have been performed for a fixed droplet diameter (d_p = 40 μm). The results have been averaged over a relevant number of images, as outlined before and applied to all remaining evaluations in this set of measurements as well.

To verify the assumption of the LIF signal following a cubic fit and the Mie signal a quadratic dependence a further series of measurements was performed for various average droplet diameters (concentration of Coumarin 102 in ethanol: c_{dye} = 1.5*10^{-5} mol/l). As can be seen in fig. 5.19 a), the determined LIF intensities follow the cubic fit surprisingly well. Moreover the Mie signal follows a quadratic

fit as expected for illumination with femtosecond laser pulses (fig. 15.19 b)).

Nevertheless, in addition to the low signal to noise ratio for the LIF signal, the laser pulse length turned out to be an unfortunate source of experimental error. For the measurements at hand a minimal pulse length of only $t_p = 300$ fs was achieved, causing oscillations in the diameter-intensity relationship for particles smaller then $d_p = 25$ μm. Unaware of this fact, the influence of femtosecond pulses on the results was further investigated. Droplets with diameters below the critical value ($d_p = 20$ μm) have been illuminated with longer pulses ($t_p > 1$ ps) equivalent to CW for particles in this size range and compared with results for the minimal pulse length. Fig. 5.20 depicts averaged maximal intensities of the Mie signal within single droplets for a series of images. Because of the results in chapter 5.3 a smoothed curve for minimal pulse lengths was expected, due to reduced intensity fluctuations of the dominant glare point. Likewise the curve should be less smooth for longer pulses, because in this case the intensities of the glare points are less steady. Fig. 5.20 seems to confirm this assumption. However, the results for longer and shorter pulses are reversed if not only the pixel with the maximal intensity is considered, but the overall intensity of single droplets is summed up and averaged. As verified experimentally in chapter 5.4, this cannot be the case. But because the method of identifying and assessing the dominant glare point seems less prone to the mentioned sources of error, it is preferable. Regardless of this inconclusiveness, the overall results make a strong case for the application of femtosecond laser pulses for SMD measurements in sprays with small particles and should be further investigated.

Chapter 6

Outlook for Particle Characterization with Short Coherence Length Laser Sources

Beyond experimental verification the characteristics of the scattering function for small particles illuminated by femtosecond laser pulses imply the prospect of enhancing various existing particle characterization techniques. The particular case of separation within second refractive order and the smoothing of the ripple structure obviously advances Rainbow refractometry, whereas the separation between scattering orders in general is proposed to improve interferometric particle imaging (IPI). Moreover, the benefits of femtosecond laser pulse illumination for intensity-diameter, and therefore Sauter mean diameter (SMD), measurements are discussed relating to planar droplet sizing (PDS).

6.1 Rainbow Refractometry for Small Particles

The purpose of Rainbow refractometry is the determination of particle temperature by measuring the refractive index of the according transparent agent. This is achieved by detecting the angular intensity distribution, in particular the region of the primary rainbow. Typically the particle is a liquid, homogeneous droplet. So far, two implementations have been realized for refractive index measurements in sprays, by Sankar et al. (1993) and van Beeck and Riethmuller (1995). As depicted in fig. 5.1, Sankar et al. (1993) added a standard phase Doppler device to a Rainbow refractometry instrument. In combination such an instrument was expected to not only determine the refractive index and therefore temperature of particles, but also particle size due to the stand-alone phase Doppler component. The size information allows for a more precise numerical analysis of the measured data. In

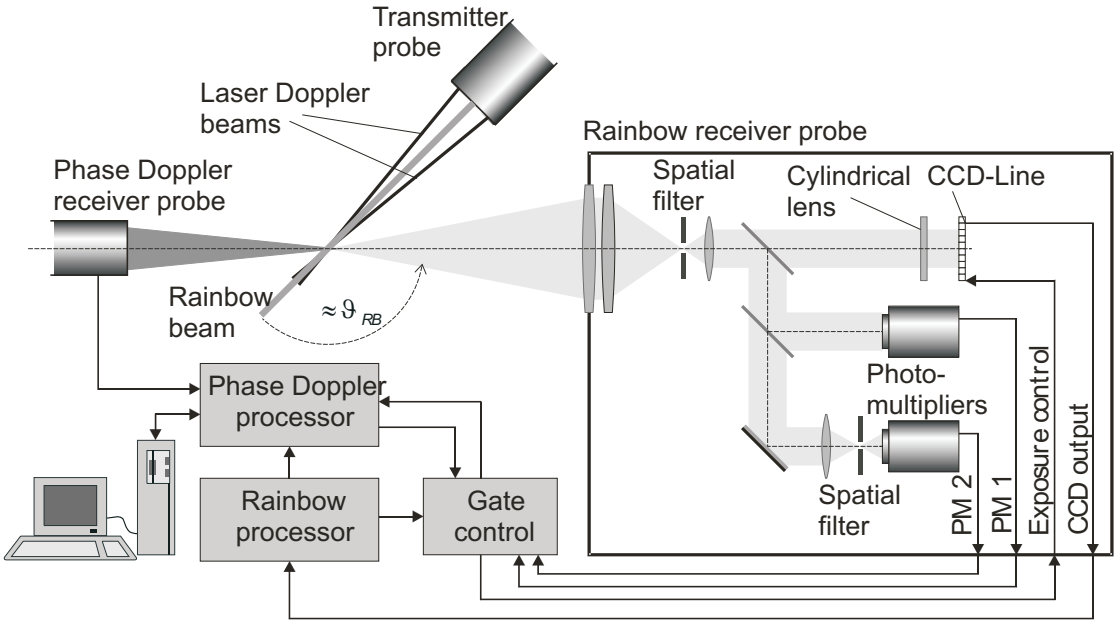

Figure 6.1: Depiction of an integrated phase Doppler/rainbow refractometry device (adapted from Sankar et al. 1993).

the rainbow receiver part of the set-up the rainbow pattern is imaged by a cylindrical lens on a high-speed and -resolution 1-dimensional CCD-array. The signals of two implemented photomultipliers are used to synchronize the measurement with the phase Doppler device and to optimize the detection of the signal intensity by the CCD-array. However, the system had no broader commercial success due to the extreme sensitivity of the angular intensity distribution to non-sphericity and refractive index inhomogeneities inside the droplet (Massoli 1998).

As discussed in chapter 3.5 and 5.1, the primary rainbow of a spherical, homogeneous droplet refers to the angular intensity pattern emerging through interference within the second-order refraction and additional interference with the surface reflection. As shown by Roth (1996), the position of the inflection point next to the maximum intensity rainbow peak is nearly size independent. Because the angular intensity distribution of the rainbow shifts almost linearly with refractive index, this has been used to determine droplet temperature (van Beeck et al. 1999). The ripple-structure, emerging due to interference with surface reflection, overlays the supernumerary bows of the second-order refraction. A measurement instrument has to relate the angular intensity frequencies of this pattern to size and refractive index of the droplet. This is realized by application of Lorenz-Mie theory. The ripple structure can be a help in determining the size of larger particles if the detected signal is fitted to numerical prediction. However, for small particles

($d_p < 30$ μm) the amplitude of the ripple structure becomes substantial, and the information contained by the supernumerary bows of an individual droplet is concealed. The deviation increases rapidly for smaller particles. The accuracy of the refractive index measurement is therefore significantly limited, as investigated by Heukelbach (1998). A further limitation of Rainbow refractometry is due to the sensitivity of the angular intensity distribution to non-sphericity (Marsten, 1980). Larger droplets are by no means perfect spheres and therefore size and refractive index errors quickly accumulate. However, because of the increasing influence of surface tension, small droplets are far more spherical. And because the ripple structure is caused by the interference of second-order refractive order and surface reflection, femtosecond laser pulses can be used to improve the accuracy of rainbow refractometry for small droplets. A white light source would of course eliminate the ripple structure, too, but the interference within the second order refraction is needed to create the supernumerary bows. The coherence length of the light source must be short enough to separate the according scattering orders in time and space, but long enough to cause interference within the scattering orders. This can also be achieved with the semiconductor laser source using optical feedback with good illumination intensity as presented in chapter 5.2.

An alternative method of limiting the defective influence of the ripple structure and non-sphericity on temperature determination with Rainbow refractometry is the application of global Rainbow thermometry (GRT), as proposed by van Beeck et al. (1999) and implemented by Saengkaew et al. (2007). In GRT the rainbow patterns of many individual droplets are averaged, and therefore the average size and temperature of a particle ensemble is detected. However, this is a statistical measurement technique. Rainbow refractometry with femtosecond laser pulses gives the future prospect of an in-situ measurement technique avoiding the shortcomings of the classical system by Sankar for small particles ($d_p < 30$ μm). In principle, compared to GRT, in-situ measurement additionally allows the quantification of fluxes and concentration of particle ensembles. Moreover, the introduction of short coherence length laser sources with adaptable coherence length as in Peil (2006) allow for a compact, cost-efficient implementation.

6.2 Interferometric Particle Imaging (IPI)

Interferometric particle imaging (IPI) developed from a succession of studies by König et al. (1986), Ragucci et al. (1990) and Glover et al. (1995). The corresponding method is explainable on the basis of geometrical optics. As depicted in fig. 6.1, two scattering orders of a spherical particle are considered whose intensity is of the same magnitude, e.g. reflective and first refractive order. A focused image will display the corresponding glare points. The spatial separation

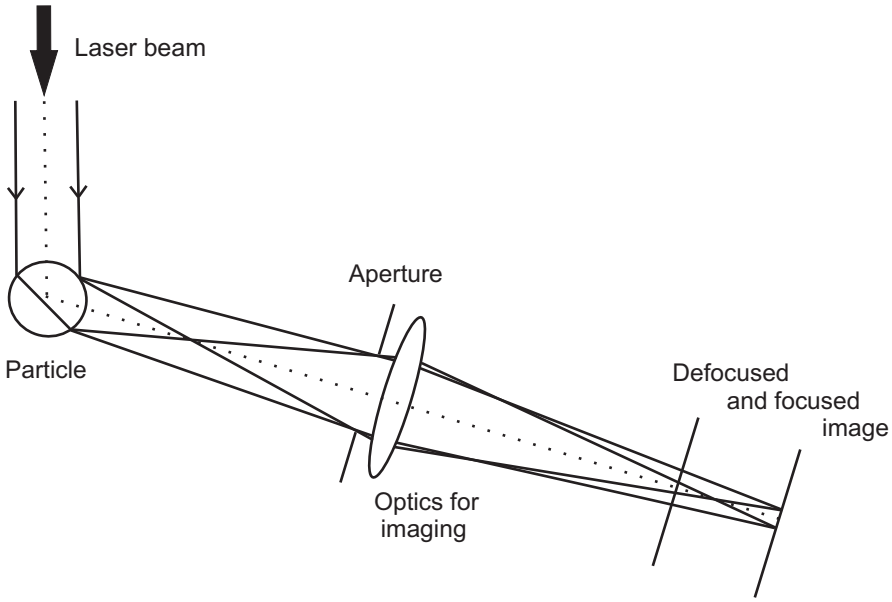

Figure 6.2: The IPI technique in principle.

of them contains information about size. However, as discussed in Schaller (2000), morphology dependent resonances prevent an exactly linear relationship between particle size and glare point distance on individual particles. Moreover, because of the excellent image resolution necessary (Hess 1998, 2009), imaging and distance measurements of focused glare points established by CW laser illumination lack a clear advantage over common, back-lighted imaging of single particles. For an out-of-focus particle though, interference fringes induced by the rays emitted by the two glare points appear at the intersection of the two images (fig 6.2). If the two images are defocused strongly, they merge into a single image of interference fringes. The profile of the defocused images depends solely on the profile of the utilized aperture, while the size of the various images corresponds to the extent of defocussing. The angular frequency of the interference fringes is a function of particle size, due to the path length difference between e.g. the reflection and first order refraction scattering orders. It evolves inversely proportional to the particle size.

The technique is obviously expandable to multiple particles by using a 2D laser light sheet. An image of a spray depicts large particles by more fringes and small particles by less (fig 6.3). The size of the particle image on the out-of-focus plane is not related to the particle size, but depends on the position of the detection plane relative to the focal plane of the experimental setup. As an alternative to counting a higher number of fringes a Fourier transform can be applied to determine the

spatial frequency. On the one hand, using scattering angles with more than two glare points helps validating the results, because the size can be estimated by more than one combination between scattering orders. On the other hand, validating more then two glare points simultaneously leads to higher orders of interference fringes and therefore prevents straightforward implementation of the technique. Experimentally, the interference fringes are in accord with the oscillating scattering lobes appearing in the angular intensity distribution diagrams calculated with Lorenz-Mie theory. As discussed for the angular intensity distribution for second order refraction in chapters 3.4, 3.5 and 5.1, femtosecond laser pulses allow for a temporal and spatial separation of the reflection order and second-order refraction. For scattering angles in the rainbow region interferometric particle imaging can therefore be enhanced to consider the contribution of second order refraction without the perturbing influence of the reflection order. Overall, the illumination with femtosecond laser pulses or short coherence length laser sources with adaptable coherence length as in Peil (2006a,b) establishes an additional degree of freedom in fitting the coherence length to a specific problem and therefore angle of detection. Within the limits of the scattering function (chapter 3.5) this allows for a choice of which glare points should be considered to contribute to the interference fringes.

Moreover, as discussed in chapter 5.3, illumination of small particles with femtosecond laser pulses or semiconductor devices with optical feedback allow for direct size measurement from focused images of a thin spray. As mentioned before, for CW illumination MDR´s prevent an exactly linear relationship between particle size and glare point distance on individual particles. With illumination by femtosecond laser pulses not only MDR´s are smoothed significantly (chapter 5.4), but the demands for excellent imaging resolution are lessened because the size of small particles is quantifiable from comparing the intensities of specific glare points, not the exact detection of spatial glare point separation.

6.3 Planar Droplet Sizing (PDS)

Planar imaging techniques are widely used, especially in the area of qualitative and quantitative measurements in the gas phase region. These techniques can provide a large spatial and temporal information simultaneously. Nevertheless it remains difficult for imaging techniques so far established to characterize dense sprays. As discussed in chapter 5.5, a promising method for spray characterization applicable in dense sprays is the planar droplet sizing (PDS) technique (Yeh 1993, Sankar 1999), also known as laser sheet drop sizing (LSD) or Mie/LIF technique. It uses the fluorescence intensity emitted from a dye added to and the Mie signal scattered from liquid droplets to determine droplet sizing information. Fig 6.4 gives

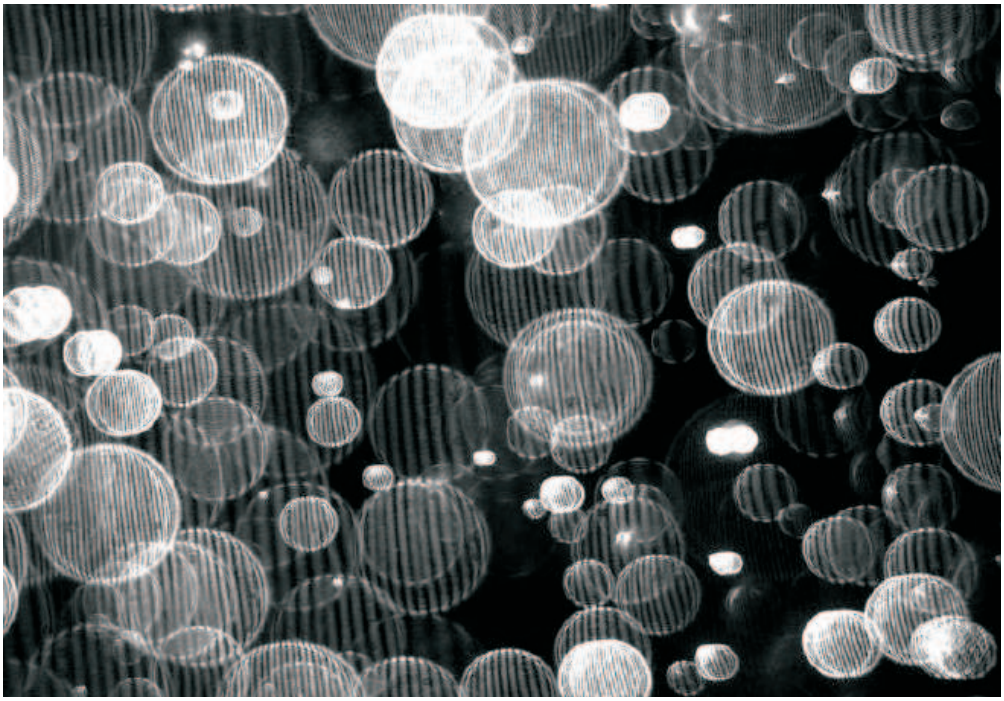

Figure 6.3: Defocused image from a water spray with d_p = 20 μm... 400 μm (Adapted from Albrecht et al. 2003).

an overview of a representative experimental setup. A light sheet constructed from a laser source is directed into a spray cone of particles. The Mie signal and laser induced fluorescence (LIF) intensities are detected simultaneously during the illumination of the spray. The principle of the technique relies on the assumption that the LIF signal emitted by the fluorescent dye is proportional to the volume of the droplet and the Mie signal is proportional to its surface area. The ratio of the two intensities from an illuminated plane of a spray is proportional to the Sauter Mean Diameter (SMD). The SMD is a common parameter used in fluid dynamics to estimating the average particle size in a spray. It is defined as the diameter of a sphere that has the same volume or surface area ratio as a particle of interest (chapter 5.5).

In general, LIF requires high intensity laser pulses to distinguish the emission induced by the laser source from further emission, for example in commonly investigated processes like combustion. The emission not induced by the laser can be suppressed, e.g., by multiple orders of magnitude if the laser pulses are combined with gated detection of the LIF signal. The high intensity is necessary for high excitation efficiency and hence for the high sensitivity of LIF. Moreover, the laser source should be tunable, because the excitation of the involved molecules is due

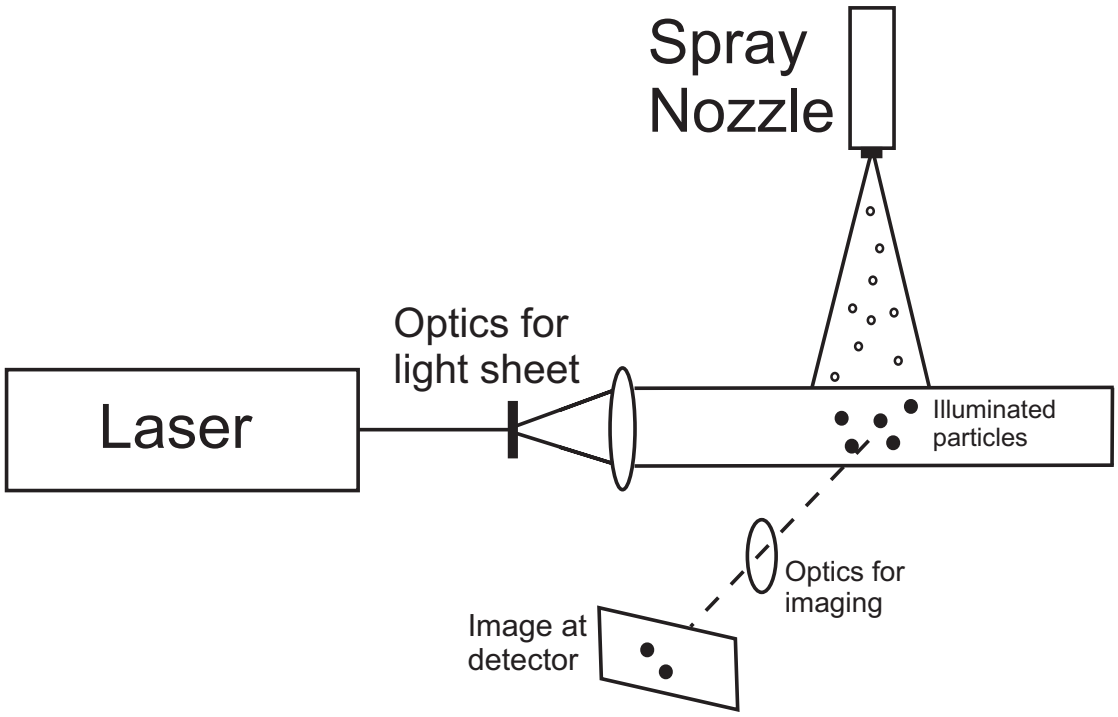

Figure 6.4: Experimental setup for PDS

to resonant processes. Typically Nd:YAG lasers are used as a pump source, allowing for tunable laser emission in the visible part of the spectrum. To generate the deep UV emission ($\lambda < 250$ nm) necessary for the analysis of most combustion problems, nonlinear effects like frequency doubling are employed. Alternatively tunable examiner lasers can be used for this frequency range, or, with many advantages, Ti:Sa femtosecond laser systems.

A Ti:Sa system provides ultrashort laser pulses, and therefore significantly higher illumination intensities per pulse compared to the nano- and picosecond regime of conventional LIF setups. As a consequence spatially wide laser sheets can be employed and multiphoton fluorescence becomes applicable. Moreover this systems are well tunable and allow for extremely fast gating. Two displaced detectors with picosecond shutter time facilitate the measurement of the fluorescence quenching rate. Also, the study at hand provides experimental and numerical results which indicate the favorable application of femtosecond laser pulses for SMD measurements in sprays with small particles. Because the ratio of the Mie and the LIF signal is proportional to the SMD, the error in calculating this parameter for small particles can be reduced by smoothing the oscillations in the Mie diameter-intensity relationship.

Chapter 7

Conclusion

In this thesis the time integrated detection of scattered femtosecond laser pulses, and illumination from a CW semiconductor laser source with optical feedback and adaptable coherence length, has been investigated for small particles. In this context the scattering function for small particles was numerically advanced. The angular distribution of local maxima of the scattering function has been presented for small particles under ultrashort pulse illumination. The position of local maxima relating to scattering angle, particle size and refractive index was calculated with Fourier-Lorenz-Mie theory. Moreover, an estimate of the sensitivity of the scattering function to non-sphericity has been presented, utilizing general Lorenz-Mie theory. For ultrashort pulse illumination the maxima of the supernumerary bows of the primary rainbow were freed from disturbing interferences with reflection order and higher refractive order contributions. The progression of the maxima with particle size and refractive index corresponded directly with the function of second-order refraction. The presented results quantify the pulse duration or coherence length for the desired lower size range, which is essential information for future experimental studies.

The time-integrated angular intensity distribution of scattered laser pulses with t_p = 200 fs on water droplets with a diameter of d_p = 94 μm has been measured in an angular range where the second-order refraction, also known as the first-order rainbow, is dominant. With this the suppression of the ripple structure, which obscures the angular intensity distribution of second-order refraction, has been demonstrated successfully. While the rainbow measurement technique is not applicable for non-spherical single particles, because of the overwhelming influence of the non-sphericity on the rainbow´s angular position, small particles attain a spherical and stable form rapidly due to surface tension. Consequently, the angular position of the rainbow and, thus, the refractive index are expected to be determined with greater precision for spherical droplets and particles smaller than

$d_p = 30$ μm. Together with the experimental application of the semiconductor source with optical feedback, which combines many advantageous properties, such as well-directional light, high output power of $P = 110$ mW, good beam properties and controllable short coherence length of $L_{coh} = 50$ μm with the prospect of reduction to the order of $L_{coh} = 100$ μm, this indicates the feasibility of precise in-situ measurements with Rainbow refractometry for highly spherical small particles with compact and cost-efficient sources of illumination.

Moreover, we experimentally determined the intensity scattered by water droplets of diameter less than $d_p = 60$ μm, integrated over a certain solid angle under the illumination of $t_p = 200$ fs pulses. In this way a substantial reduction of morphology dependent resonances for microscopic water droplets has been successfully demonstrated. The use of the electrodynamic trap, together with the Ti:Sa laser allowed, for the first time, to successfully observe the scattering of femtosecond laser pulses on water droplets not only during a short period of milliseconds as in a droplet stream, but also over the temporal evolution of the evaporating droplet. As the diameter of droplets in sprays changes in general, this can be seen as an important step towards spray diagnostics using femtosecond laser pulses. The new geometry of the electrodes of the electrodynamic trap does not restrict the horizontal observation angle for the scattered light. Therefore it was possible to center the detector easily at the necessary scattering angle of $\Theta = 76°$, being in the range where the scattering function can be made monotonic down to a droplet diameter of less than $d_p = 35$ μm for $t_p = 200$ fs, according to theory. A further smoothing of the scattering function for shorter pulse lengths to less then $d_p = 5$ μm was predicted numerically.

Beyond Rainbow refractometry, these results indicate the feasibility of new measurement techniques and the significant enhancement of existing methods. Under the aspect of the separation of scattering orders, interferometric particle imaging can be enhanced by fitting the coherence length to the angle of detection. Illumination of small particles with femtosecond laser pulses has been shown to facilitate direct size measurement from focused images of a thin spray by measurement of the intensity ratio of specific glare points on individual particles. Moreover, the smoothing of the diameter-intensity function for small particles allows for more precise determination of the Sauter mean diameter in the named size range. Due to the introduction of coherence length as a variable parameter for small particle characterization, the advantages of time integrated detection of femtosecond laser pulses scattered by small particles are underscored by the outlook of utilizing spatially compact and cost-efficient semiconductor laser devices with the important benefit of adjustable coherence length.

References

Agrawal G.P. (1995) Semiconductor lasers. AIP, Woodbury.

Albrecht H.-E., Bech H., Damaschke N., Feleke M. (1995) Berechnung der Streuintensität eines beliebigen im Laserstrahl positionierten Teilchens mit Hilfe der zweidimensionalen Fouriertransformation. Optik (100):118-124.

Albrecht H.-E., Borys M., Damaschke N., Tropea C. (2003) Laser Doppler and Phase Doppler Measurement Techniques. Springer-Verlag, Heidelberg.

Al Zaitone B. (2009) Drying of multiphase single droplet in ultrasonic levitator. PhD-Thesis, Technische Universität Darmstadt, Darmstadt, Germany.

Azouz A., Stelmakh N., Langlois P., Lourtioz J-M., Gavrilovic P. (1995) Non-linear chirp compensation in high-power(>100W) broad spectrum (20nm) pulses from mode-locked AlGaAs lasers. IEEE STQE (1):557-582.

Bakic S., Heinisch C., Damaschke N., Tschudi T., Tropea C. (2008) Time integrated detection of fs-laserpulses scattered by small droplets. Appl. Opt. (40):523-530.

Bakic S., Xu F., Damaschke N., Tropea C. (2009) Feasibility of extending rainbow refractometry to small particles using femtosecond laser pulses. Part. Part. Syst. Charact. (26):34-40.

Bareiss S., Dreizler A., Janicka J. (2009) By oral communication, Fachgebiet Energie- und Kraftwerkstechnik, Technische Universität Darmstadt, Darmstadt, Germany.

Baumert T., Grosser M., Thalweiser R., Gerber G. (1991) Femtosecond time-resolved molecular multiphoton ionisation: The Na_2 system. Phys. Rev. Lett. (67):3753

Bech H., Leder A. (2004) Particle sizing by ultrashort laser pulses - numerical simulation. Optik (115):205-217.

Bech H., Leder A.(2006) Particle sizing by time - resolved Mie calculations - a numerical study. Optik (117):40-47.

Berrocal E., Churmakov D.Y., Romanov V.P., Jermy M.C., Meglinski I.V. (2005) Crossed source-detector geometry for a novel spray diagnostic: Monte Carlo simulation and analytical results. Appl. Opt. (13):2519-2529.

Bohren C.F., Huffmann D.R. (1983) Absorption and Scattering of Light by Small Particles. John Wiley and Sons, New York

Born M. (1981) Optik. Springer-Verlag, Berlin.

Born M., Wolf E. (1999) Principles of optics. Cambridge University Press, London.

Brenn G., Durst F., Tropea C. (1996) Monodisperse sprays for various purposes - their production and characteristics. Part. Part. Syst. Charact. (13):179-185

Card J.B.A., Jones A.R. (1991) Measurement of the refractive index of atomised liquid drops by light scattering. Part. Part. Syst. Charact. (1-4):267-273.

Chowdhury D.Q., Barber P.W., Hill S.C. (1992) Energy-density distribution inside large nonabsorbing spheres by using Mie theory and geometrical optics. Appl. Opt. (31):3518-3523.

Clemmow P.C. (1966) The Plane Wave Spectrum Representation of Electromagnetic Fields. Pergamon Press Oxford, New York.

Colak S. (1978) Focused laser beam scattering by stationary and moving particles. PhD thesis, University of California, USA.

Damaschke N., Heukelbach K., Tropea C. (1998) Messung von Partikeldurchmesser, Brechungsindex und Temperatur mit dem Regenbogen. Proceedings 6. Fachtagung Lasermethoden in der Strömungsmeßtechnik (GALA), Essen, Germany.

Damaschke N., Nobach H., Semidetnov N., Tropea C. (2002a) Optical particle sizing in backscatter. Appl. Opt. (27):5713-5727.

Damaschke N., Michel T., Tropea C. (2002b) Streuung von Femtosekunden-Pulsen an sphärischen Partikeln. Proceedings 10. Fachtagung Lasermethoden in der Strömungsmesstechnik (GALA), Rostock Germany.

Damaschke N. (2003) Light scattering theories and their use for single particle characterization. PhD Thesis, Technische Universität Darmstadt, Darmstadt, Ger-

many.

Damaschke N., Nobach H., Nonn T.I., Semidetnov N., Tropea C. (2005) Multi-dimensional particle sizing techniques. Exp. Fluids (2):336-350.

Debye P. (1908) Das elektromagnetische Feld um einen Zylinder und die Theorie des Regenbogens. Physikalische Zeitschrift (9):775-778.

Debye P. (1909) Der Lichtdruck auf Kugeln von beliebigem Material. Ann. Phys. (30):57-136.

Demtröder W. (2003) Laser Spectroscopy: Basic Concepts and Instrumentation. Third Edition, Springer-Verlag, Heidelberg.

Domann R., Hardalupas Y. (2001a) A study of parameters that influence the accuracy of the planar droplet sizing (PDS) technique. Part. Part. Syst. Charact. (1):3-11.

Domann R., Hardalupas Y. (2001b) Spatial distribution of fluorescence intensity within large droplets and its dependence on dye concentration. Appl. Opt. (40):3586-3597.

Favre C., Boutou V., Hill S.C., Zimmer W., Krenz M., Lambrecht H., Yu J., Chang R.K., Woeste L., Wolf J.P. (2002) White-light nanosource with directional emission. Phys. Rev. Lett. (89):035002.

Fork R., Shank C., Yen R., Hirlimann C. (1983) Femtosecond optical pulses. IEEE J. Quantum Electron. (19):500-506.

Frohn A., Roth N. (2000) Dynamics of Droplets. Springer-Verlag, Heidelberg.

Frackowiak B., Strzelecki A., Lavergne G. (2007) Vapor concentration measurement around vaporizing droplets by the PLIF technique. Comparison with the numerical simulation. Proceedings, 6th International Conference on Multiphase Flow (ICMF), Leipzig, Germany.

Gillespie J.B., Ligon D.A., Pellegrino P.M., Fell N.F., Wood N.J. (2002) Development of a broadband LIDAR system for remote determination of aerosol size distributions. Meas. Sci. Technol. (3):383.

Glover A.R., Skippon S.M., Boyle R.D. (1995) Interferometric laser imaging for droplet sizing: a method for droplet-size measurement in sparse spray systems. Appl. Opt. (34):8409-8421.

Gor´kov (1962) On the forces acting on a small particle in an acoustical field in an ideal fluid. Soviet Physics-Doklady (6):773-775.

Gouesbet G., Gréhan G., Maheu B. (1988) Computations of the coefficients gn in the generalized Lorenz-Mie theory using three different methods. Appl. Opt. (27):4874-4883.

Gouesbet G., Gréhan G., Maheu B. (1989) On the generalized Lorenz-Mie theory (GLMT): First attempt to design a localized approximation to the computation of the coefficients g n. J Opt (20):31-43.

Gouesbet G., Mees L. (1999) Generalized Lorenz-Mie theory for infinitely long elliptical cylinders. J. Opt. Soc. Am. A (16):1333-1341.

Gouesbet G., Gréhan G. (2000a) Generic formulation of a generalized Lorenz-Mie theory for a particle illuminated by laser pulses. Part. Part. Syst. Charact. (5-6):213-224.

Gouesbet G., Gréhan G. (2000b) Generalized Lorenz-Mie theories, from past to future. Atom & Sprays (10):277-333.

Gouesbet G. (2003) Debye series formulation for generalized Lorenz-Mie theory with the Bromwich method. Part. Part. Syst. Charact. (20):382-386.

Guilbault G.G. (1990) Practical Fluorescence. Marcel Dekker Inc., New York.

Heinisch C., Bakic S., Damaschke N., Petter J., Tschudi T., Tropea C. (2006) Neue Paulfallengeometrie zur Fixierung von Tropfen und Partikeln in Gasströmungen mit 360°-Zugang für Laserdiagnostik. Proceedings 14.Fachtagung Lasermethoden in der Strömungsmesstechnik (GALA), Braunschweig, Germany.

Hess C.F. (1998) Planar particle image analyzer. Proceedings 9th Int. Symp. on Appl. of Laser Anemom. to Fluid Mech., Lisbon, Portugal.

Hess C.F., L´Esperance D. (2009) Droplet imaging velocimeter and sizer: a two-dimensional technique to measure droplet size. Exp. Fluids (47):171-182.

Heukelbach K., Hom J., Chigier N. (1998) Capabilities and limitations of the rainbow refractometer, determined with temperature measurements of water droplets. ILASS-Americas 1998, Sacramento, USA.

Hill S.C., Boutou V., Yu J., Ramstein S., Wolf J.P., Pan Y.L., Holler S., Chang R.K. (2000) Enhanced backward-directed multiphoton-excited flourescence from dielectric microcavities. Phys. Rev. Lett. (85):54-57.

Hom J. (2000) Rainbow refractometry: A non-intrusive measurement technique for determining droplet-size, refractive index and temperature. PhD Thesis, Carnegie Mellon University, Pittsburgh, USA.

Hovenac E.A., Lock J.A. (1992) Assessing the contribution of surface waves and complex rays to far field Mie scattering by use of Debye series. J. opt. Soc. Am. A (9):781-795.

Huibers P.D.T. (1997) Models for the wavelength dependence of the index of refraction of water. Appl. Opt. (36):3785-3787.

Jewell J.L., Scherer A., McCall S.L., Lee Y.H., Walker S., Harbison J.P., Florez L.T. (1989) Low-threshold electrically pumped vertical-cavity surface-emitting microlasers. Electron. Lett. (25):1123-1124.

Jones A.R., Parasram N.T., Taylor A.M.K.P. (2002) Numerical simulation of the sizing performance of the shadow doppler velocimeter (SDV). Meas. Sci. Technol. (3):317-330.

Kahre V., Nussenzveig H.M. (1977) Theory of the glory. Phys. Rev. Lett. (38):1279-1282.

Kerker D.M. (1969) The Scattering of Light. Academic Press, New York.

King L.V. (1934) On the acoustic radiation pressures on spheres. Proc. R. Soc. London, Ser. A (147):212-240.

König G., Anders K., Frohn A. (1986) A new light-scattering technique to measure the diameter of periodically generated moving droplets. J. Aerosol. Sci. (17):157-167.

Koroll H. (2009) Verwendung kostengünstiger Breitbandquellen zur Charakterisierung homogener und inhomogener Partikel mittels Fluoreszenz und Zeitverschiebungstechnik. Master Thesis, Universität Rostock, Rostock, Germany.

Kowalewicz A. (1984) Combustion Systems of High-Speed Piston I.C. Engines. Elsevier, Amsterdam.

Lami J.-F., Petit S., Hirlimann C. (1999) Self-steepening and self-compression of ultrashort optical pulses in a defocusing CdS crystal. Phys. Rev. Lett. (82):1032-1035.

Lavieille P., Delconte A., Blondel D., Lebouche M., Lemoine F. (2004) Non-intrusive temperature measurements using three-color laser-induced fluorescence.

Exp. Fluids (5):706-716.

Lefebvre A. (1986) Atomization and Sprays. Hemisphere Publishing, New York.

Le Gal P., Farrugia N., Greenhalgh D.A. (1999) Laser sheet dropsizing of dense sprays. Opt. Laser Technol. (31):75-83.

Leung E., Jacobi N., Wang T. (1981) Acoustic radiation force on a rigid sphere in a resonance chamber. J. Acoust. Soc. Am. (70):1762-1767.

Linne M.A., Paciaroni M., Gord J.R., Meyer T.R. (2005) Ballistic imaging of the liquid core for a steady jet in crossflow. Appl. Opt. (44): 6627-6634.

Lorenz L. (1890) Lysbevaegeiseni og uden for en hal plane lysbôlger belyst kulge. Vidensk Selk Skr (6):1-62.

Maeda M., Akasaka Y., Kawaguchi T. (2002) Improvements of the interferometric technique for simultaneous measurement of droplet size and velocity vector field and its application to a transient spray. Exp. Fluids (1):125-134.

Marsten P.L. (1980) Rainbow phenomena and the detection of nonsphericity in drops. Appl. Opt. (19):680-685.

Massoli P. (1998) Rainbow refractometry applied to radially inhomogeneous spheres: the critical case of evaporating droplets. Appl. Opt. (37):3227-3234.

Mees L., Gouesbet G., Gréhan G. (2001a) Scattering of laser pulses (plane wave and focused Gaussian beam) by spheres. Appl. Opt. (40):2546-2550.

Mees L., Gréhan G., Gouesbet G. (2001b) Time-resolved scattering diagrams for a sphere illuminated by plane wave and focused short pulses. Opt. Commun. (194):59-65.

Mees L., Gouesbet G., Grehan G. (2001c) Interaction between femtosecond pulses and a spherical micro cavity: internal fields. Opt. Commun. (199):33-38.

Mees L., Wolf J.-P., Gouesbet G., Gréhan G. (2002) Two-photon absorption and fluorescence in a spherical micro-cavity illuminated by using two laser pulses: Numerical simulations. Opt. Commun. (4-6):371-375.

Midwinter J.E. (1979) Optical Fibers for Transmission. Wiley, New York.

Michel T. (2002) Streuung von Femtosekundenpulsen an sphärischen und geschichteten Partikeln. Diploma thesis, Technische Universität Darmstadt, Darmstadt, Ger-

many.

Mie G. (1908) Beiträge zur Optik trüber Medien, speziell kolloidaler Metallösungen. Annalen der Physik (4):377-452.

Mollenauer L.F., Stolen R.H., Gordon J.P. (1980) Experimental observation of picosecond pulse narrowing and solitons in optical fibers. Phys. Rev. Lett. (45):1095-1098.

Nasr G.G., Yule A.J., Bending L. (2002) Industrial Sprays and Atomization: Design, Analysis and Applications. Springer-Verlag, New York.

Nikander K. (1997) Nebulization of suspensions. J. Aerosol Med. (10):89.

Nikolaus B., Grischkowsky D. (1983) 90-fs tunable optical pulses obtained by two stages pulse compression. Appl. Phys. Lett. (43):228-230.

Nishino K., Kato H., Torii K. (2000) Stereo imaging for simultaneous measurement of size and velocity of particles in dispersed two-phase flow. Meas. Sci. Technol. (6):633-645.

Nussenzveig, H.M. (1969a) High-frequency scattering by a transparent sphere, I. Direct reflection and transmission. J. Math. Phys. (10):82-124.

Nussenzveig, H.M. (1969b) High-frequency scattering by a transparent sphere, II. Theory of the rainbow and the glory. J. Math. Phys. (10):125-176.

Oberlé J., Jonusauskas G., Abraham E., Ruillière C. (1995) Enhancement and sub-picosecond dynamics of optical non-linearities of excited-states: transstilbene in solution. Chem. Phys. Lett. (241):281.

Onofri F., Gréhan G., Gouesbet G. (1995) Electromagnetic scattering from a multilayered sphere located in an arbitrary beam. Appl. Opt. (34):7113-7124.

Onofri F. (1999) Critical angle refractometry for simultaneous measurement of particles in flow: Size and relative refractive index. Part. Part. Syst. Charact. (3):119-127.

Onofri F., Girasole T., Grehan G., Gouesbet G., Brenn G., Domnick J., Xu T.-H., Tropea C. (1996) Phase-Doppler anemometry with the dual burst technique for measurement of refractive index and absorption coefficient simultaneously with size and velocity. Part. Part. Syst. Charact. (2):112-124.

Onofri F., Guering P.-H., Radev S.(2004) Light scattering properties and high-

resolution diffractometry of homogeneous and non homogeneous fibers. OPC 2004, Kyoto, Japan.

Palero V., Lobera J., Arroyo M.P. (2005) Digital image plane holography (DIPH) for two-phase flow diagnostics in multiple planes. Exp. Fluids (2):397-406.

Pedrotti F., Pedrotti L., Bausch W., Schmidt H. (2002) Optik für Ingenieure. Grundlagen. Zweite Auflage. Springer-Verlag, Heidelberg.

Peil M., Fischer I., Elsäßer W. (2006a) Spectral broadband dynamics of semiconductor lasers with resonant short cavities. Phys. Rev. A (73):023805.

Peil M., Fischer I., Elsäßer W., Bakic S., Damaschke N., Tropea C., Stry S., Sacher J. (2006b) Rainbow refractometry with a tailored incoherent semiconductor laser source. Appl. Phys. Lett. (89):091106.

Quan X., Fry E.S. (1995) Empirical equation for the index of refraction of seawater. Appl. Opt. (34):3477-3480.

Ragucci R., Cavaliere A., Massoli P. (1990) Drop sizing by laser light scattering exploiting intensity angular oscillation in the Mie regime. Part. Part. Syst. Charact. (7):221-225.

Raupach S.M.F., Vössing H.J., Curtius J., Borrmann S. (2006) Digital crossed-beam holography for in situ imaging of atmospheric ice particles. J. Opt. A: Pure Appl. Opt. (9):796-806.

Rayleigh J.W.S. (1879) On the instability of jets. Proceedings of the London mathematical society (10):4-13.

Rayleigh L. (1910) The problem of the whispering gallery. Phil. Mag. (20):1001-1004.

Ren K.F., Gréhan G., Gouesbet G. (1997) Scattering of a Gaussian beam by an infinite cylinder in the framework of generalized Lorenz-Mie theory: formulation and numerical results. J. Opt. Soc. Am. A (14):3014-3025.

Roll G. (1999) Optische Mikroresonatoren: Beschreibung im Bild der geometrischen Optik. PhD Thesis, Ruhr-Universität Bochum, Bochum, Germany.

Roth N. (1998) Bestimmung des Brechungsindex in Einzeltropfen aus dem Streulicht im Bereich des Regenbogens. Shaker-Verlag, Aachen.

Roze C., Girasole T., Mees L., Grehan G., Hespel L., Delfour A. (2003) Interac-

tion between ultra short pulses and a dense scattering medium by Monte Carlo simulation: Consideration of particle size effect. Opt. Commun. (4-6):237-245.

Rullière C. (Ed.), Hirlimann C. (2005) Femtosecond Laser Pulses. Springer-Verlag, Berlin.

Saengkaew S., Charinpanitkul T., Vanisri H., Tanthapanichakoon W., Biscos Y., Garcia N., Lavergne G., Mees L., Gouesbet G., Gréhan G. (2007) Rainbow refractrometry on particles with radial refractive index gradients. Exp. Fluids (43):595-601.

Sankar S.V., Ibrahim K.M., Buermann D.H., Fidrich M.J., Bachalo, W.D. (1993) An integrated phase Doppler/rainbow refractometer system for simultaneous measurement of droplet size, velocity, and refractive index. Proceedings 3rd International Congress on Optical Particle Sizing, Yokohama, Japan.

Sankar S.V., Maher K.E., Robart D.M. (1999) Spray characterization using a planar droplet sizing technique. J. Eng. Gas Turb. Power (121):409.

Sbanski O., Roman V.E., Kiefer W., Popp J. (2000) Elastic light scattering from single microparticles on a femtosecond time scale. J. Opt. Soc. Am. A (2):313-319.

Schelinsky B. (2002) Charakterisierung von Streuteilchen durch laseroptische Meßverfahren mit strukturierten Empfängern. PhD Thesis, Universität Rostock, Rostock, Germany.

Schaller J.K., Wasserberg S., Fiedler D.K., Stojanoff C.G. (1994) A new method for temperature measurements of droplets. Proceedings 6th International Conference of Liquid Atomization and Spray Systems (ICLASS), Rouen, France.

Schaller J. K. (2000) Laseroptische Messtechnik: Erweiterung bestehender Verfahren und Entwicklung neuer Techniken. Habilitation Thesis, RWTH Aachen, Aachen, Germany.

Shifrin K.S., Zolotov I.G. (1994) Quasi-stationary scattering of electromagnetic pulses by spherical particles. Appl. Opt. (33):7798.

Shifrin K.S., Zolotov I.G. (1995) Nonstationary scattering of electromagnetic pulses by spherical particles. Appl. Opt. (3):552.

Shank C.V., Bjorkholm J.E., Kogelnik H. (1971) Tunable Distributed-Feedback Dye Laser. Appl. Phys. Lett. (18):395.

Thormählen I., Straub J., Grigull U. (1985) Refractive index of water and its de-

pendence on wavelength, temperature and density. J. Phys. Chem. Ref. Data. (14):933-945.

Thurber M. C. (1999) Acetone laser induced fluorescence for temperature and multiparameter imaging in gaseous flows. Thesis report TSD-120, Stanford University, USA.

Tinker S., di Marzo M., Tartarini P., Chandra S., Quiao Y.M. (1995) Dropwise evaporation cooling: effect of dissolved gases and effect of surfactants. Proceedings Int. Conf. on Fire Research and Engineering (101):48-71.

Vahala K. (2004) Optical Microcavities. World Scientific Publishing, Singapore.

van Beeck J.P.A.J., Riethmuller M.L. (1995) Nonintrusive measurements of temperature and size of single falling raindrops. Appl. Opt. (34):1633-1639.

van Beeck J.P.A.J. (1997) Rainbow phenomena: Development of a laser based, non-intrusive technique for measuring droplet size temperature and velocity. PhD Thesis, Techn Uni Eindhoven, Eindhoven, Netherlands.

van Beeck J.P.A.J., Giannoulis D., Zimmer L., Riethmuller M.L. (1999) Global Rainbow thermometry for droplet-temperature measurement. Opt. Lett. (23):1696-1698.

van de Hulst H.C. (1981) Light Scattering by Small Particles. Dover Publications, New York.

Velesco N., Kaiser T., Schweiger G. (1997) Computation of the internal field of a large spherical particle by use of the geometrical-optics approximation. Appl. Opt. (36):8724-8728.

Vetrano M.R., van Beeck J.P.A.J., Riethmuller M.L. (2004) Global rainbow thermometry: improvements in the data inversion algorithm and validation technique in liquid-liquid suspension. Appl. Opt. (18):3600-3607.

Williams F.A. (1988) Combustion Theory. Combustion Science and Engineering Series. Addison & Wesley, Redwood City, 2nd edition.

Wilms J. (2005) Evaporation of multicomponent droplets. PhD-Thesis, Universität Stuttgart, Stuttgart, Germany.

Wuerker R.F., Shelton H., Langmuir R.V. (1959) Electrodynamic containment of charged particles. J. Appl. Phys. (30):342-349.

Xu F., Ren K., Gouesbet G., Gréhan G., Cai X. (2007) Generalized Lorenz-Mie theory for arbitrarily oriented, located and shaped beam scattering by a homogeneous spheroid. J. Opt. Soc. Am. A (24):119-131.

Xu F. (2007) Diffusion d´un Faisceau Quelconque par un Spheroide et Mesure en Ligne de la Vapeur Humide par l´Extinction Spectrale de la Lumiere. PhD Thesis, Universite de Rouen, Rouen, France.

Xu F., Lock J.A., Gouesbet G., Tropea C. (2008) Radiation torque exerted on a spheroid: analytical solution. Phys. Rev. A (78):013843.

Yariv A. (1975) Quantum Electronics, 2nd ed. Wiley, New York. Chap. 11.

Ye J., Cundiff S.T. (2005) Femtosecond Optical Frequency Comb Technology, Springer-Verlag, New York.

Yeh C.-N., Kosaka H., Kamimoto T. (1993) A fluorescence/scattering imaging technique for instantaneous 2-D measurement of particle size distribution in a transient spray. Proceedings 3rd Congress on Optical Particle Sizing, Yokohama, Japan.

Zhang J., Alexander D.R. (1992) Hybrid inelastic-scattering models for particle thermometry: unpolarized emissions. Appl. Opt. (31):7132-7139.

Zoubir A., Shah L., Richardson K., Richardson M. (2003) Practical uses of femtosecond laser micro-materials processing. Appl. Phys. A (77):311-315.

List of Figures

.

List of Symbols

Abbrevations:

AC	Alternating Current
BB	Broad Band
CCD	Charge Coupled Device
CPM	Colliding Pulse Mode-Locked Laser
CW	Continuous Wave
DBR	Distributed Bragg Reflector
DC	Direct Current
DFDL	Distributed Feedback Dye Laser
FLMT	Fourier-Lorenz-Mie Theory
GLMT	General-Lorenz-Mie Theory
GRT	Global Rainbow Thermometry
ICCD	Intensified Charge Coupled Device
IPI	Interferometric Particle Imaging
LED	Light Emitting Diode
LIDAR	Light Detection And Ranging
LIF	Laser Induced Fluorescence
LMT	Lorenz-Mie Theory
LSD	Laser Sheet Drop Sizing
MDR	Morphology Dependent Resonances
PDS	Planar Droplet Sizing
PIV	Particle Image Velocimetry
SL	Semiconductor Laser
SMD	Sauter Mean Diameter
SNR	Signal to Noise Ratio
VCSEL	Vertical Cavity Surface Emitting Laser

Greek symbols:

α	Angle	rad
Γ	Shape Factor of the Gaussian Envelope	s^2
δ, $\Delta\Phi$	Phase Difference	1
δ_d	Density of Levitated Object	$\frac{kg}{m^2}$
δ_{gas}	Density of Surrounding Atmosphere	$\frac{kg}{m^2}$
δ_{ik}	Kronecker Symbol	1
$\Delta\omega_0$	Pulse Width at Half Maximum	$\frac{1}{s}$
ϵ	Electric Permittivity	$\frac{A*s}{V*m}$
$\Delta\nu$	Spectral Width	$\frac{1}{s}$
$\Delta\Phi$	Feedback Phase in Cavity	rad
$\Delta\Phi_{BB}$	Feedback Phase in Cavity for Broadband Emission	rad
$\Delta\Phi_{stab}$	Feedback Phase in Cavity for Stable Emission	rad
Θ_i, $\tau_{i,t}$	Angle of Ray Incidence	rad
Θ_{rb}	Rainbow Angle	rad
Θ_{r1}	Scattering Angle in Region of First-Ord. Refr.	rad
Θ_{r2}	Scattering Angle in Region of Second-Ord. Refr.	rad
Θ_{r1c}	Highest Possible Angle in Region of First-Ord. Refr.	rad
Θ_{r2c}	Highest Possible Angle in Rainbow Region	rad
Θ_{r2rb}	Lowest Possible Angle in Rainbow Region	rad
Θ_s	Scattering Angle	rad
Θ_{SW}	Surface Wave Scattering Angle	rad
λ	Wavelength	m
λ_{dis}	Wavelength of Periodic Disturbances	m
ν	Phase	1
ν_{center}	Central Pulse Frequency	$\frac{1}{s}$
ν_g	Group Velocity	$\frac{nm}{s}$
ν_i	Frequency	$\frac{1}{s}$
ν_Φ	Phase Velocity	$\frac{nm}{s}$
ξ	Angle Associated with Circular Arc s	rad
τ_c	Critical Angle for Tangential Incidence	rad
τ_i	Angle of Incidence	rad
τ_{iRB}	Angle of Incidence for Lowest Rainbow Angle	rad
Φ	Electric Potential	V
Φ_0	Cylindrical Coordinate	rad
Φ_f	Flow Rate	$\frac{kg}{s}$
Φ_i	Phase Factor	$\frac{1}{s}$

Φ_{qe}	Quantum Efficiency	1
χ	Electric Susceptibility	1
ω	Angular Frequency	$\frac{1}{s}$
Ω_{rb}^2	Intensity Distribution of the Airy-Function	1

Latin symbols:

a	Longer Half Axis of Spheroid	m
b	Shorter Half Axis of Spheroid	m
A	Electric Field Strength Amplitude	$\frac{kg*m}{s^4*A}$
c	Velocity of Light	$\frac{m}{s}$
c_{dye}	Dye Concentration	$\frac{mol}{l}$
c_s	Sound Velocity	$\frac{m}{s}$
C	Function of Contrast	1
C_{cir}	Circumference	m
d_p	Particle Diameter	m
d_{ph}	Pinhole Diameter	m
D	Droplet Diameter	m
D_{beam}	Beam Diameter	m
d_{ori}	Diameter of Orifice	m
E	Electric Field	$\frac{kg*m}{s^3*A}$
F	Hydrodynamic Force	N
f	Focal Length	m
f_{dis}	Frequency of Liquid Jet Perturbance	$\frac{1}{s}$
g	Shape Parameter	$\frac{1}{s^2}$
I	Intensity	$\frac{W}{m^2}$
I_{dc}	Pump Current	A
I_{fl}	Intensity of Fluorescence	$\frac{W}{m^2}$
k	Wavenumber	$\frac{1}{m}$
l	Optical Path Difference in Surface Wave Model	m
l_p	Spatial Length of Pulse	m
L	Laser Cavity Length	m
L_{coh}	Coherence Length	m
n	Refractive Index	1
P	Polarization of Light	$\frac{C}{m^2}$
P_{out}	Output Power	W

P_p	Pulse Energy	W
p	Static Pressure	$\frac{N}{m^2}$
r	Position	m
r_{jet}	Radius of Liquid Jet	m
s_0	Ray Path in Surface Wave Model	m
s_1	Ray Path in Surface Wave Model	m
s_2	Arc Path in Surface Wave Model	rad
S	Scattering Function	$\frac{W}{m^2}$
t	Time	s
t_c	Coherence Time	s
t_p	Pulse Duration at Half Maximum	s
t_s	Shutter Time	s
Δt_{R-RB}	Time Difference between Refl. and Second-Order Refr.	s
t_r	Response Time	s
T	Cycle Period	s
T_{trans}	Transmission	1
U	Electric Potential	V
v_{jet}	Velocity of Liquid Jet	$\frac{m}{s}$
x	Distance	m
x_s	Size Parameter	1
y	Position along z-Axis	m
z	Position along z-Axis	m

Curriculum Vitae

Personal Information

Name: Saša Bakić

Date of Birth: June 19th, 1976

Place of Birth: Darmstadt, Germany

Nationality: German

Education

2005-2009: Doctoral research at the Chair of Fluid Mechanics and Aerodynamics, Technischen Universität Darmstadt, Darmstadt, Germany.

1998-2005: Academic Studies in Physics at Technischen Universität Darmstadt, Darmstadt, Germany. Final degree: Diplom-Physiker, Univ.